

5121

UNIVERSITY OF HAWAI'I LIBRARY

LONG-RANGE DETECTION OF SFERICS OVER THE PACIFIC OCEAN:  
THUNDERSTORM CHARACTERISTICS AND DATA ASSIMILATION  
INTO NWP MODELS

A DISSERTATION SUBMITTED TO THE GRADUATE DIVISION OF THE  
UNIVERSITY OF HAWAI'I IN PARTIAL FULFILLMENT OF THE  
REQUIREMENTS FOR THE DEGREE OF

DOCTOR OF PHILOSOPHY

IN

METEOROLOGY

AUGUST 2008

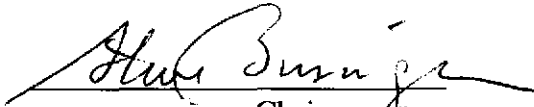
By  
Antti Pessi

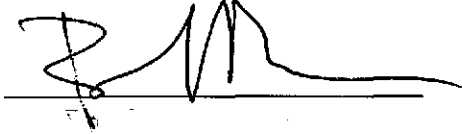
Dissertation Committee:

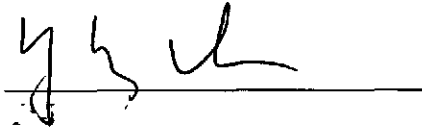
Steven Businger, Chairperson  
Yi-Leng Chen  
John Porter  
Yuqing Wang  
Ben Brooks

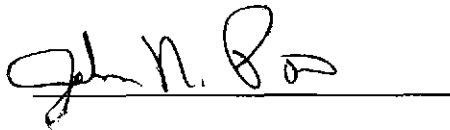
We certify that we have read this dissertation and that, in our opinion, it is satisfactory in scope and quality as a dissertation for the degree of Doctor of Philosophy in Meteorology.

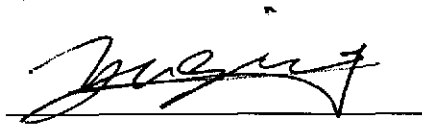
Dissertation committee:

  
Chairperson









## **ACKNOWLEDGEMENTS**

I would like to express my sincerest gratitude to my academic advisor, Professor Steven Businger, who has given me the opportunity to work with this interesting project and for his constant support throughout the program. I also thank my committee members for their guidance.

I would also like to thank my parents and family who have given their full support for me from the other side of the world, Finland. Thanks to all my friends and colleagues at the department. Finally, I would like to thank my wife Daša for her great support throughout this process.

## **ABSTRACT**

The waveguide between the earth's surface and the ionosphere allows very low frequency emissions generated by lightning, called sferics, to propagate over long distances. The new Pacific Lightning Detection Network (PacNet) utilizes this attribute to monitor lightning activity over the North Pacific Ocean with a network of ground-based lightning detectors.

The performance of the PacNet was assessed. Lightning detection efficiency (DE) and location accuracy (LA) model calibration procedures are detailed, and comparisons of model results with lightning observations from the PacNet in correlation with Tropical Rainfall Measuring Mission (TRMM) satellite's Lightning Imaging Sensor (LIS) are presented.

The implications of this work are that the DE and LA model output can be used in quantitative applications of the PacNet over the Pacific Ocean. For example, storms over the North Pacific Ocean are often poorly forecast due to the lack of observations over the ocean and insufficient initial conditions in numerical weather prediction (NWP) models. By virtue of the relationship between lightning and convective rainfall rates, PacNet data hold promise as input for NWP models as a proxy for latent heat release in convection.

To investigate the relationships between lightning and other storm properties, lightning data from PacNet and LIS were compared to data from TRMM's precipitation radar and microwave imager. Three years of data over the North Pacific Ocean were analyzed.

The results of the data analysis show a consistent logarithmic increase in convective rainfall rate with increasing lightning rates. Moreover, other storm characteristics, such as radar reflectivity and ice water path, show a similar logarithmic increase.

These results were utilized to assimilate lightning data from PacNet into a NWP model. A lightning data assimilation (LDA) system was programmed, which nudged the model's latent heating rates according to rainfall derived from lightning observations.

Two cases were analyzed. A rapidly deepening extratropical cyclone approaching the west coast of the U.S. was poorly forecast initially. The use of LDA improved the storm central-pressure forecast significantly. In the second case, a squall line associated with a Kona low moved over Hawaii. The location and timing of the squall line was improved using LDA.

## Table of Contents

<b>Acknowledgements</b> .....	iii
<b>Abstract</b> .....	iv
<b>List of Tables</b> .....	viii
<b>List of Figures</b> .....	viii
<b>Chapter 1. Introduction and Motivation</b> .....	<b>1</b>
1.1 Microscale studies on thunderstorms: Charge separation theories.....	4
1.1.1 Inductive charge (IC) separation.....	5
1.1.2 Non-inductive charge (NIC) separation .....	6
1.2 Mesoscale studies on thunderstorms: Major field campaigns.....	8
1.2.1 Continental field campaigns .....	9
1.2.2 Maritime field campaigns.....	10
<b>Chapter 2. Development of a Long-Range Lightning Detection Network for the Pacific: Construction, Calibration, and Performance</b> .....	<b>14</b>
2.1. Introduction .....	14
2.1.1. Very low frequency signal propagation .....	14
2.1.2. Long-range lightning location systems .....	18
2.2. Description of Pacific Lightning Detection Network.....	19
2.3. Assessment of PacNet sensor performance.....	20
2.3.1. Signal attenuation.....	23
2.3.2. Timing and angle errors .....	25
2.3.3. Diurnal variation .....	26
2.4. Modeling detection efficiency and location accuracy .....	28
2.4.1. Estimation of DE model parameters for salt-water path.....	32
2.4.2. Refinement of DE model using Puerto Rico observations.....	34
2.4.3. Modeling location accuracy.....	35
2.5. Observed performance of PacNet/LLDN.....	35
2.5.1. Observed detection efficiency .....	37
2.5.2. Observed location accuracy.....	39
2.6. Summary and conclusions.....	41
<b>Chapter 3. Relationships Between Lightning, Precipitation, and Hydrometeor Characteristics over the North Pacific Ocean</b> .....	<b>59</b>
3.1. Introduction .....	59
3.1.1 Maritime vs. continental storms.....	59
3.1.2 Lightning vs. rainfall.....	63
3.2. Data and methods .....	64
3.2.1. PacNet/LLDN data.....	64
3.2.2. TRMM data .....	66

3.2.3. Methods .....	68
3.3. Results .....	69
3.3.1. Vertical profiles of radar reflectivity and rainfall .....	70
3.3.2. Maximum radar reflectivity and altitude of the echo top .....	72
3.3.3. Lightning vs. rainfall .....	74
3.3.4. Latent heating .....	74
3.3.5. Vertical profiles of precipitable ice .....	76
3.3.6. Precipitation water path and ice water path .....	77
3.4. Summary, conclusions, and discussion .....	77
3.4.1 Conclusions .....	78
3.4.2. Discussion .....	79
<b>Chapter 4. The Impact of Lightning Data Assimilation on two Winter Storm Simulations over the North Pacific Ocean .....</b>	<b>94</b>
4.1 Introduction .....	94
4.2 Data and assimilation method .....	98
4.2.1 Lightning data .....	98
4.2.2 Model setup and assimilation method .....	99
4.3. Results .....	102
4.3.1. Extratropical storm on the northeast Pacific .....	102
4.3.2. Tropical squall line over Hawaii .....	111
4.4. Another approach – Four Dimensional Data Assimilation .....	113
4.5. Summary and discussion .....	115
<b>Chapter 5. Summary .....</b>	<b>146</b>
5.1 Focus of this research .....	146
5.2 Research conducted and main results .....	147
5.3 Future studies .....	150
<b>Appendix. Estimation of IC:CG correction for observational Detection Efficiency analysis .....</b>	<b>152</b>
<b>References .....</b>	<b>154</b>

## LIST OF TABLES

Table 3.1 Summary of heights and reflectivities at various dBZ and altitude thresholds. .....	82
--	----

## LIST OF FIGURES

Figure 1.1 Schematic diagram of the earth-ionosphere wave guide, which allows VLF (3-30 kHz) emissions from thunderstorms (sferics) to propagate thousands of kilometers through reflection. The best propagation is observed over the ocean at night. ....	12
Figure 1.2 Locations of four PacNet sensors installed at Unalaska, Lihue, Kona, and Kwajalein. The long-range lightning detection network (LLDN) sensors installed in the North America contribute specifically over the eastern Pacific. Dotted rectangle shows the area of analysis in discussed in Chapter 3. ....	12
Figure 1.3 Reversal temperature is a function of air temperature and liquid water content in the cloud. On the upper part of the figure (+) graupel is charged positively and on the lower part (-) negatively. Below the lowest horizontal line, where both liquid water content and temperature are very low, charge transfer is also positive (Saunders et al. 1991). ....	13
Figure 2.1 (a) Ground installation at Lihue airport, Kauai, (b) roof installation in Unalaska. ....	43
Figure 2.2 IMPACT-ESP sensor schematic diagram showing the relationship between the remote communications module (RCM), the remote power module (RPM), the primary line replaceable unit (PLRU) and the sensor power/communication module (SPCM). ....	44
Figure 2.3 Installation stage at Lihue airport. The magnetic direction finding loops are exposed at the top of the mast together with electric field and GPS antennas. Below them in the box is the main electronics module (PLRU). A laptop computer is connected to the sensor power/communication module to test the sensor. The power and communication cables are buried 90 cm below the surface. ....	44
Figure 2.4 Vertical electric field waveforms for a cloud-to-ground return stroke detected by sensors located at 264, 860, and 3400 km from the lightning stroke. The amplitude scale is uncalibrated. Black arrows in a) and b) indicate initial appearance of the ground wave, and the gray arrow in b) indicates the single-hop reflected wave. ....	45
Figure 2.5 Relative signal strength as a function of stroke distance as detected by a PacNet test sensor located in Tucson, Arizona for (a) day and (b) night. The error	

bars are $\pm 1$ standard deviation. The fitted curve shows the attenuation rate predicted by Eq. 2.....	46
Figure 2.6 Percentage of different propagation types as a function of distance for (a) day and (b) night. Thick solid line is for ground wave, dashed for first-hop sky-wave, and thin solid for second-hop sky-wave. The bars indicate the total number of strikes detected in each 200 km distance bin (right ordinate).....	47
Figure 2.7 (a) Daytime ground wave signal delay distribution for is centered at 20.0 $\mu$ s and has a standard deviation of 5.0 $\mu$ s. Second-hop sky wave distribution is centered at 90.0 $\mu$ s ( $\sigma=5.1 \mu$ s). (b) First-hop (inverted) sky-wave distribution is centered at 52.9 $\mu$ s and has a standard deviation of 4.7 $\mu$ s (graph inverted in reference to reversed polarity of first hop).....	48
Figure 2.8 Angle error without site-error correction has a mean value of -4.0 degrees and a standard deviation of 4.5 degrees (for both day and night). .....	50
Figure 2.9 Time-series plots of (a) the variation of arrival-time delay of VLF signals observed by the PacNet test sensor in Tucson, AZ relative to time-of-occurrence of the CG stroke determined by the NLDN. Each symbol represents the median value of nine time-ordered events. (b) Peak current estimated using the PacNet sensor magnetic field peak, relative to NLDN estimated peak current. Diamonds in the lower part of each figure show the distance of the events from the sensor (right ordinate). .....	51
Figure 2.10 Empirically derived diurnal DE variation over the North Pacific (solid line) and fitted curve used for diurnal DE correction (dashed line). Since the actual DE of ground-wave events is not exactly known, the DE-scale (y-axis) is relative. ....	52
Figure 2.11 Simplified schematic for LLS network detection efficiency. $I_0$ is the strike peak current, $P_i$ is the peak-current probability distribution, $r_1 \dots r_n$ are the distances between the strike and the sensors $S_1 \dots S_n$ . $SS_1 \dots SS_n$ are the incident signals at the sensors $S_1 \dots S_n$ . If the DE threshold is met then the signal is passed on to a central location algorithm.....	53
Figure 2.12 Cumulative peak current distribution derived from CG first strokes striking salt water near Puerto Rico. ....	54
Figure 2.13 Results from the detection efficiency model show (a) 5% day and (b) 20% night DE over Puerto Rico when using the reference peak-current distribution and space constants of 2000 and 6000 km for day and night, respectively. (c) Insert: Lightning data analysis region for Puerto Rico. The salt-water region is the "Sea" region, with the exclusion of the "Land" region. ....	55
Figure 2.14 Modeled DE (%) over the Pacific during (a) day, and (b) night. The boxes show the areas where the observed DE was assessed. The observed values for the Hawaii region were 22% and 61% during the day and night, respectively (lower box). DE values for the central-north region were 19% and 44% for day and night, respectively (upper box).....	56
Figure 2.15 Modeled LA (km) of PacNet/LLDN with four PacNet sensors located in Alaska, Kwajalein, Lihue, and Kona. The boxes show the areas where the observed LA was assessed. LA over the west, central, and east boxes was 40, 35, and 13 km, respectively.....	57

Figure 2.16 PacNet/LLDN lightning data (red dots) overlaid with GOES-10 infrared satellite image at 1000 UTC on 3 September 2004. Image processed by the author shows lightning active convective storms on the trans-Pacific air traffic routes between the U.S. west coast and Hawaii. Areas of intense lightning can be used to differentiate between cold cirrus and deep convection. Note that the impact of inferior network geometry on the location accuracy west of 160°W longitude is apparent in the image.....	58
Figure 3.1 Kohler curves for different size sulfates and sea salt. If a cloud condensation nuclei is small and supersaturation is low, particle does not reach the critical size and eventually evaporates. Larger CCN reach their critical size in lower supersaturation values and continue to grow. ....	82
Figure 3.2 Collision efficiencies vs ratio of colliding drop radii. Triangles (10 μm radius drop collector), squares (20 μm radius drop collector) and circles (30 μm radius drop collector) (Pinsky et al, 1999). The theoretical results obtained in different studies (Pruppacher and Klett 1978) are also presented; dotted lines, Jonas (1972); dashed lines, Klett and Davis (1973); dashed-dotted lines, Lin and Lee (1975); solid line, Schlamp et al. (1976).....	83
Figure 3.3 Cumulative probability distribution function for PacNet lightning rate [flashes × (10 <sup>4</sup> km <sup>2</sup> h <sup>-1</sup> ) <sup>-1</sup> ] and PR convective rainfall rate [mm h <sup>-1</sup> × 10]. The x-axis is suppressed with ~99% of the highest rates shown. ....	84
Figure 3.4 (a) GOES-10 infrared image at 1130 UTC on 30 August 2005 overlaid with one-hour of PacNet lightning observations. (b) NCEP Reanalysis at 1200 UTC on 30 August 2005 at 250 hPa shows a low northwest of Hawaii. (c) NWS subjective surface analysis of the central Pacific at 1200 UTC on 30 August 2005 shows a surface trough northwest of Hawaii. Streamlines are plotted in gray south of 30°N. ....	85
Figure 3.5 As in Figure 3.4 but for 0600 UTC on 12 December 2005. Satellite image in (a) is valid at 0630 UTC.....	86
Figure 3.6 Vertical profiles of PR reflectivity in (a) winter and (b) summer for three different lightning rate categories (low, moderate, and high lightning rate). Low lightning rate category is the lowest bin from PacNet data, moderate category is the highest PacNet data bin, and high category the highest LIS bin, as described in Section 3.2.3. Lowest levels are not shown since the near-surface range bins were frequently filled with surface clutter, or missing data. Despite a sensitivity threshold for PR echos of ~17 dBZ, values start from zero because of the compositing method. ....	87
Figure 3.7 (a) Maximum PR reflectivity and (b) maximum height of radar echo. Squares and solid lines are for winter data and diamonds and dashed lines for summer data. Filled symbols are PacNet data, open symbols are LIS data, and grey symbols are combined PacNet and LIS data. Abscissa shows the number of lightning flashes per hour normalized over 10 <sup>4</sup> km <sup>2</sup> . The error bars are ± 1 σ.....	88
Figure 3.8 (a) Convective rainfall vs. lightning rate and (b) stratiform rainfall vs. lightning rate. Symbols and lines as in Figure 3.7. ....	89

Figure 3.9 As in Figure 3.6, but vertical profiles of latent heating in (a) winter and (b) summer for low, moderate and high lightning rates. Lines and symbols as in Figures 3.6 and 3.7. ....	90
Figure 3.10 As in Figure 3.6, but precipitable ice content, derived from TMI data, as a function of height and lightning rate. ....	92
Figure 3.11 (a) Precipitation water path derived from PR and (b) ice water path derived from TMI. Lines and symbols as in Figure 3.7. ....	93
Figure 4.1 Lightning – convective rainfall relationship using PacNet lightning data and TRMM’s PR rainfall data. The fitted curve in the middle (solid) is described by the equation $y=0.67*\ln(x)+9.2$ ( $R^2=0.89$ ). The $y$ -error bars represent $\pm 1\sigma$ in rainfall rates. The corresponding fitted curves are described by equations $y=0.68*\ln(x)+13.6$ ( $R^2=0.75$ ) and $y=0.66*\ln(x)+4.8$ ( $R^2=0.92$ ), respectively. The $x$ -error bars and corresponding curves illustrate a hypothetical $\pm 50\%$ error in lightning rates. The upper and lower curves are described by equations $y=0.67*\ln(x)+9.6$ and $y=0.67*\ln(x)+8.9$ , respectively. ....	118
Figure 4.2 (a) Surface analysis of the eastern North Pacific Ocean valid at 0000 UTC on 18 December 2002. (b) GOES-10 IR satellite image valid at 0030 UTC on 18 December 2002 overlaid with one hour of lightning observations. Each red dot indicates a lightning flash detected by LLDN $\pm 30$ minutes from the satellite image time. “L” marks the low center. (c) Surface analysis valid at 1200 UTC and (d) satellite image valid at 1230 UTC 18 December 2002. ....	119
Figure 4.3 Twelve-hour MM5 forecast of sea-level pressure (hPa) and 3-h accumulated rainfall (mm) valid at 1200 UTC on 19 December 2002. (a) Control run and (b) LDA run. ....	121
Figure 4.4 Difference in sea-level pressure (hPa) and rainfall (mm) between the LDA and control runs (as shown in Fig. 4.3). Valid at 1200 UTC on 19 December 2002. “LAT” in figure titles indicates latent heating LDA run and “CTRL” indicates control forecast. ....	122
Figure 4.5 As Figure 4.4, but valid at 0000 UTC on 20 December 2002. ....	123
Figure 4.6 Difference in 700 hPa $\theta_e$ between the control and LDA runs at (a) 0300 UTC, (b) 0600 UTC, (c) 0900 UTC, and (d) 1200 UTC on 19 December 2002 (shaded, [K]). Sea-level pressure is shown from the LDA run at given hour (contours, [hPa]). ....	124
Figure 4.7 Cross-section across the storm along 46°N (horizontal line in Fig. 4.6d) valid at 1200 UTC on 19 December 2002. (a) Difference in $\theta_e$ (K) and geopotential height (m) between the LDA and control runs. (b) Difference in $T_e$ (K) and geopotential height (m). The red “L” indicates the position of the surface low center. ....	125
Figure 4.8 Difference in 500 hPa wind speed ( $m s^{-1}$ ) between the LDA and control runs at 0600 UTC on 19 December 2002 (shaded). Sea-level pressure (hPa) is shown from the LDA run (contours). ....	126
Figure 4.9 Comparison of observed storm central pressure (solid) with that predicted by MM5 with (dotted) and without (dashed) lightning data. The model was initialized	

at 0000 UTC 19 December 2002 and ran for 24 hours. The observed values are from the NWS North Pacific surface analyses at 0000, 0600, 1200, and 1800 UTC, and the values between them are linearly interpolated. The arrow shows the LDA period. ....	127
Figure 4.10 24-hour forecast of sea-level pressure and 3-h accumulated rainfall. (a) Control run and (b) LDA run. Forecast valid at 0000 UTC 20 December 2002. The observed storm central pressure was 978 hPa (marked with "x").....	128
Figure 4.11 24-hour MM5 forecast of sea-level pressure (hPa) and 3-h accumulated rainfall (mm) valid at 1200 UTC on 19 December 2002. (a) Control and (b) LDA run. ....	129
Figure 4.12 As in Figure 4.9, but the model was initialized at 1200 UTC 18 December 2002 and ran for 36 hours. ....	130
Figure 4.13 As in Figure 4.9, but the model was initialized at 0000 UTC 18 December 2002 and ran for 48 hours. ....	130
Figure 4.14 Difference in sea-level pressure (hPa) and rainfall (mm) between the "standard" LDA run and LDA run using (a) $+1\sigma$ rainfall rates, and (b) $-1\sigma$ rainfall rates (see Fig. 4.1). 24-h forecast valid at 1200 UTC on 19 December 2002.....	131
Figure 4.15 Comparison of "standard" LDA run storm central pressure (solid) with pressure from LDA run using $+1\sigma$ rainfall rates (dashed) and $-1\sigma$ rainfall rates (dotted). The model was initialized at 1200 UTC 19 December 2002 and ran for 36 hours.....	132
Figure 4.16 (a) Surface analysis and (b) GOES-10 IR satellite image valid at 0600 UTC on 19 February 2004. Image is overlaid with $\pm$ one hour of lightning observations from the image time. ....	133
Figure 4.17 a) MM5 6-hr forecast without lightning data of precipitation (shading) and sea-level pressure (contours). b) MM5 6-hr forecast with lightning data. (c) Satellite IR image. All valid at 0600 UTC on 28 February 2004 .....	134
Figure 4.18 as in Figure 4.17, but valid at 1200 UTC on 28 February 2004.....	135
Figure 4.19 as in Figure 4.17, but valid at 1800 UTC on 28 February 2004.....	136
Figure 4.20 as in Figure 4.17, but valid at 0000 UTC on 29 February 2004.....	137
Figure 4.21 Wind speed (shaded [knots]) and sea-level pressure (contours [hPa]) valid at 1800 UTC 28 February 2004 for (a) control and (b) LDA run. White wind barbs are surface observations.....	138
Figure 4.22 Vertical cross section across the squall line (see Figs. 4.17-4.20 for location) for (a) control run and (b) LDA run. Shaded areas show $\theta_e$ (K) and contours show vertical velocity ( $m s^{-1}$ ). The forecast initialization time was 0000 UTC and the forecast is valid at 0600 UTC on 28 February 2004.....	139
Figure 4.23 As in Figure 4.22, but forecast is valid at 1200 UTC on 28 February 2004. ....	140
Figure 4.24 As in Figure 4.22, but forecast is valid at 1800 UTC on 28 February 2004. ....	141
Figure 4.25 As in Figure 4.22, but forecast is valid at 0000 UTC on 29 February 2004. ....	142

Figure 4.26 12-hour forecast of sea-level pressure and 3-h accumulated rainfall. Valid at 1200 UTC on 19 December 2002. Lightning data was assimilated using FDDA. 143

Figure 4.27 As Figure 4.10, but FDDA run added (dashed-dotted curve). ..... 144

Figure 4.28 MM5 6-hr forecast of precipitation (shading) and sea-level pressure (contours) valid at 0600 UTC on 28 February 2004. Lightning data was assimilated using FDDA. .... 145

## CHAPTER 1. INTRODUCTION AND MOTIVATION

The paucity of in situ observations over the North Pacific Ocean can lead to significant errors in the initial moisture fields input into operational numerical weather prediction (NWP) models and result in inadequate initial conditions of the models. These observational errors in turn often lead to large forecast errors in simulated storm geopotential height, wind, and rainfall (e.g., McMurdie and Mass 2004). Accurate knowledge of the distribution and evolution of moisture- and latent heating fields associated with deep convection is essential for accurate numerical forecasts of cyclogenesis (e.g., Anthes et al. 1983; Brennan and Lackmann 2005).

Radiosonde and weather radar sites are limited to a few Pacific islands that are generally located thousands of kilometers apart. Moreover, effective radar scans extend only ~200 km from the radar. Although geostationary satellites offer continuous monitoring of clouds and water vapor on visible and infrared channels, cirrus anvils often obscure convective activity. Some low orbiting satellites carry microwave radiometers and precipitation radars such as Tropical Rainfall Measuring Mission (TRMM) with its Microwave Imager (TMI) and Precipitation Radar (PR) (e.g. Kummerow et al. 1998). Unfortunately, they provide only intermittent glimpses of convective activity, typically having twice-per-day coverage. Therefore, they do not permit continuous monitoring of the evolution of convective weather systems.

TRMM satellite also carries a Lightning Imaging Sensor (LIS) (Christian et al. 1992). It detects lightning with good detection efficiency (73-93%), but provides only

~90 s view time per overpass (Boccippio et al. 2002). The next generation series of GOES-R (Geostationary Operational Environmental Satellite) are scheduled to be equipped with Geostationary Lightning Mappers (GLM) (Christian 2006) that will monitor lightning activity continuously over a wide field of view. Until these instruments are in orbit, tested and calibrated, ground-based lightning detection remains the only method to provide a continuous lightning data stream. The launch of the first GOES-R series satellite is scheduled for 2014.

Long-range lightning detection networks utilize the waveguide between the earth's surface and the ionosphere. The waveguide allows very low frequency (VLF) electromagnetic waves generated by lightning strike channels, called sferics, to travel thousands of kilometers (Fig. 1.1). The Pacific Lightning Detection Network (PacNet) is a network of widely spaced (400-3800 km) lightning detectors installed on the islands of the North Pacific (Fig. 1.2) to monitor thunderstorm activity over the central and eastern North Pacific Ocean. PacNet is one of the few observing systems, outside of geostationary satellites, that provide continuous real-time data throughout a synoptic-scale coverage area over the open ocean. In Hawaii and the surrounding Pacific region, PacNet helps to fulfill a requirement for long-distance, real-time storm tracking.

Several studies have shown the value of lightning detection for real-time storm tracking, warning, and nowcasting (e.g. Johnson et al. 1982; Demetriades and Holle 2005; Squires and Businger 2008). In remote regions where conventional data sources are not available, tracking of thunderstorms and assessing cyclone intensification are important challenges in weather prediction. Some of the cirrus-obscured clouds pose

little hazard to aircraft operations; however, convective clouds that produce lightning have significant updrafts, increasing the threat of turbulence and icing. A lack of real-time weather data from the areas surrounding civilian airports on islands presents an important opportunity for long-range lightning detection. In Hawaii and the surrounding Pacific region there has been an unmet requirement for long-distance, real-time storm tracking that can now be met using modern ground-based long-range Lightning Location Systems (LLSs). Because of the long-range propagation characteristics of lightning electromagnetic signals in the VLF range, long-range LLSs provide cost-effective, accurate monitoring of convective storms over a synoptic-scale region.

A promising application of PacNet is to derive estimates of the rainfall rate and hydrometeor characteristics from lightning data over the Pacific Ocean. The relationship between lightning and convective rainfall has been shown to vary, depending on air-mass characteristics and cloud microphysics (e.g. Petersen and Rutledge 1998). However, several studies have showed, that over a particular climatic regime and a limited geographic region, lightning is well correlated to convective rainfall (Cheze and Sauvageot 1997; Petersen and Rutledge 1998; Tapia et al. 1998; Soriano et al. 2001). One goal of this study is to investigate if these previous results can be confirmed over the North Pacific Ocean. In that case, lightning data could be used as a proxy for convective rainfall or latent heating rates in deep convective clouds and assimilated into numerical models.

This dissertation is organized as follows: Next, at the end of this chapter, the main cloud charging theories are reviewed and the major field campaigns on thunderstorms introduced. Recently installed Pacific Lightning Detection Network is documented in Chapter 2, including a detailed analysis of the network performance and detection efficiency and location accuracy models. Chapter 3 includes a comprehensive discussion of maritime and continental thunderstorm characteristics. Oceanic thunderstorms over the North Pacific Ocean are studied using data from PacNet. The observations from quantified PacNet data stream are compared with satellite-based rainfall and hydrometeor data, and used to investigate the relationships between lightning, rainfall, and hydrometeor characteristics over the North Pacific Ocean. In Chapter 4, these results are applied to assimilate lightning data from PacNet into a mesoscale NWP model over the North Pacific by specifying convective areas that were originally inadequately initialized in the model. Chapter 5 summarizes the work done in this dissertation.

### **1.1 Microscale studies on thunderstorms: Charge separation theories**

Lightning is a manifestation of a deep, convective cumulonimbus cloud, where the electrical potential difference has exceeded its breakdown value. There is no unique cloud electrification mechanism and the charge separation theories are still exploratory. Several mechanisms operate within different parts of a cloud and different mechanisms can operate within the same part of a cloud. However, numerous field- and laboratory experiments, and numerical modeling studies have been carried out, and a consensus regarding the basic mechanisms has emerged. Takahashi (1984) used a numerical model

to capture the major stages of cloud electrification. Recently, Advanced Cloud Resolving Models (CRM) and Explicit Microphysics Models (EMM) have become increasingly popular in cloud electrification studies (e.g. Phillips et al. 2001), where the varying cloud microphysical parameters, including aerosols, can be specified. Cloud electrification mechanisms have been tested in laboratories (e.g. Saunders 1994). In addition, aircraft and balloon measurements of the charges on precipitation particles in the thunderstorms have been made (e.g. Gaskell et al. 1978; Marshall and Winn 1982; Marshall and Rust 1991). Takahashi (1990) used a Precipitation Particle Image Sensor (PPIS) or videosonde, which made observations of hydrometeor particles in clouds.

Based on the knowledge gained from these experiments, among others, the charging theories are often divided into two categories. (i) A process where charge is transferred during particle collisions, and oppositely charged particles are carried to different levels within updrafts. This process is considered the dominant mechanism for charge separation. (ii) A process where particles are charged by ion capture and separated by convective motions, also known as convective charging. The first type of process is further divided into inductive (IC) and non-inductive (NIC) charge separation categories.

### *1.1.1 Inductive charge (IC) separation*

Inductive charging requires an existing vertical electric field, which polarizes the cloud particles. When particles with different vertical velocities collide, the oppositely charged particles are carried to different levels and the electric field is further

strengthened. The IC transfer methods are divided into two categories: drop breakup and particle rebound. Above the freezing level, the dominant electric field within the cloud is usually positive over negative. This electric field generally causes the bottom of a droplet to become positive and the top of the droplet to become negative.

Drop breakup IC occurs when the environmentally induced charge separation within a droplet is redistributed when the droplet breaks up. The breakup of the droplet is usually due to the collision and coalescence process occurring within clouds. Particle rebound occurs when a smaller particle asymmetrically collides with the bottom of a larger particle due to differential fall velocities. A portion of the positive charge of the bottom of the large droplet will be lost and transferred to the smaller droplet. For both drop breakup and particle rebound the charge separation within the cloud comes as a result of the redistribution of the differing charged particles via gravitational separation (Beard and Ochs 1986).

#### *1.1.2 Non-inductive charge (NIC) separation*

Non-inductive charging is independent of the local electric field and usually occurs during cloud particle collisions. Two main methods of NIC transfer operating during collisions are thermoelectric effect and contact potential effect (Caranti et al. 1985; Pruppacher 2000).

The thermoelectric effect states that a collision by two particles of different temperatures will cause a temperature gradient across the particles. This temperature gradient causes an ion gradient and a resultant electric field across the particles. Large

objects, such as hail, will tend to be frozen, whereas smaller particles may remain in liquid phase (i.e. supercooled water). A collision between the two would tend to cause the colder particle to acquire a negative charge, while the small particle would acquire a positive charge.

Contact potential effect requires the collision of two particles, which have differing electric surface potential. The difference in contact potential tends to equalize by transferring charges between particles. Contact potential varies with riming rate and temperature (Saunders 1995).

Extensive laboratory work, models, and aircraft data all suggest that the most efficient charge separation occurs during the interactions of vapor grown ice crystals with graupel, in the presence of supercooled water droplets (Saunders 1993; MacGorman and Rust 1998). Illingworth and Caranti (1985) found that in the absence of supercooled water, ice conductivity is too low to allow charge separation during the short contact time. Instead, as long as there is supercooled water among the ice particles and graupel is riming, conductivity of an ice sphere is sufficient for charge separation. The sign of the charge transfer to graupel particles is a function of temperature and effective liquid water content in cloud, so that at low temperatures ice crystals charge graupel negatively and at high temperatures positively (Reynolds et al. 1957; Church 1966). Gaskell and Illingworth's (1980) and Takahashi's (1978a) results also support the earlier experiments. In addition, Takahashi found that positive graupel charging also occurred at low temperatures if liquid water content was low. Saunders et al. (1991) carried out a number of cloud chamber experiments and formulated the dependence of the charge transfer on

temperature and liquid water content (Fig. 1.3). That said, charging between unriming ice crystals has been observed (Mason and Dash 2000; Dash and Wettlaufer 2003).

Freezing drop breakup mechanism is another NIC process. When a droplet begins to freeze, the outer ice shell of the droplet is positively charged, while the main inner core is negatively charged. If the droplet fractures during freezing, the main core of the particle will remain negatively charged, and the ice splinters associated with the outer shell will remain positively charged. Again, gravitational separation of the oppositely charged particles will cause the electric field within the cloud to strengthen.

## **1.2 Mesoscale studies on thunderstorms: Major field campaigns**

Due to the mesoscale nature of the thunderstorms, the fundamental knowledge of the structure and evolution of the thunderstorms has been achieved from field campaigns. During the field campaigns, the data were gathered utilizing observations from ground based observational networks (sensors located either on the ground, buoy, or ship), aircraft measurements, which often included Lightning Instrumentation Package, weather balloons, and ground based lightning detection networks.

Majority of the severe storm field campaigns have concentrated on the continental storms. Most of them were conducted in the central United States or Florida. In addition, several field campaigns have been conducted over the oceans, but only a few of them included lightning studies. These campaigns have yielded hundreds of publications, whose results are too numerous to summarize here.

### *1.2.1 Continental field campaigns*

The pioneering severe storm field campaign was The Thunderstorm Project (Byers and Braham 1949). It was carried out during the summers of 1946 and 1947 in Florida and Ohio, respectively. The Thunderstorm Project was a result of cooperation of four U.S. government agencies: the U.S. Weather Bureau, the U.S. Army Air Force, Navy, and National Advisory Committee for Aeronautics (predecessor of NASA). The project used a high-resolution (1-2 km) network of automatic recording surface stations, weather balloons, and aircraft observations. Some of the fundamental findings from this campaign are still used today to describe the structure and evolution of the thunderstorms. The thunderstorms were divided roughly into two categories: airmass and severe. Airmass or single-cell storms are disorganized and short-lived. A convective cell goes typically through three stages during an approximate 45-min lifetime: (1) the cumulus stage, (2) the mature stage, and (3) the dissipating stage. In severe thunderstorms, the updrafts and downdrafts are typically separate from one another due to the wind shear. This allows the storm to last longer and to develop severe weather.

The COoperative Huntsville Meteorological EXperiment (COHMEX) was conducted in the vicinity of Huntsville, Alabama during June-July 1986 (Fulton and Heymsfield 1991). The North Dakota Thunderstorm Project (NDTP) was held in the vicinity of Bismarck during June - July 1989 (Boe et al. 1992). The Airborne Field Mill (ABFM) Project was conducted during the summers of 1990 and 1991 and during winter 1992 in the vicinity of Kennedy Space Center, Florida (Harris-Hobbs et al. 1994). The Convection and Precipitation/Electrification (CaPE) field experiment was carried out in

the vicinity of Cape Canaveral, Florida during July and August 1991 (e.g. Wilson and Megenhardt 1997). The U. S. Weather Research Program, formerly the STormscale Operational and Research Meteorology (STORM) program, conducted an experiment called the STORM-FEST (Fronts Experiment Systems Test) during February-March 1992 (Szoke et al. 1994). The Severe Thunderstorm and Precipitation Study (STEPS-2000) field campaign was conducted during May-July 2000 in eastern Colorado and western Kansas along the climatological position of the dry line (Lang et al. 2004). Thunderstorm Electrification and Lightning Experiment (TELEX) was held in central Oklahoma, during May-June in 2003 and 2004 (Rust et al. 2004).

### *1.2.2 Maritime field campaigns*

In addition to continental experiments, some campaigns have been conducted over maritime regions – either over the open ocean or in the vicinity of islands. The Island Thunderstorm Experiment (ITEX) was a field campaign and modeling study of the thunderstorms forming regularly over Bathurst and Melville Islands north of Darwin, Australia, during the breaks in the summer monsoon and during the transition season. The experiment was carried out in November-December 1988 (Keenan et al. 1989). The Tropical Ocean Global Atmosphere Coupled Ocean-Atmosphere Response Experiment (TOGA COARE) was conducted during the 4-month period between November 1992 and February 1993 (Webster and Lucas 1992). The experiment was conducted over the western Pacific equatorial zone (10°N-10°S; 140-180°E). It included a study of thunderstorms and lightning using a network of three cloud-to-ground lightning sensors.

Measurements of cloud electrification were also made from the NASA's ER-2 and DC-8 airplanes (Lucas and Orville 1996; Petersen et al. 1996; Orville et al. 1997). The Maritime Continent Thunderstorm Experiment (MCTEX) was conducted during November-December 1995 over the same region as ITEX - Bathurst and Melville Islands (Tiwi Islands) in Australia, 50 km off the coast of Northern Territory (Keenan et al. 2000). A network of Advanced Lightning Direction Finders (ALDF) was deployed to monitor electrical activity over the islands.

In the next Chapter, the Pacific Lightning Detection Network is introduced, followed by the results from new studies of the Pacific thunderstorms conducted for this dissertation.

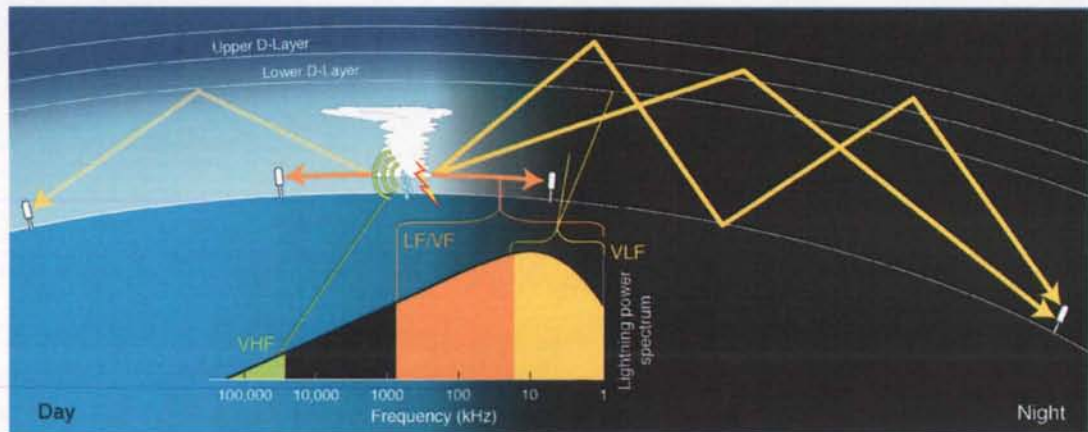


Figure 1.1 Schematic diagram of the earth-ionosphere wave guide, which allows VLF (3-30 kHz) emissions from thunderstorms (sferics) to propagate thousands of kilometers through reflection. The best propagation is observed over the ocean at night.

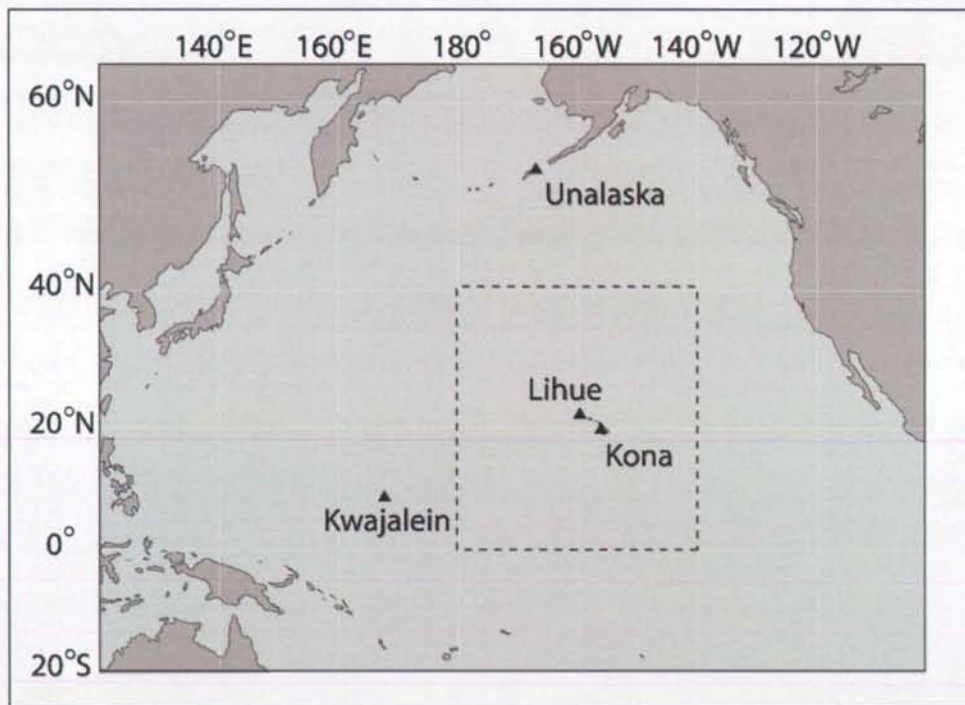


Figure 1.2 Locations of four PacNet sensors installed at Unalaska, Lihue, Kona, and Kwajalein. The long-range lightning detection network (LLDN) sensors installed in the North America contribute specifically over the eastern Pacific. Dotted rectangle shows the area of analysis in discussed in Chapter 3.

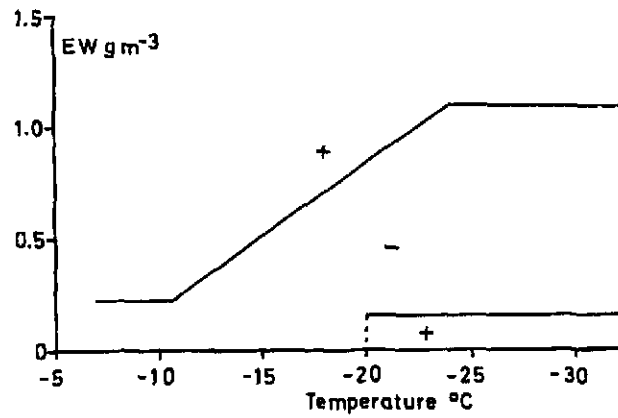


Figure 1.3 Reversal temperature is a function of air temperature and liquid water content in the cloud. On the upper part of the figure (+) graupel is charged positively and on the lower part (-) negatively. Below the lowest horizontal line, where both liquid water content and temperature are very low, charge transfer is also positive (Saunders et al. 1991).

# CHAPTER 2. DEVELOPMENT OF A LONG-RANGE LIGHTNING DETECTION NETWORK FOR THE PACIFIC: CONSTRUCTION, CALIBRATION, AND PERFORMANCE<sup>1</sup>

## 2.1. Introduction

### 2.1.1. Very low frequency signal propagation

Electromagnetic waves created by a lightning discharge radiate over a broad frequency range and propagate in all directions. Very high frequency (VHF) emissions occur during virgin electrical breakdown as well as during leader and streamer processes (Mazur et al. 1995; Shao and Krehbiel 1996). These signals can only be detected at ranges up to a few hundred kilometers since they rely on line-of-sight propagation and are not reflected by the ionosphere. The large current variations associated with return strokes in cloud-to-ground (CG) and very large pulses in cloud discharges are mainly observable in the low frequency (LF) and very low frequency (VLF) regions of the spectrum (Cummins et al. 1998a). When propagation distances are less than about one thousand km, significant energy in both the VLF and LF band can propagate as a ground

---

<sup>1</sup> Pessi et al. 2008: Development of a Long-Range Lightning Detection Network for the Pacific: Construction, Calibration, and Performance. *J. Atmos. Oceanic Technol.* In review.

wave, as shown in Figure 1.1. At greater distances, energy in the VLF portion of the spectrum between 3 and 30 kHz (sferics) can propagate effectively in the waveguide defined by the earth's surface below and by the ionosphere above, specifically its lowest layer, the D region. Out to roughly 4000 km, most of the energy is carried in signals that can be accounted for using the first two "ionospheric hops" shown in Figure 1.1. At even greater distances, propagation is more efficiently characterized using modal analysis (Wait 1968). Electron densities increase rapidly with height in the D region, typically from a few per  $\text{cm}^3$  to a few hundred per  $\text{cm}^3$ . VLF waves typically reflect from the heights 60-75 km during the daytime when high electron densities extend into the lower ionosphere. During the night the high electron density retreats to higher altitudes, with the reflections occurring in the range 75-90 km.

Ionospheric D region characteristics are often defined by two parameters, the reflection height  $h'$  and the exponential sharpness factor  $\beta$  (rate of increase of electron density with height) (Wait and Spies 1964). The parameter values are particularly stable during the day, resulting in predictable daytime wave propagation (Thomson 1993; McRae and Thomson 2000). The characteristics of the nighttime ionosphere are more variable and the signal propagation is less predictable than by day. Thomson et al. (2007) measured the nighttime D region parameters from VLF phase and amplitude observations and found average midlatitude values of  $h'=85.1\pm 0.4$  km and  $\beta=0.63\pm 0.04$   $\text{km}^{-1}$ . For daytime, McRae and Thomson (2004) found the value of  $h'$  varying between 58-71 km and Thomson (1993) found an average value of  $\beta=0.45$   $\text{km}^{-1}$ . Other factors, such as ground conductivity  $\sigma_g$ , ground permittivity and ambient magnetic field affect the VLF

propagation. Attenuation rate is the smallest for  $\alpha_g = \infty$ , which is a good approximation for sea water (Wait 1968).

Clilverd et al. (1999a) investigated lightning activity in Africa and South-America from 10 kHz spectral power measurements using a VLF receiver in Halley, Antarctica. To investigate the significant diurnal and annual variations in the VLF propagation, they used signals from 10 kHz Omega transmitters in Liberia and Argentina. They found that during the Austral winter, the relative signal strength in the Argentina-Halley path dropped quickly (in two hours) at 1100 UTC from its nighttime value of 1.0 to 0.6. The propagation factor in the Liberia-Halley path dropped quickly at 0600 UTC from 1.0 to 0.45, but required six hours to reach its minimum value of 0.2. The annual variation in propagation factor varied between 1.0 in July and  $\sim 0.7$  in January in both paths.

It is commonly known that eastward and westward propagating VLF waves have different propagation characteristics (e.g. Taylor 1960). The mean attenuation rate for subionospheric, westward propagating waves have been observed to be somewhat greater than for eastward propagation. Nickolaenko (1995) used VLF navigation system Omega at 10.2 kHz in the Atlantic and found attenuation rates of  $2.1 \text{ dB Mm}^{-1}$  for eastward propagation and  $2.6 \text{ dB Mm}^{-1}$  for westward propagation. Pappert and Hitney (1988) modeled nocturnal VLF signal propagation between Hawaii-San Diego and Hawaii-Wake Island using empirical electron density profiles with ionospheric parameters of  $\beta = 0.5 \text{ km}^{-1}$  and  $h' = 87 \text{ km}$ . They compared the predictions to in-flight measurements and found that the predictability was much better for eastward- than for westward propagation. They argued that the propagation to the west is less stable and more

sensitive to the variations in the ionosphere than propagation to the east. This is a second order effect, which is not incorporated in the simple propagation models employed in this study.

When the sunrise or sunset terminator crosses the propagation path, the situation becomes more complicated. A simple single-mode propagation theory is not sufficient, but multiple modes are required to explain the VLF propagation, as was noted by Budden (1961) and Wait (1962). Crombie (1964) modeled the effect of the sunrise terminator crossing over long VLF signal paths. He used a model with two waveguide modes and assumed a *second mode* in the nocturnal part of the path with significant mode conversion at the terminator. The terminator effect has been later discussed in many papers including Walker (1965), Ries (1967), Lynn (1967), and Pappert and Snyder (1972). Clilverd et al. (1999b) investigated 24-kHz signal propagation along a 12,000 km path from Cutler, Maine to Faraday, Antarctica. The path was nearly parallel with north-south meridian with only 3° deviation from the meridian. They used five years of observations and the Naval Ocean Systems Center (NOSC) Long Wave Propagation Capability code (LWPC) (Ferguson and Snyder 1990). The gross features of propagation were relatively well modeled. Particularly the timing of the amplitude minimum during the Austral summer was very well predicted, whereas the amplitude prediction was poorer.

Based on the above body of knowledge, the approach taken in this study will be to employ different model parameters for daytime and nighttime propagation that take into account diurnal changes in ionospheric electron density and ground conductivity, but that

ignore the directional, second-order, propagation effects. Since the propagation distances of interest are at or below 4000 km, analysis and results will be presented in terms of ground-wave and sky-hop propagation.

### *2.1.2. Long-range lightning location systems*

Research systems exist that employ long-range lightning location methods, with varying levels of performance and areas of coverage. The World Wide Lightning Location Network (WWLLN) (Rodger et al. 2006) utilizes a time-of-group-arrival (TOGA) method to locate lightning strikes. The Zeus long-range network (Chronis and Anagnostou 2003) uses an arrival-time-difference method. The U.K. Met Office employs the Arrival Time Difference Network (ATDNET) (Nash et al. 2005; Keogh et al. 2006). Time-of-arrival methods typically need detection from 3 or 4 sensors to compute a strike location. PacNet sensors combine both magnetic direction finding (MDF) and time-of-arrival (TOA) based methods and can locate a strike with as few as two sensors. We note that determining a location using *ionospherically-propagated signals seen by only two sensors* will have somewhat larger location errors, when compared to locations produced by three or more sensors. This is because polarization errors (due to non-horizontal components of ionospherically-propagated magnetic fields) can result in azimuth errors of several degrees.

In this chapter, the construction and instrumentation of the Pacific Lightning Detection Network (PacNet) is described and its observed performance and limitations are assessed. Furthermore, we describe the development of detection efficiency (DE) and

location accuracy (LA) models and outline the derivation of the model parameters.

Together these are necessary initial steps toward the goal of quantitative applications of the lightning data stream, such as assimilation into NWP models.

## **2.2. Description of Pacific Lightning Detection Network**

VLF sensors have been installed on four islands in the North-Pacific Ocean:

(i) Unalaska in the Aleutian Islands, Alaska, the Hawaiian Islands of (ii) Hawaii and (iii) Kauai, and (iv) Kwajalein in Marshall Islands (Figs. 1.2 and 2.1). PacNet sensors<sup>2</sup> are modified IMPACT ESP (Improved Accuracy from Combined Technology, Enhanced Sensitivity and Performance) sensors designed for long-range detection (Figs. 2.2 and 2.3). The gain has been set to a high level in order to receive weak, ionospherically reflected sferics, and the bandwidth has been adjusted to have greatest sensitivity in the VLF band. The sensors use combined technology that employs both time-of-arrival and magnetic direction finding methods in the data processing (Cummins et al. 1998b). These sensors work in combination with Vaisala's Long Range Lightning Detection Network (LLDN), which consists of National Lightning Detection Network (NLDN) and Canadian Lightning Detection Network (CLDN) sensors located throughout the U.S. and Canada. The ~200 broadband LF/VLF sensors in these networks are not optimized for long-range detection, but still provide important contributions to the overall network performance. The resulting long-range research network, hereafter called *PacNet/LLDN*,

---

<sup>2</sup> We hereafter refer the sensors installed on the Pacific islands as "PacNet sensors" and the sensors in North America as "conventional sensors", although PacNet is a combination of both.

continuously monitors lightning activity associated with convective storms across the central and eastern Pacific Ocean, north of the equator. Additional sites will be added in the near future, expanding the network to the western Pacific.

Although PacNet sensors are specifically designed for long-range detection, the concept of this “long-range lightning detection network” is broader than just these sensors, since the processing algorithm also incorporates sensor data from conventional sensors. The long-range location-processing algorithm identifies and accepts sensor data produced by both ground-propagated waves and ionospheric reflections that are rejected by the short-range algorithm used in NLDN and CLDN.

The raw (sensor) data from PacNet sites are transferred to Vaisala’s Network Control Center in Tucson, Arizona, via the Internet, where they are processed in combination with the NLDN and CLDN sensor data. The strike locations and times are computed using the individual sensors’ raw data, and final products are disseminated to users via the Internet.

### **2.3. Assessment of PacNet sensor performance**

For quantitative applications of the PacNet/LLDN data stream, the detection efficiency (DE) and location accuracy (LA) of the network must be assessed, and then an accurate model of these characteristics constructed.

The percentage of lightning flashes reported by long-range lightning detection networks depends on the strength of the lightning discharge, solar angle, the distance between the lightning flashes and the sensors, specifics of the hardware, and the nature of

the waveguide, discussed further in this Section. This flash detection efficiency (DE) is defined as

$$DE(x,y,t) = \frac{\text{number of flashes detected}}{\text{actual number of flashes}} \times 100\% \quad (1)$$

The LLDN DE is generally best during the night and is poorest during the day. The lower-loss propagation at night is the result of improved ionospheric reflection (Fig. 1.1).

LA is determined by the locations of sensors, the probability of detection by a specific group of sensors, and the time and angle error statistics (standard deviations) of the detected signals.

Basic sensor characteristics have been determined using data from a PacNet test sensor located in Tucson, Arizona, collected for one week in 2002. These data were compared to NLDN data collected during the same week in which a strong midlatitude storm system, with attendant squall lines, propagated from the High Plains across to East Coast, providing robust lightning strike data from a range of distances.

The ionospherically reflected signals have different waveforms than typical ground waves produced by CG lightning return strokes (Fig. 2.4). Note the sharp initial downward peak and short peak-to-zero time for the ground wave at 264 km (Fig. 2.4a). At a distance of 860 km, Figure 2.4b shows a distinct initial downward ground wave followed by a single-hop ionospheric reflection of opposite polarity (Kelso, 1964). At a distance of 3400 km (Fig. 2.4c), the waveform is determined by multiple ionospheric components, but there is evidence of a very small initial downward ground wave, a

slightly larger first-hop (inverted) sky wave, and a larger downward second-hop sky wave (at  $\sim 520 \mu\text{s}$ ). Although this distant signal contains clear sky-hop components, its overall waveform would be best-described using mode theory (Wait 1996). Since the field produced by a return stroke generally changes polarity at each reflection, the original polarity of the reflected waves cannot be readily determined, unless the ground wave is clearly identifiable.

The discharges detected by PacNet/LLDN are predominantly CG return strokes. Intracloud discharges have typically much weaker peak current than CG strokes and remain below the detection threshold. Ogawa and Brook (1964) reported typical current amplitudes in cloud flashes of 1-4 kA. Murphy et al. (2006) used an LF sensor and the Lightning Detection And Ranging (LDAR) VHF lightning mapping system (Mazur et al. 1997) in Florida and observed that the majority ( $\sim 70\%$ ) of all LF pulses from cloud discharges have amplitudes less than 1% ( $\sim 0.2$  kA) of the typical first return stroke ( $\sim 20$  kA) in a CG flash. Only the largest 1-2 pulses in each flash showed amplitudes equivalent to  $\sim 1$  kA.

However, intracloud discharges can be sometimes accompanied by a short-duration, relatively high-amplitude electric field change emissions termed narrow bipolar pulses (NBPs) (e.g. Smith et al. 1999). NBPs typically have much higher amplitude than the majority of cloud discharges ( $\sim 70\%$  of a typical CG return stroke) (Smith et al. 1999). These events are relatively rare. Murphy et al. (2006) noted that NBPs constituted less than 1% of the cloud pulses. Smith et al. 2002 used the Los Alamos Sferic Array (LASA) and found that  $\sim 1.4\%$  of the  $\sim 900,000$  events located by the sferic array

produced distinctive NBPs. Shao et al. (2006) used also LASA to investigate thunderstorms in Florida and found that among 34,000 flashes, there were ~1.2% NBPs. These events are the subject of ongoing research.

### 2.3.1. Signal attenuation

As discussed in Section 2.1, long-range propagation of lightning sferics involves a complex interaction between the earth and the ionosphere. The behavior of this propagation medium varies with time-of-day, conductivity of the earth path, and (to a lesser degree) season and direction. Since we are primarily interested in a “first order” characterization of propagation over salt water, it is reasonable to simply partition propagation into two conditions: day and night. It has been shown that propagation characteristics between two widely separated locations (both attenuation and phase changes as a function of frequency) transition fairly continuously from the daytime behavior to the nighttime behavior, over a period of 2-3 hours, as will be discussed later in this Section.

The propagation characteristic that directly affects peak signal strength is the amplitude attenuation as a function of frequency and distance. This can be approximated by the expression

$$A = \frac{\alpha}{R} \sqrt{\left(\frac{\theta}{\sin(\theta)}\right)} \exp\left(-\frac{R}{\lambda}\right). \quad (2)$$

This attenuation function is a dimensionless scaling function, where  $\alpha$  is a scaling constant,  $R$  is the distance along the earth surface between the lightning discharge and a remote sensor,  $\theta = \frac{R}{R_e}$ , and  $R_e$  is the radius of the earth (Al'pert, 1963). The space constant ( $\lambda$ ) or e-folding distance (the distance at which propagation losses reach 1/e) is primarily dependent on the conductivity of the earth-portion of the path and the electron density profile in the atmosphere. This expression is a simplification of the general propagation models described by Wait (1968) and others, but empirical evidence suggests it captures the average behavior of broadband sferics over modest propagation distances (<4000 km).

The attenuation rate was derived by time-correlating data from the test sensor with NLDN data collected throughout the U.S., and comparing the lossless signal strength (determined by the NLDN estimated peak current and the known distance) with the peak field strength measured by the test sensor. The analysis of signal strength shows the expected exponential loss in energy with distance (Fig. 2.5), where the average relative field strength (filled circles) is normalized by the estimated NLDN peak current. The standard deviation error bars show larger errors in the range of 2000-3500 km, where propagation involves a mix of 1<sup>st</sup> and 2<sup>nd</sup> hop ionospheric propagation (see Section 2.3.2 and Fig. 2.6). The daytime e-folding distance shown in Figure 2.5a is 10,000 km, and the nighttime e-folding distance is 40,000 km (Fig. 2.5b).

The distinct separation of timing between ground-, first-hop-, and second-hop waves can be used to identify the wave type (Fig. 2.6). Within ~500 km of the sensor,

nearly 100% of the signals are ground waves. Beyond that, the percentage of the first-hop waves increases sharply, whereas the ground wave percentage decreases. They become equal at 900-1000 km. As noted earlier, the error bars for the observations of relative signal strength with distance are greatest at distances where there is significant overlap in the wave types (compare Figs. 2.5 and 2.6). The addition of a signal processing capability within the sensor hardware to distinguish between the waveforms could reduce this uncertainty in future.

### *2.3.2. Timing and angle errors*

Timing errors were calculated by time-correlating data from the PacNet test sensor with NLDN data and comparing speed-of-light propagation time (determined from the NLDN stroke time and the known propagation distance) with the arrival time measured by the sensor (Fig. 2.7). These histograms were obtained by measuring the arrival-time delay of PacNet sensor reports relative to NLDN estimated stroke times measured with an accuracy of approximately one microsecond. All reports from one week of observations are included in this analysis. Figures 2.7a and c include reports with the same polarity as the NLDN peak current, and Figures 2.7b and d include opposite-polarity reports. The polarity reversal (relative to the polarity determined by the NLDN) occurs when the earlier signal components (ground wave, then 1<sup>st</sup>-hop, then 2<sup>nd</sup>-hop) fall below the fixed detection threshold of the sensor. The ground wave signal delay distributions (average  $\bar{x}$  and standard deviation  $\sigma$ ) were nearly the same for day and night

( $\bar{x}=20.0 \mu\text{s}$ ,  $\sigma=5.0 \mu\text{s}$  and  $\bar{x}=19.3 \mu\text{s}$ ,  $\sigma=4.7 \mu\text{s}$ , respectively) (Figs. 2.7a, c). The first-hop sky-wave distribution shifted from daytime value of  $52.9 \mu\text{s}$  ( $\sigma=4.7 \mu\text{s}$ ) to night value of  $70.5 \mu\text{s}$  ( $\sigma=4.0 \mu\text{s}$ ) (Figs. 2.7b, d). The second-hop distribution shifted from a daytime value of  $\bar{x}=90.0 \mu\text{s}$  ( $\sigma=5.1 \mu\text{s}$ ) to night value of  $\bar{x}=104.0 \mu\text{s}$  ( $\sigma=8.0 \mu\text{s}$ ) (Figs. 2.7a, c). Note that the polarity reversal of the first hop helps distinguish it from the ground-wave and second-hop signals, and that the signals delay distributions have almost no temporal overlap.

Angle errors were calculated by time-correlating data from the test sensor with NLDN data ( $150 \mu\text{s}$  time window) and comparing the true azimuth from the sensor (determined from the NLDN stroke location) with the azimuth measured by the sensor. An angle error histogram was derived from all time-correlated events with signal strengths from just above threshold to four times threshold (Fig. 2.8). The parametric fit has a mean value of  $-4$  degrees (resulting from an uncorrected antenna rotation and site errors due to local site conditions), and a standard deviation of  $4.5$  degrees. This value is conservative since it includes polarization errors and the variation of the local site error around its mean value.

### *2.3.3. Diurnal variation*

As noted earlier, propagation characteristics between two widely separated locations (both signal attenuation and phase changes as a function of frequency) transition fairly continuously from the daytime to the nighttime behavior, over a period of

2-3 hours. This fact has been confirmed through analyses of arrival-time delay and relative amplitude as a function of time-of-day for a portion of the PacNet sensor test period. For one 48-hour observation period (hours 96 through 144), all lightning was at least 900 km from the test sensor (diamond symbols in Fig. 2.9). The plateau in the time-delay time series (Fig. 2.9a) at  $\sim 50\text{-}55 \mu\text{s}$  reflects the behavior during daytime propagation when the D-layer extends lower in the ionosphere (Section 2.1). The plateau at  $\sim 70\text{-}75 \mu\text{s}$  reflects the behavior during nighttime propagation. Note the rapid and smooth transition between the two stable conditions that occurs during day-night transitions.

The PacNet “current” estimate (Fig. 2.9b) employed the propagation model in Eq. (2), using an e-folding distance of 10,000 km (representative for daytime propagation). This value is typically between 0.5 and 1.0, with random variations that can be larger than the day-night variability. The extent of these random variations is correlated with the variation in propagation distance, as one would expect. Note that for the hours 132-144, when most of the lightning is in the (narrow) range of 1500-2500 km, the random variability gets rather small. We note that this is the “sweet spot” range for one-hop propagation (see Figs. 2.6 and 2.7).

In addition, the behavior of PacNet DE during the transition periods between night and day over the Pacific was investigated, using the LLDN. Ground waves from flashes within 800 km of Hawaii were used as reference data. The two Hawaii sensors detected these events and the ground wave propagation was assumed to have no diurnal variation. The same events detected by distant sensors (excluding Hawaii sensors) were assumed to

be sky waves, since all other sensors were more than 2400 km away. Hourly relative DE values were obtained by comparing the number of sky wave events to the number of ground-wave events near Hawaii (Fig. 2.10). The diurnal variation of DE can be written

$$DE_{d/n} = \frac{\frac{S_d}{G_d}}{\frac{S_n}{G_n}} = \frac{S_d}{G_d} \cdot \frac{G_n}{S_n}, \quad (3)$$

where S and G are the number of flashes detected using sky waves and ground waves, respectively. The indices d and n refer to day and night, respectively.

In Figure 2.10, the nighttime maximum DE begins to drop at ~0300 Hawaii local time (LT), when the U.S. west coast sensors are in dawn. The lowest DE is reached at 0600 LT when the whole path from Hawaii to North America is in daylight. This continues until 1500 LT, when the North American sensors reach the dusk, and DE starts to enhance. The maximum DE is reached at 1800 LT when the whole propagation path is on the night side again. The relative DE during the day drops to ~20% of the night value. It should be noted that the diurnal variation shown in Figure 2.10 over this test configuration area near Hawaii is close to its upper limit, as the nearest non-Hawaii sensors are >2400 km away. For quantitative applications of the PacNet data stream, such as numerical modeling, a linearly interpolated curve can be fit to the observed diurnal variation (see Fig. 2.10).

#### **2.4. Modeling detection efficiency and location accuracy**

As mentioned at the outset of Section 2.3, quantitative applications require assessment of the detection efficiency (DE) and location accuracy (LA) of the network,

followed by construction of an accurate model of these effects. A calibrated model of DE and LA allows these important parameters to be estimated throughout the domain of the network. As discussed in the Section 2.3, there are a numerous factors that determine the DE of an LLS.

Specific examples of LLS DE are stroke  $DE_s$  (the fraction of all strokes, including first and subsequent) and subsequent stroke  $DE_{su}$  (excludes first strokes). Flash  $DE_f$  is unique in that a flash is reported (detected) if at least one stroke (first or subsequent) is detected. Therefore flash  $DE_f$  can be much higher than any form of stroke DE.

In this Section, the key parameters that determine the DE of individual sensors are defined, providing a framework for calculating DE for a given network geometry. This is followed by empirical derivation of the model parameters used to produce DE performance predictions for PacNet/LLDN.

The task of lightning detection begins with the electromagnetic field produced by the lightning discharge. In the case of CG lightning being detected at VLF/LF frequencies, the peak field strength (electric and/or magnetic) is roughly proportional to the peak current of the return stroke (Cummins et al., 1998b). The magnitude of the resulting field at a remote sensor location, which establishes the detectability of the signal by that sensor, is determined by three factors: (1) the attenuation of this field strength associated with normal propagation, (2) additional losses due to finite conductivity along the propagation path, and (3) imperfect (loss) ionospheric reflections. Once this attenuated signal reaches a remote sensor, it must exceed the detection threshold of the

sensor, which is determined by sensor gain, threshold setting, and local noise. To obtain a location for the lightning discharge, the signal must be seen by a sufficient number of sensors, which depends on strike point location (relative to the detecting sensors), and on the applied location method (MDF, TOA, or combined).

A graphical depiction of the detection process that is amenable to direct modeling is shown in Figure 2.11. The first step involves the occurrence of a CG stroke with peak current  $I_0$ , selected from the probability distribution  $P_1$  (the peak-current distribution). The peak electric and/or magnetic field produced by the stroke, having traveled a distance  $r_i$ , then reaches sensor  $S_i$  with incident signal  $SS_i$ . The probability of the sensor detecting this stroke is defined by the sensor DE function, illustrated in Figure 2.11. Note that there is a minimum signal strength (detection threshold) below which no events are detected, and that the maximum detectability is not reached until the signal is a bit larger than the detection threshold. Note also that as signal strength increases further, the DE decreases and eventually returns to zero when the sensor “over-ranges” and is no longer able to provide reliable information. Since each sensor that detects a specific stroke will be at a different distance, they may all have different sensor DE values for this stroke. Using the assumption that each sensor responds independently from all other sensors, these DE values are independent for each sensor. Based on this assumption, and by defining the probability of sensor  $S_i$  not detecting the event as  $Q_i(I_0) = 1-DE_i(I_0)$ , then the probability of a specific combination of sensors detecting the event is simply the product of the appropriate  $P_i(I_0)$  and  $Q_i(I_0)$  values for all sensors. For example, the probability  $P$

that a stroke with current  $I_0$  is detected by a minimum of 2 sensors of a 3 sensor network, is

$$P = [DE_1(I_0) * DE_2(I_0) * Q_3(I_0)] + [DE_1(I_0) * Q_2(I_0) * DE_3(I_0)] + [Q_1(I_0) * DE_2(I_0) * DE_3(I_0)] + [DE_1(I_0) * DE_2(I_0) * DE_3(I_0)] \quad (4)$$

Using this construct, it is possible to determine the probability of detection for any specific number of sensors in a network of arbitrary size.

To produce a modeled overall DE estimate for a region, the region of interest is typically broken up into a set of rectangular grid cells. For a point in the center of each cell, and for each possible peak current value, the model must determine the DE for each sensor. To determine the overall network detection efficiency for a specific peak current and grid point, one simply sums the probabilities for “N” or more sensors detecting a discharge, where N is the minimum number of sensors required by the network to locate a discharge. For networks that employ MDF in combination with TOA, N is two. For networks that employ direction finding by itself, N is 2-3, depending on the stroke location relative to the sensors locations. For networks that employ only the TOA method, N is 3-4. The overall DE is determined from the sum of DE values for each current value ( $I_0$ ), weighted by their probability of occurrence taken from the peak current distribution  $P_i$ .

This general parametric model has been employed over the past 15 years to estimate LLS performance. Recent validation of the model (for CG lightning detection in the U.S. involving ground-wave propagation paths) is provided in the work by Biagi et al. (2007).

To summarize, the fundamental information required to accurately model network DE is the distribution of peak currents, the detection threshold characteristics of the sensors, the propagation conditions (regional conductivity and ionospheric conditions) and knowledge of the location method (2, 3, or 4 sensors required to get a location). The detection threshold characteristics of the sensor are strictly a function of the incident peak field strength and the gain of the sensor. The characteristics have been determined in a laboratory setting and confirmed in field tests performance by the sensor manufacturer (Vaisala). The location method employed in this network is the IMPACT method which combines time-of-arrival and direction finding, so only two sensors are required to detect a stroke for it to be reported by the network.

#### *2.4.1. Estimation of DE model parameters for salt-water path*

The form of the propagation model provided in Eq. 2 was shown to be a reasonable approximation of the observations from NLDN and a PacNet test sensor located in Arizona. To estimate DE for the LLDN, the two remaining parameters (peak current distribution and propagation characteristics; i.e., space constants) were needed for salt-water path conditions. These parameters were obtained by comparing recent information produced by the LLS operated by the Puerto Rico Electric Power Authority (PREPA) with information produced by the LLDN in the western Atlantic Ocean. The PREPA network is a short-baseline network comprised of five low-gain IMPACT sensors installed in 2003. Based on analyses performed by Vaisala, this network has a CG flash

DE in excess of 95% over Puerto Rico and nearby surrounding waters, and a median location error of 500 m or less. The western Atlantic portion of the LLDN operates with the same location algorithm configuration as the PacNet network in the Pacific, but this region is too distant from the four PacNet sensors to derive any value from them.

It has been shown (Orville and Huffines 2001) that the median peak current value for negative first strokes, inferred from LLS measurements, are somewhat larger when a stroke impacts salt water than when it strikes ground. It is unknown whether this enhancement is the result of a change in the relationship between peak field and peak current over salt water, or an actual increase in peak current in the channel. Either way, this effect produces a change in the population of source signals over salt water that needs to be accounted for when estimating LLS DE over the oceans.

To account for this salt-water effect, the peak current distribution was constructed using negative first strokes obtained from the PREPA LLS for the calendar year 2006 (Fig. 2.12), obtained from the "Sea" region surrounding Puerto Rico (Fig. 2.13c). A PREPA CG lightning stroke was considered to be detected by the LLDN if it occurred within 350 microseconds of the CG stroke detected by the PREPA network.

Since LLDN DE varies as a function of day and night, CG flash and stroke DE were computed as a function of peak current for both day and night. Daytime (night-time) statistics were only computed between the hours of 12 (00) and 22 (10) UTC, when the propagation path between Puerto Rico and the LLDN sensors was all daylight (night), with no terminator crossing between Puerto Rico and LLDN sensors. LLDN DE was

defined as the percentage of PREPA CG flashes detected by the LLDN. The observed flash DE values were 4.7% for day and 20.8% for night.

#### *2.4.2. Refinement of DE model using Puerto Rico observations*

The attenuation rate in the DE model (see Eq. 2) were adjusted (2000-km space constant during the day and a 6000-km space constant for night) so that the predicted DE (~5% day and ~21% night) was consistent with the observed DE (Fig. 2.13), given the observed salt-water peak current distribution in the vicinity of Puerto Rico (Fig. 2.12). Note that these space constants are smaller than those observed for the PacNet test sensor, which reflects that lesser performance of the NLDN sensors.

The refined DE model was then applied to the PacNet/LLDN sensor distribution in the central North Pacific (Fig. 1.2), with the resulting predicted DE distribution shown in Figure 2.14. In applying the refined DE model to Hawaii, it is assumed that the weather regime in the two locations, in a prevailing trade-wind belt, will produce similar peak current distributions. In this regard, it should be noted that during the period of Puerto Rico data analyzed, no tropical cyclones passed through the region studied. In Section 2.5.1 comparison between observed and predicted DE in the vicinity of Hawaii will be presented to test the validity of this assumption.

### *2.4.3. Modeling location accuracy*

As described by Cummins et al. (1998b, Appendix) the median estimated location accuracy is defined as the semi-major axis of a location error ellipse. For the PacNet/LLDN LA model, the ellipse is computed for each element of a 75x75 point grid, and is determined by sensor locations, probability of detection by specific groups of sensors (DE model), and the time and angle standard errors. The timing and angle errors characteristics were derived empirically using the PacNet test-sensor data, described in Section 2.3. The errors were parameterized as the standard deviation of a normally distributed random variable (Figs. 2.7 and 2.8), resulting in a 5  $\mu$ s RMS timing error value and an angle error of 4.5 degrees RMS employed in the LA model.

The resulting modeled LA distribution is mostly between ~2 and 16 km between Hawaii and North America, increasing to 64-128 km near the dateline over the North Pacific Ocean (Fig. 2.15). Areas of poor LA occur to the northwest and southeast of Hawaii, which lie on the extension of the baseline between the two Hawaii sensors. The modeled LA for the area to the southeast of Hawaii is especially large due to the absence of additional sensors in that direction. The Unalaska or Kwajalein sensors improve performance slightly to the northwest of Hawaii.

### **2.5. Observed performance of PacNet/LLDN**

The performance of PacNet/LLDN was assessed using data from NASA's Lightning Imaging Sensor (LIS) onboard the Tropical Rainfall Measuring Mission (TRMM)

satellite. Both DE and LA were evaluated using time-correlated LIS flashes with PacNet/LLDN data. Three years of LIS and PacNet/LLDN data were used to assess the performance (DE and LA) of PacNet/LLDN over the central Pacific (February 2004 – February 2007).

Only days when at least three PacNet sensors (Unalaska, Lihue, Kona + LLDN) were up were included in the analysis. In addition, PacNet/LLDN data were filtered by removing multiple events. A single lightning strike is often detected as two or more PacNet/LLDN events. Multiple sky-wave locations are possible, because more than one "collection" of sensors can experience a group-consistent propagation path delay. In contrast, there is only one (or zero) ground-wave location. The ground-wave events can usually be identified as the earliest event (~30-200  $\mu$ s earlier), and (for the region near Hawaii) only being seen by 2-3 sensors. The time difference between LIS and LLDN events is determined by which "hop" triggered the sensor reports, time-of-day, the distance between the sensors and the strike-point, and the difference in the location calculation.

Location error ( $\Delta D$ ) results in a timing difference having a maximum of  $\Delta D \cdot (3.3 \mu\text{s km}^{-1})$  and a minimum of zero, depending on the geometry of the network and the location errors. If we assume a maximum location error of 300 km, then the time difference is less than one millisecond. Expected time differences due to propagation alone are generally less than 200  $\mu$ s. Time differences greater than 1 ms are probably different strokes in the flash, which can strike the ground up to 7-10 km away from the first stroke.

The PacNet/LLDN stroke information includes three quality parameters. (a) *Chi-*

*Square* is the average squared-normalized angle- and time deviations (from the optimized location) for the sensors that participated in each specific stroke location. This tells if reasonable angle and time deviations were assumed. In an ideal world, the mean and standard deviation for a large population of these values are 1.0. (b) *Error Ellipse Semi-major Axis (SMA, in km)* is the SMA of the error ellipse for the expected location error for each stroke, determined from the actual sensors reporting the stroke and their positions relative to the stroke location. This is also the parameter that is plotted in the LA performance modeling. In that case, we normally assume that all sensors within a specified range will detect the stroke. This assumption is a problem for PacNet/LLDN, given the size of the network. The special LA model weighs each combination of two or more sensors by their DE (probability of occurrence). (c) *Average Number of Sensors Reporting (NSR)* is the average count of sensors that participated in the stroke location calculations. The minimum number is two (for IMPACT sensor networks). When there is a large NSR, either the DE is quite high or only high-current strokes are located at a great distance from the sensors. The spatial distribution of this value gives insight into the actual behavior of the network.

When more than one LLDN stroke location is time-correlated with a LIS flash, the above error statistics are applied to select between multiple PacNet/LLDN locations.

### 2.5.1. Observed detection efficiency

The DE over the central Pacific was assessed over two areas: near Hawaii (20-26°N;

149-159°W) and over the central-north region (28-38°N; 150-160°W) (Fig. 2.14). The total number of LIS and PacNet/LLDN flashes occurring over the two areas were counted over the three-year period, February 2004 – February 2007. Both day and night DE were assessed. Day (night) data include all the flashes occurring between 9-15 (21-03) local time (LT) over each area. The six-hour time windows centered at midnight and noon were selected to avoid terminator effects in the propagation path.

Three different corrections were applied to LIS data to make the PacNet/LLDN and LIS flash rates comparable (i) LIS data were DE-corrected using values of 0.73 for day and 0.93 for night, according to Boccippio et al. (2002), (ii) LIS view time is a function of latitude, thus the flash rates were normalized for view time over the selected areas, and (iii) LIS reports were corrected for an estimated IC:CG ratio, since LIS detects both intracloud (IC) and cloud-to-ground (CG) flashes, whereas the strikes detected by PacNet/LLDN are predominantly CG (Section 2.3). The method to estimate IC:CG ratio is presented in Appendix.

Using the above approach, DE over the Hawaii region was calculated to be 21-22% during the day and 57-61% at night. DE over the central-north region varied between 17-19% during the day and 40-44% at night (Fig. 2.14)

The issue of infrequent LIS sampling was addressed using a 10% data deprivation study, also known in statistics as the Jackknife method. The PacNet/LLDN and LIS data were divided into ten similarly sized parts that were matched temporally. DE was computed ten times, with one part of the data missing during each computation. This yielded a mean DE for the Hawaii region of 23% for day and 61% for night with standard

deviations of 4% and 7%, respectively. For the central-north region, the mean DE was 22% for day and 45% for night with standard deviations of 12% and 7%, respectively. Compared to the computations with the original full data set, these values are within 1% for the Hawaii region and within 3% for the central-north region.

The observed DE of 17-22% for day and 40-45% for night over the central-north region is in relatively good agreement with the DE model (Fig. 2.14), although the variation is large for daytime using the Jackknife method. Over the Hawaii region, the observed DE of 21-23% for day is lower than modeled, and observed DE of 57-61% for night is higher than modeled (Fig. 2.14). It is suggested that the underestimate of the daytime DE is because of partial blockage of ground waves by high terrain to the north and east of the Kona sensor. Slightly higher DE at night may simply be a reflection of the longer space constants that characterize the performance of the PacNet sensors in Hawaii.

### *2.5.2. Observed location accuracy*

Location accuracy (LA) is defined as the difference between the actual flash location and the location the LLS observes. The location accuracy (LA) of PacNet/LLDN was assessed using LIS data. LIS flash location is an optical centroid with nadir and limb resolutions of 4 and 6 km, respectively. Therefore, the results from the LA analysis need to be interpreted cautiously, considering the resolution of LIS data. The great-circle distances between all the PacNet/LLDN and LIS flashes occurring within  $\pm 1$  ms time window were computed. The timestamp in the LIS flash data is not corrected for transmitting delay, resulting in 2 ms bias in the dataset (D. Boccippio 2007, personal

communication). Therefore, PacNet/LLDN events were temporally matched with LIS flashes that occurred within a 1-3 ms lagged time window of LIS time stamp. The SMA and chi-values represent the quality of the location, and if there are multiple locations within 1 ms, the flash with the smallest value of  $\frac{SMA}{\sqrt{\chi}}$ , ( $\chi \geq 1$ ) is chosen to represent the flash location. As the number of matching pairs was relatively small, LA was averaged over relatively large grid boxes to obtain a reasonable sample size. All the boxes were located between 25-38°N, with “east”, “central”, and “west” box boundaries of 140-155°W, 155-165°W, and 165-180°W, respectively. The median location accuracies over the east, central, and west boxes were 13, 35, and 40 km, respectively (see Fig. 2.15).

Calibration of PacNet/LLDN includes the calculation of site error corrections. Site errors are systematic angle errors caused by scattering of the received signals in the vicinity of the sensors (e.g., Krider et al. 1976; Hiscox et al. 1984). The calibration process relies on redundant information in the form of additional lightning sensors or an independent measurement source. Given that there are currently only two PacNet sensors in the central North Pacific (Lihue and Kona), existing site error corrections are challenging. Therefore lightning strikes near the baseline between the two Hawaii sensors may have large location errors when only these two sensors detect the discharge. By contrast, strikes away from the baseline can be accurately located, especially if additional sensors outside Hawaii participate in the detection. Strikes detected with more than two sensors are less sensitive to site errors due to the nature of the combined direction-finding and time-of-arrival methods (Cummins et al. 1998b). In practice, the

U.S. and Canadian sensors reduce the location errors over the eastern Pacific near the coast of North America.

## **2.6. Summary and conclusions**

The waveguide between the Earth's surface and the ionosphere allows VLF emissions generated by lightning to propagate over long distances. PacNet, as a part of a larger long-range lightning detection network (LLDN), utilizes this attribute to monitor lightning activity over the central North Pacific Ocean with a network of ground-based lightning detectors that have been installed on four widely spaced Pacific islands. PacNet/LLDN sensors combine both magnetic direction finding (MDF) and time-of-arrival (TOA) based technology to locate a strike with as few as two sensors. As a result, the PacNet/LLDN is one of the few observing systems, outside of geostationary satellites, that provide continuous real-time data concerning convective storms throughout a synoptic-scale area over the open ocean (Fig. 2.16).

The detection efficiency and location accuracy of PacNet/LLDN varies with time of the day and the location of the thunderstorm with respect to the sensors. Detection efficiency and location accuracy models have been developed and applied to quantify the lightning rates and locations over the North Pacific region. The model parameters were derived by comparing the waveforms arriving at a PacNet test sensor to NLDN lightning data spread throughout the continental United States. Lightning data from Puerto Rico were then used in conjunction with LLDN data to derive the salt-water peak current distribution and space constants for the DE model.

LIS data were used to assess the location accuracy and detection efficiency of PacNet/LLDN. The observed location accuracy was in the range of 13-40 km over the central North Pacific, in reasonable agreement with the LA model. The observed detection efficiency over the central-north region was 17-22% and 40-45% for day and night, respectively. These values were in good agreement with the DE model. In the vicinity of Hawaii, the observed DE was 21-23% and 57-61% for day and night, respectively. These values differ 10-20% from the modeled values. These discrepancies maybe due to unmodeled partial blocking of groundwaves by terrain during the day and the fact that the space constants associated with PacNet and NLDN sensors differ. As the geometry of the network evolves with the addition of new sensors, network DE and LA will be reevaluated in future.

In the next Chapter, observations from PacNet/LLDN are utilized alongside DE and LA models to study the characteristics of the North Pacific thunderstorms.



Figure 2.1 (a) Ground installation at Lihue airport, Kauai, (b) roof installation in Unalaska.

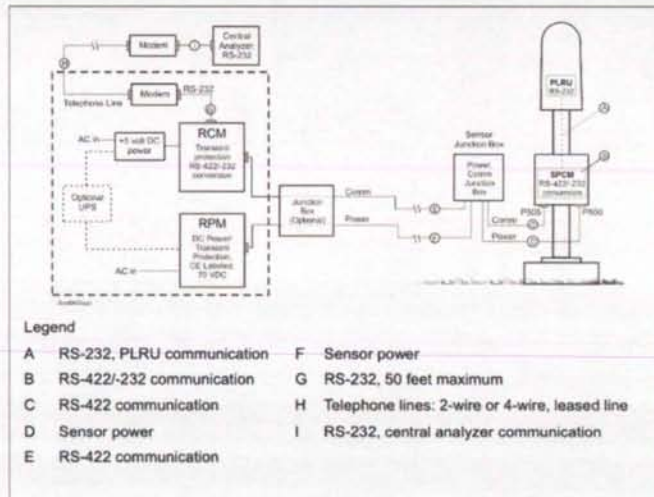


Figure 2.2 IMPACT-ESP sensor schematic diagram showing the relationship between the remote communications module (RCM), the remote power module (RPM), the primary line replaceable unit (PLRU) and the sensor power/communication module (SPCM).



Figure 2.3 Installation stage at Lihue airport. The magnetic direction finding loops are exposed at the top of the mast together with electric field and GPS antennas. Below them in the box is the main electronics module (PLRU). A laptop computer is connected to the sensor power/communication module to test the sensor. The power and communication cables are buried 90 cm below the surface.

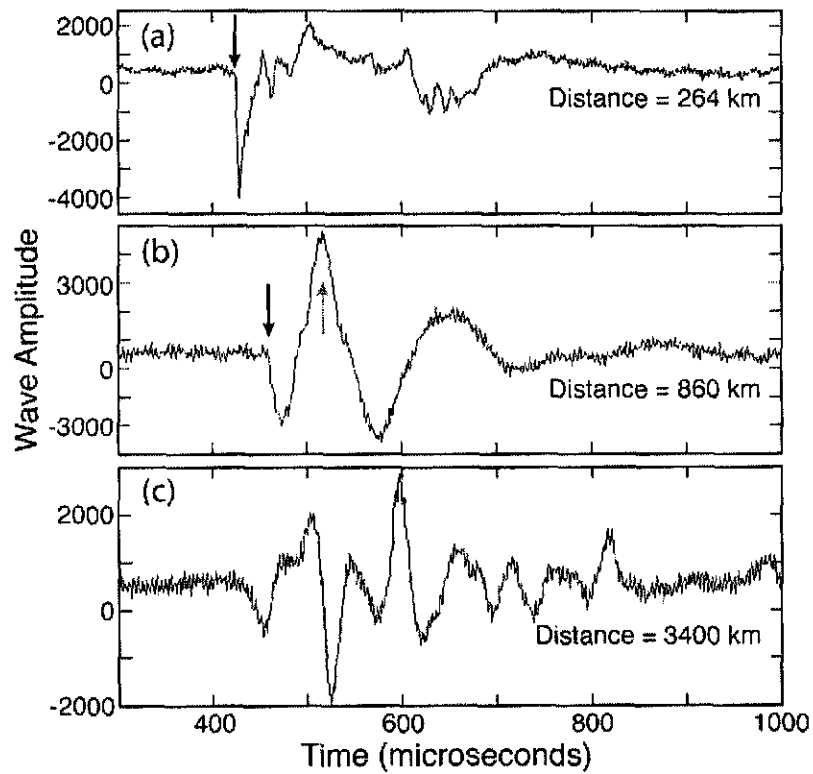


Figure 2.4 Vertical electric field waveforms for a cloud-to-ground return stroke detected by sensors located at 264, 860, and 3400 km from the lightning stroke. The amplitude scale is uncalibrated. Black arrows in a) and b) indicate initial appearance of the ground wave, and the gray arrow in b) indicates the single-hop reflected wave.

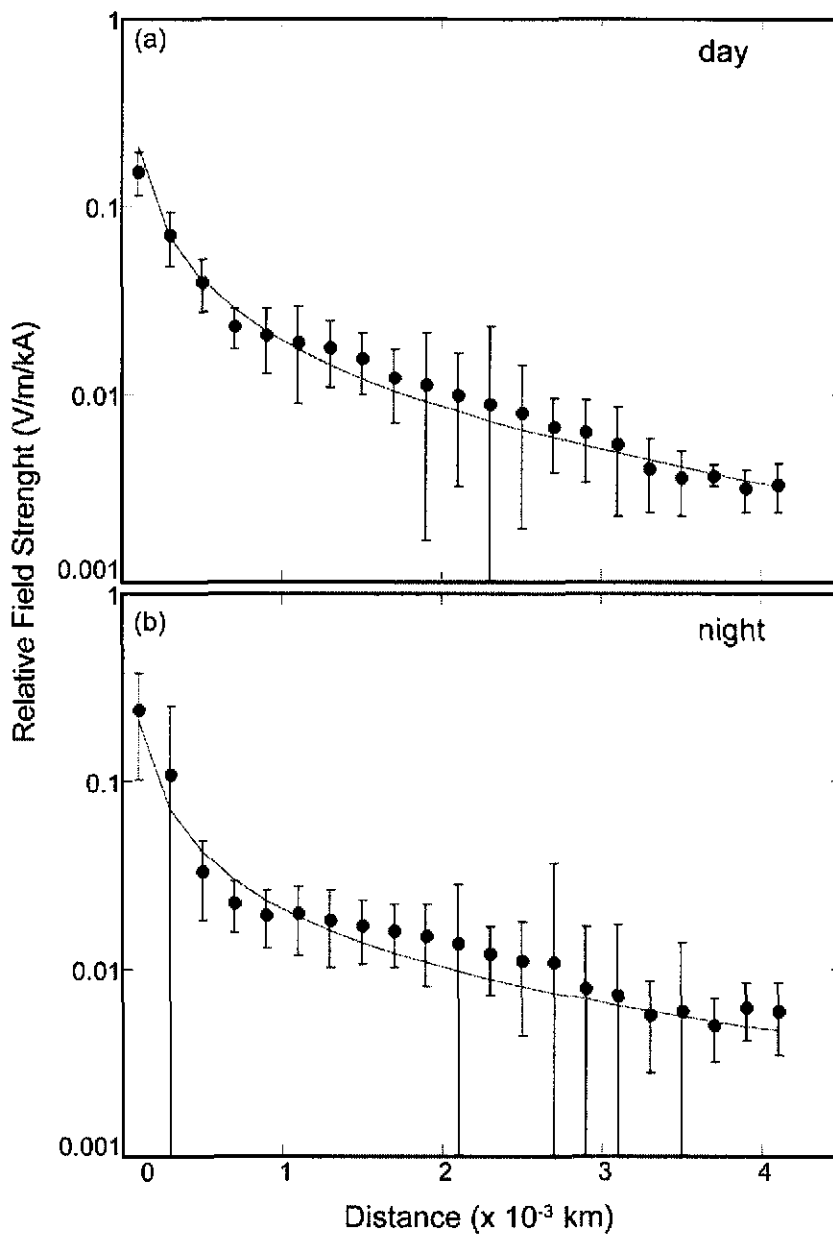


Figure 2.5 Relative signal strength as a function of stroke distance as detected by a PacNet test sensor located in Tucson, Arizona for (a) day and (b) night. The error bars are  $\pm 1$  standard deviation. The fitted curve shows the attenuation rate predicted by Eq. 2.

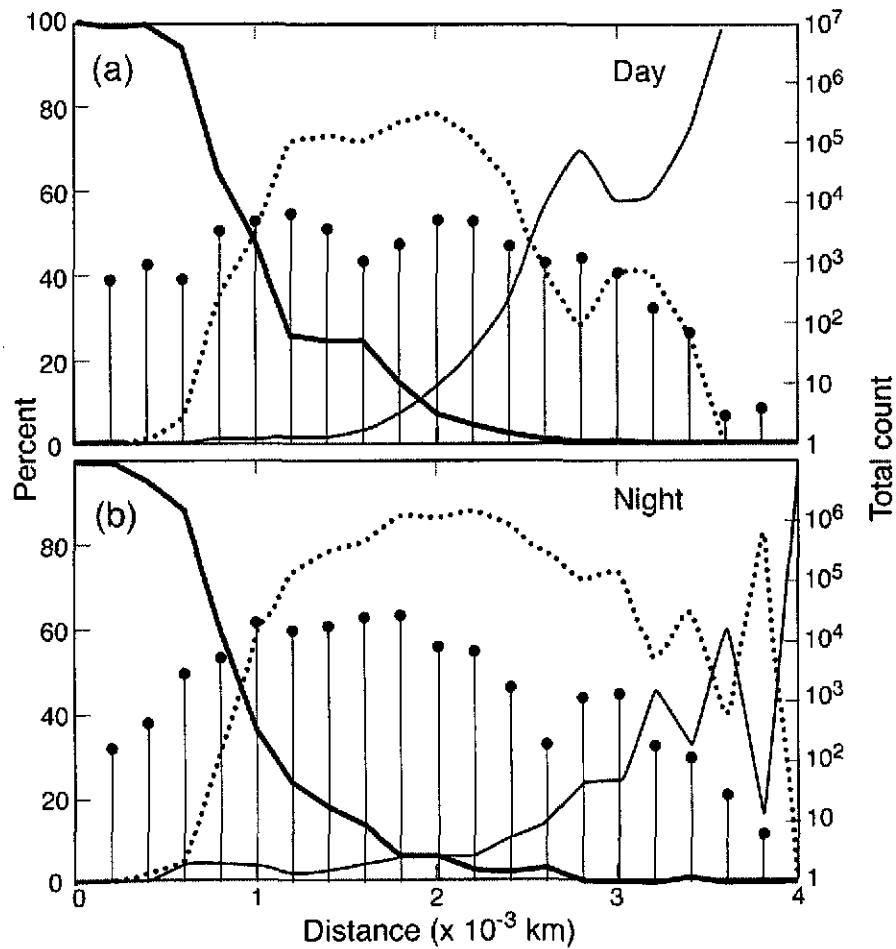


Figure 2.6 Percentage of different propagation types as a function of distance for (a) day and (b) night. Thick solid line is for ground wave, dashed for first-hop sky-wave, and thin solid for second-hop sky-wave. The bars indicate the total number of strikes detected in each 200 km distance bin (right ordinate).

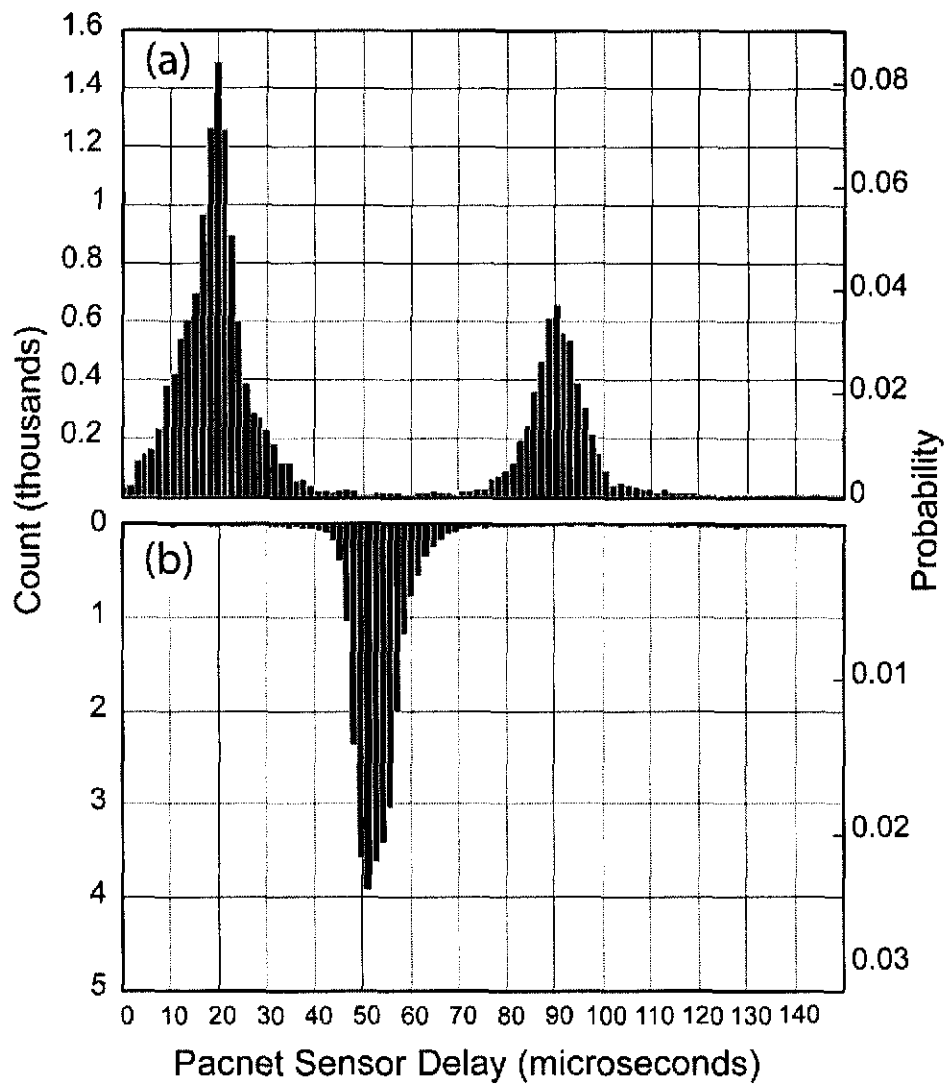


Figure 2.7 (a) Daytime ground wave signal delay distribution for is centered at  $20.0 \mu\text{s}$  and has a standard deviation of  $5.0 \mu\text{s}$ . Second-hop sky wave distribution is centered at  $90.0 \mu\text{s}$  ( $\sigma=5.1 \mu\text{s}$ ). (b) First-hop (inverted) sky-wave distribution is centered at  $52.9 \mu\text{s}$  and has a standard deviation of  $4.7 \mu\text{s}$  (graph inverted in reference to reversed polarity of first hop).

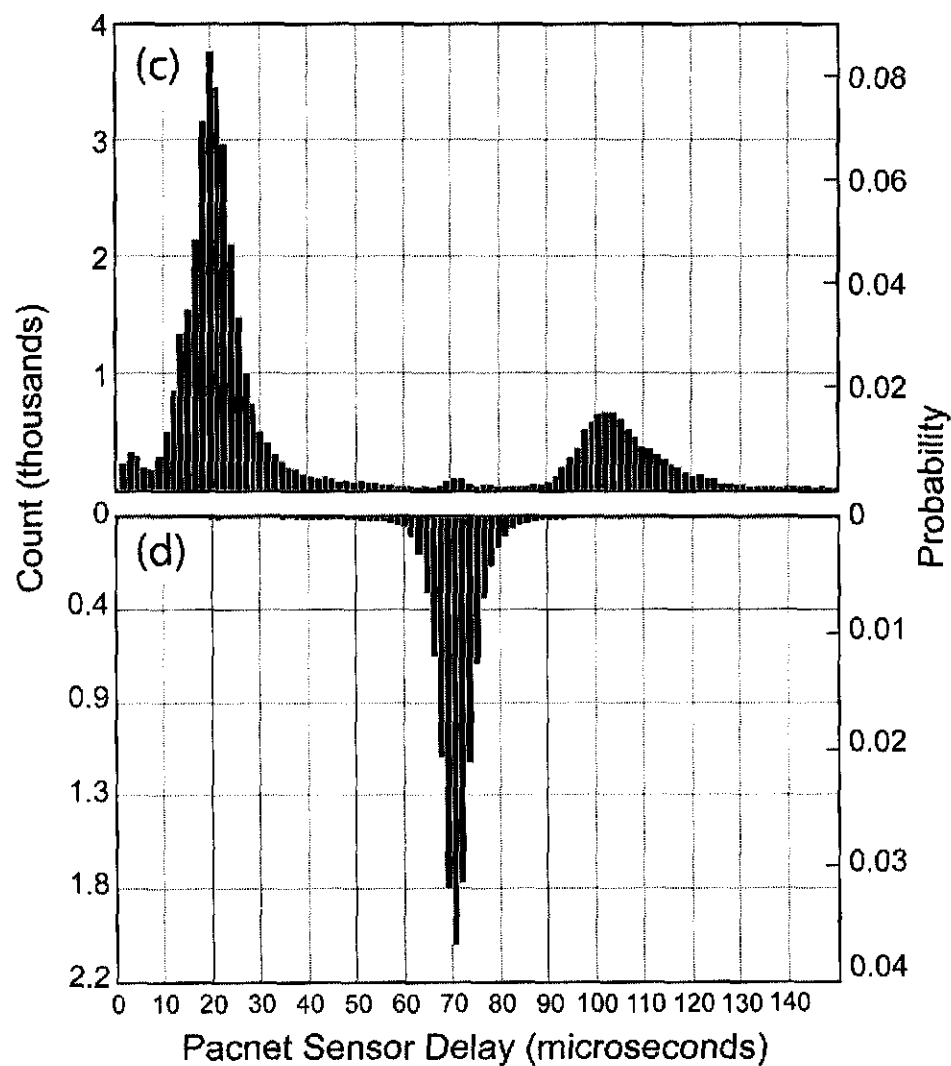


Figure 2.7 continued. (c) Night-time average for ground-wave distribution is  $19.3 \mu\text{S}$  ( $\sigma=4.7 \mu\text{S}$ ). Second-hop wave  $104.0 \mu\text{S}$ , with  $\sigma=8.0 \mu\text{S}$ . (d) First-hop distribution is centered at  $70.5 \mu\text{S}$  with  $\sigma=4.0 \mu\text{S}$  (graph inverted in reference to reversed polarity of first hop).

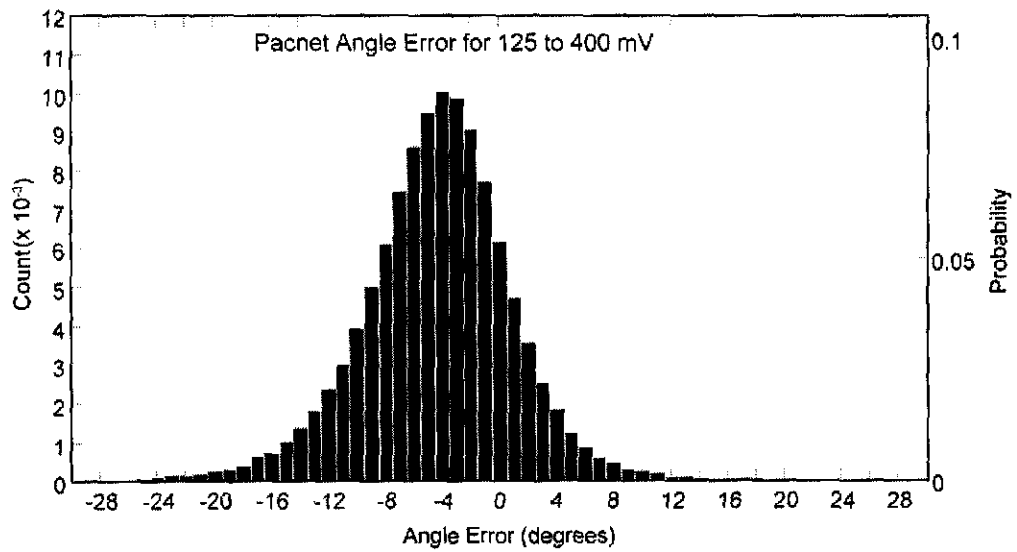


Figure 2.8 Angle error without site-error correction has a mean value of -4.0 degrees and a standard deviation of 4.5 degrees (for both day and night).

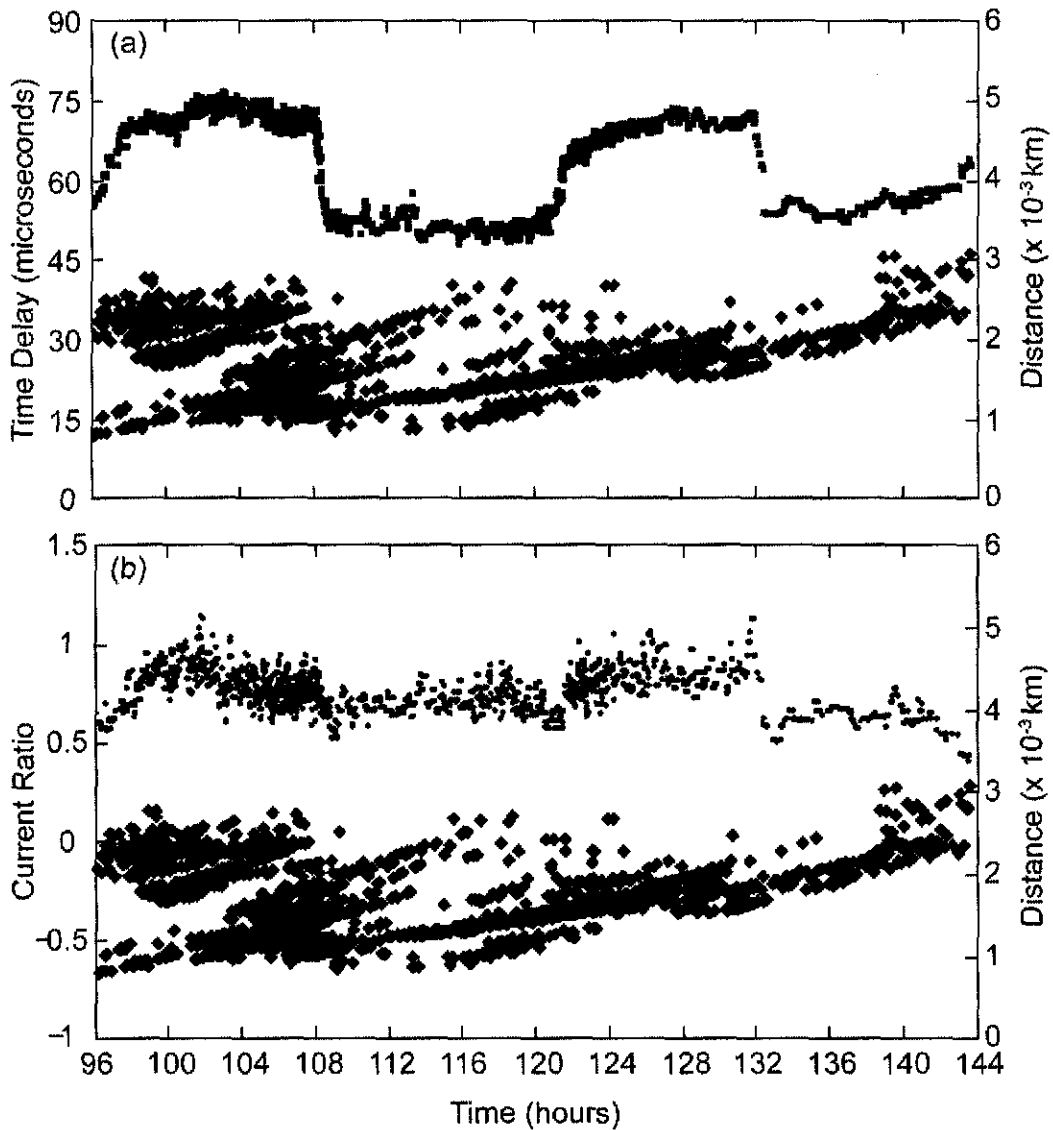


Figure 2.9 Time-series plots of (a) the variation of arrival-time delay of VLF signals observed by the PacNet test sensor in Tucson, AZ relative to time-of-occurrence of the CG stroke determined by the NLDN. Each symbol represents the median value of nine time-ordered events. (b) Peak current estimated using the PacNet sensor magnetic field peak, relative to NLDN estimated peak current. Diamonds in the lower part of each figure show the distance of the events from the sensor (right ordinate).

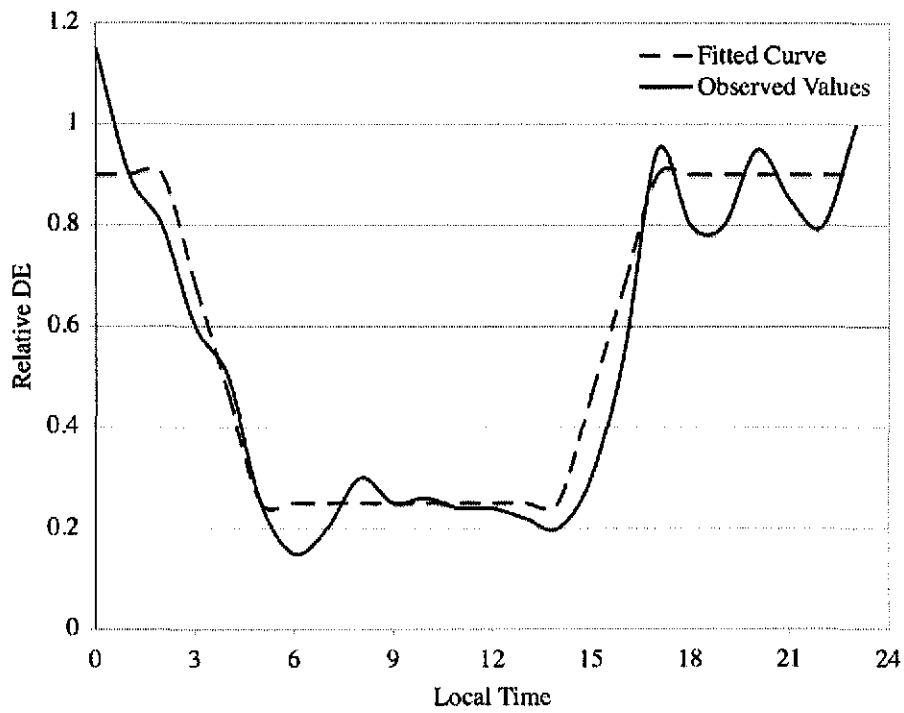


Figure 2.10 Empirically derived diurnal DE variation over the North Pacific (solid line) and fitted curve used for diurnal DE correction (dashed line). Since the actual DE of ground-wave events is not exactly known, the DE-scale (y-axis) is relative.

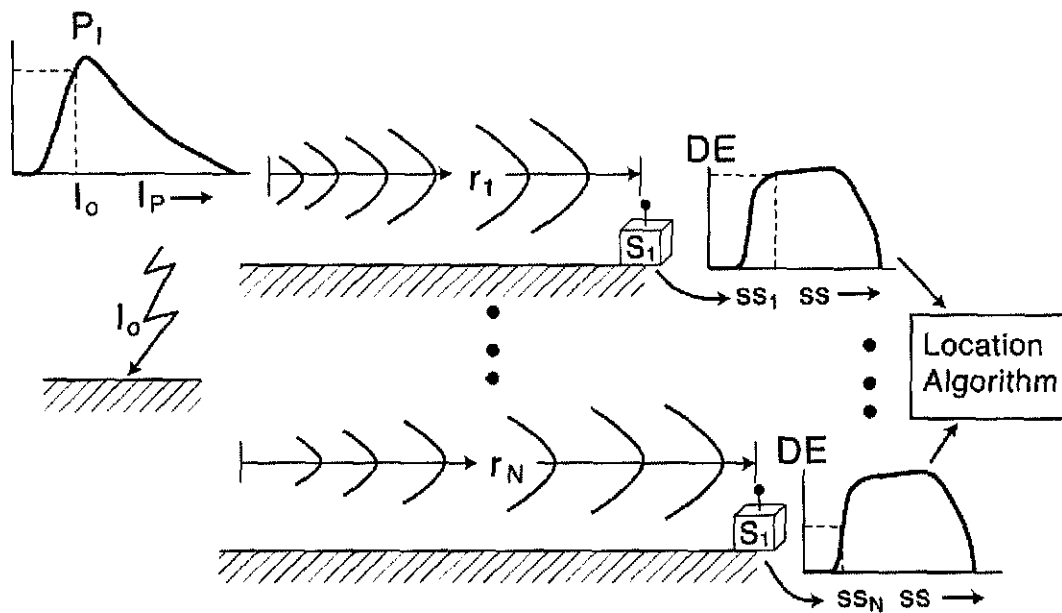


Figure 2.11 Simplified schematic for LLS network detection efficiency.  $I_0$  is the strike peak current,  $P_1$  is the peak-current probability distribution,  $r_1 \dots r_n$  are the distances between the strike and the sensors  $S_1 \dots S_n$ .  $SS_1 \dots SS_n$  are the incident signals at the sensors  $S_1 \dots S_n$ . If the DE threshold is met then the signal is passed on to a central location algorithm.

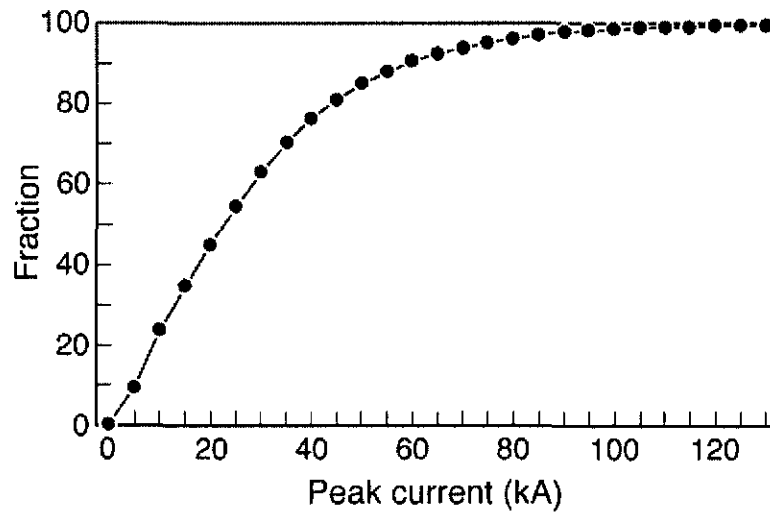


Figure 2.12 Cumulative peak current distribution derived from CG first strokes striking salt water near Puerto Rico.

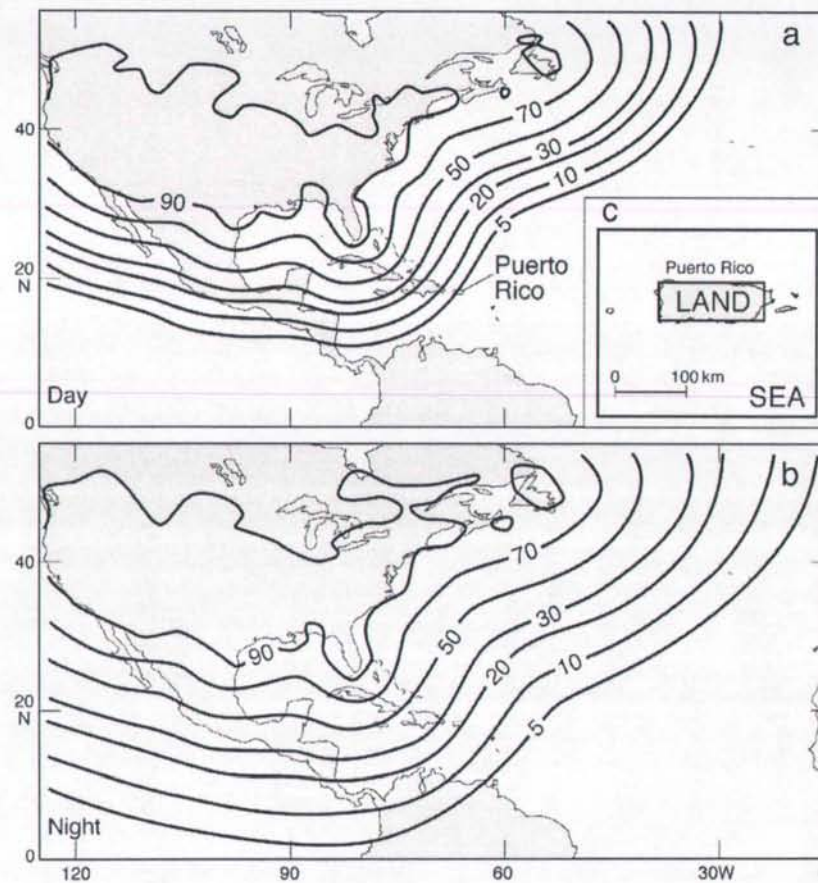


Figure 2.13 Results from the detection efficiency model show (a) 5% day and (b) 20% night DE over Puerto Rico when using the reference peak-current distribution and space constants of 2000 and 6000 km for day and night, respectively. (c) Insert: Lightning data analysis region for Puerto Rico. The salt-water region is the “Sea” region, with the exclusion of the “Land” region.

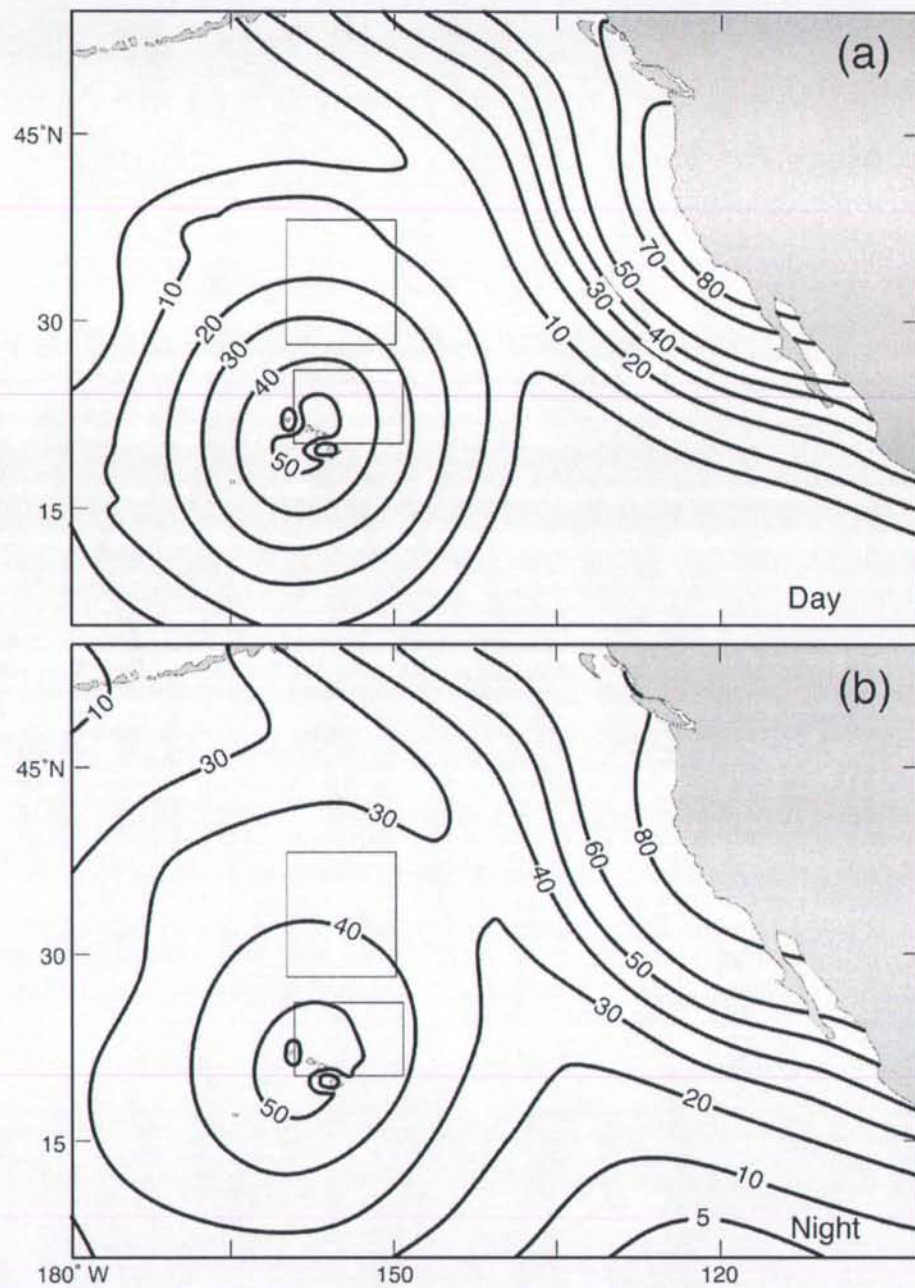


Figure 2.14 Modeled DE (%) over the Pacific during (a) day, and (b) night. The boxes show the areas where the observed DE was assessed. The observed values for the Hawaii region were 22% and 61% during the day and night, respectively (lower box). DE values for the central-north region were 19% and 44% for day and night, respectively (upper box).

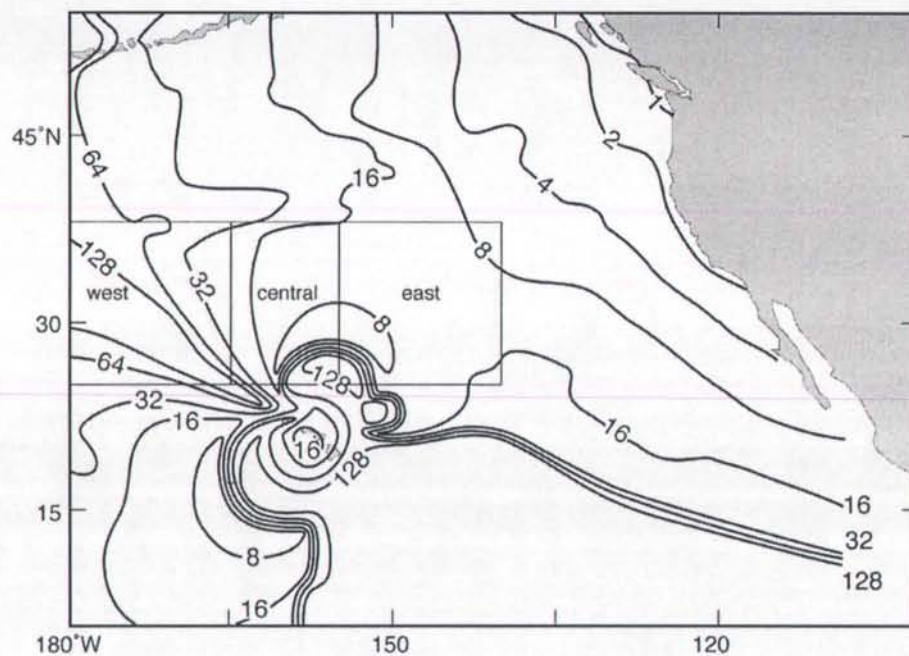


Figure 2.15 Modeled LA (km) of PacNet/LLDN with four PacNet sensors located in Alaska, Kwajalein, Lihue, and Kona. The boxes show the areas where the observed LA was assessed. LA over the west, central, and east boxes was 40, 35, and 13 km, respectively.

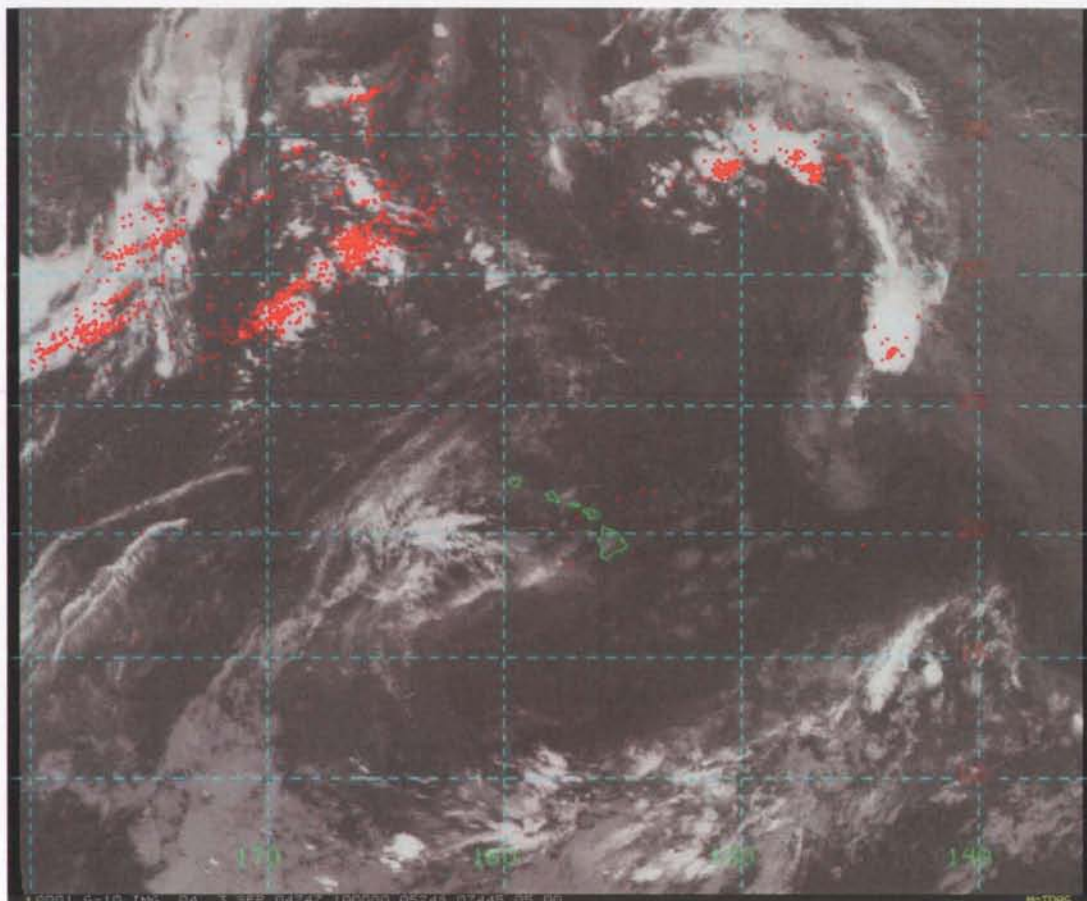


Figure 2.16 PacNet/LLDN lightning data (red dots) overlaid with GOES-10 infrared satellite image at 1000 UTC on 3 September 2004. Image processed by the author shows lightning active convective storms on the trans-Pacific air traffic routes between the U.S. west coast and Hawaii. Areas of intense lightning can be used to differentiate between cold cirrus and deep convection. Note that the impact of inferior network geometry on the location accuracy west of 160°W longitude is apparent in the image.

# CHAPTER 3. RELATIONSHIPS BETWEEN LIGHTNING, PRECIPITATION, AND HYDROMETEOR CHARACTERISTICS OVER THE NORTH PACIFIC OCEAN<sup>3</sup>

## 3.1. Introduction

A promising and important application of PacNet is to derive estimates of the rainfall rate and latent heating and hydrometeor profiles from lightning data over the Pacific Ocean that can be assimilated into numerical weather prediction (NWP) models. In areas of an NWP model domain for which the moisture content is underestimated, lightning data can contribute to forecast accuracy by adjusting the moisture fields and vertical profiles of latent heat release into the initial conditions and early forecast hours of the model in areas where lightning is observed (Alexander et al. 1999; Chang et al. 2001).

### 3.1.1 *Maritime vs. continental storms*

Numerous papers have documented the characteristics of oceanic storms and investigated the impact of various environmental conditions on storm development and electrification. Observational studies have documented convective storms over the

---

<sup>3</sup> Pessi, A. and S. Businger, 2008: Relationships Between Lightning, Precipitation, and Hydrometeor Characteristics over the North Pacific Ocean. *J. Appl. Meteorol. Climatol.* In review.

oceans that contain little or no lightning, but have rainfall rates similar to active thunderstorms over land (e.g. Wang 1963; Zipser 1970, 1994; Takahashi 1978b, 1990; Cram and Tatum 1979). Recently, satellite based lightning and rainfall measurements have confirmed these observations (e.g. Nesbitt et al. 2000; Toracinta et al. 2002; Cecil et al. 2005; Futyuan and DelGenio 2007a).

This discrepancy can be explained in part by the efficiency of warm rain process in the maritime environment (Pruppacher and Klett 1978). Maritime air mass typically contains less cloud condensation nuclei (CCN) than continental air mass and thus has different cloud microphysical characteristics. In air mass with high CCN concentrations (i.e., continental), more cloud drops form and these drops consume the available water vapor, keeping the supersaturation low. In air mass with low CCN concentrations (i.e., maritime) less drops form and supersaturation is higher (Fig. 3.1). However, the liquid water content remains nearly the same in clouds with low and high CCN concentrations (e.g. Porter 1988). The drops are larger and also the drop size spectrum is wider than in high CCN air mass. This results in a more efficient collision-coalescence process (Fig. 3.2). After the drops have grown to 25-30  $\mu\text{m}$  size by condensation, the collision-coalescence process is very efficient leading quickly to large drops and rainfall. Takahashi (1976) found that the total rainfall in his model decreased sharply when the total number of CCN exceeded  $150 \text{ cm}^{-3}$ . Warm rain process is entirely different from the rainfall initiation process typical in continental air mass, where water vapor supersaturation with respect to ice is the main process to initiate rainfall (Wegener-Bergeron-Findeisen mechanism).

Effective charging of hydrometeors in clouds to reach breakdown potential basically always requires ice particles and consequently, water or "warm" clouds rarely produce lightning. However, some warm-cloud lightning has been reported (Moore et al. 1960; Lane-Smith 1971). A few warm-cloud electrification mechanisms have been proposed (e.g. Takahashi 1979). He suggested a process based on ion interactions, where growing drops were charged negatively and evaporating drops positively. His observations of Hawaiian warm-clouds and data from his cloud model produced electric fields less than  $200 \text{ V m}^{-1}$ , which are too low to produce lightning discharges. This mechanism would be an example of convective charging, but the short lifetime and shallow vertical structure of warm trade wind clouds prevent strong electric fields from developing.

However, even oceanic cumulonimbus clouds that reach the cold tropical tropopause can still show little or no lightning. The infrequent lightning in oceanic storms may be partly due to the low ice nucleus and cloud nucleus concentrations (Takahashi 1984). He found that the number concentrations of graupel and ice crystals should exceed  $1500 \text{ m}^{-3}$  and  $50 \text{ m}^{-3}$ , respectively, in order to accumulate an electric charge separation large enough to produce lightning. Indeed, Takahashi (1990) found that in the tall, convective clouds in Micronesia, which produced torrential rain but no lightning, the concentration of frozen particles was one order of magnitude less than that required to trigger lightning.

Zipser and Lutz (1994) suggested that the updraft speed of the cloud must exceed a threshold value of  $6\text{-}7 \text{ m s}^{-1}$  to maintain a robust electrification process in the mixed-

phase region. Observational studies have confirmed the relative weakness of the oceanic updrafts (LeMone and Zipser 1980; Zipser and LeMone 1980; Jorgensen and LeMone 1989; Lucas et al. 1994; Petersen et al. 1999; Anderson et al. 2005). In contrast, continental storms have significantly stronger updrafts, which may be partly due to higher Convective Available Potential Energy (CAPE) values over the land. Rutledge et al. (1992) investigated the lightning rates and CAPE during the monsoon season near Darwin, Australia, located on the northern coast. They showed that during low CAPE periods ( $\sim 500 \text{ J kg}^{-1}$ ), lightning was absent or the rates were very low. Lightning rates increased during periods of large CAPE ( $>1500 \text{ J kg}^{-1}$ ). However, CAPE values over the tropical oceans are not insignificant. Zipser and LeMone (1980) documented an average value of  $1500 \text{ J kg}^{-1}$  during the GARP Atlantic Tropical Experiment (GATE), where observed maximum vertical velocities in the top 10% of the storms were only  $\sim 5 \text{ m s}^{-1}$ .

Although CAPE may be substantial over the oceans, its vertical distribution can be significantly different between land and ocean. CAPE is often evenly distributed over a deep layer over the oceans, whereas it is concentrated within a shallow layer over land (e.g. Ebert and Holland 1992). McCaul and Weisman (2001) found in their numerical simulation that the stratification of the buoyancy had great effect on the vertical velocity. When CAPE was concentrated in the low-levels, the parcel vertical velocity was greatly enhanced. Thus, CAPE is an overly simplified measure of convective potential (Blanchard 1998).

Although the lightning climatology shows reduced number of flashes over the ocean when compared with rates over adjacent continents, LIS and OTD have observed a

winter maximum over the North Pacific (e.g. Christian et al. 2003). PacNet data has also documented significant electrical activity over the North Pacific in a number of passing midlatitude cyclones. Williams et al. (2000) and Boccippio et al. (2000) used Tropical Rainfall Measurement Mission's (TRMM) Lightning Imaging Sensor (LIS) data to demonstrate that the majority of the differences between land and ocean lightning rates can be accounted for by differences in storm density and frequency of occurrence, rather than differences in storm instantaneous lightning rates. This result suggests that the conditions for cloud electrification are less frequently met over the oceans than over the land, but once the conditions are met, the cloud electrification mechanism is similar in maritime and continental storms. Petersen et al. (2005) presented a similar argument that *the environment can influence the degree to which the physical requirements for charge separation are met, but once the requirements are met, the basic physical process of charge separation is the same regardless of the regime (land, ocean or coast)*. Therefore, they hypothesized that the relationship between precipitation ice water path (IWP) and lightning rate should be nearly regime invariant, which was verified in the consistent correlation found globally between IWP and lightning flash density. Sherwood et al. (2006) show that the global climatological maximum in lightning rates is linked to small effective diameter of ice crystals near cumulonimbus cloud tops. This relationship was consistent both in continental and maritime environment.

### *3.1.2 Lightning vs. rainfall*

The relationship between lightning and convective rainfall has been shown to vary

up to three orders of magnitude, depending on air-mass characteristics and cloud microphysics (e.g. Petersen and Rutledge 1998). However, several studies suggest that over a particular climatic regime and a limited geographic region, lightning is well correlated to convective rainfall (Cheze and Sauvageot 1997; Petersen and Rutledge 1998; Tapia et al. 1998; Soriano et al. 2001).

In this study, we used PacNet lightning rates corrected for network detection efficiency (DE) and TRMM satellite data matched in space and time to study the relationships between oceanic lightning, precipitation, and hydrometeor characteristics.

### **3.2. Data and methods**

#### *3.2.1. PacNet/LLDN data*

The domain of this study is centered over Hawaii (0-40°N; 140-180°W) (Fig. 1.2). Currently PacNet consists of four long-range VLF sensors installed on the islands of Kauai and Big Island (Hawaii), Unalaska (Alaska) and Kwajalein (Marshall Islands). Data from LLDN (Long-range lightning detection network) are included in the data processing. LLDN sensors are conventional broadband LF/VLF sensors installed in the U.S. and Canada, but make a valuable contribution to the network, especially over the eastern Pacific. A detailed description of PacNet is given in Chapter 2.

The fourth PacNet sensor was installed in Kona, Hawaii in February 2004. Therefore three years of data (February 2004 – February 2007) were used in this study. The detection efficiency (DE) of the PacNet varies both spatially and temporally, because

of the geometry of the sensor sites and the diurnal variation of the reflectivity of the ionosphere. A DE model (Chapter 2) was applied to the lightning data stream to take this variability into account, and adjust the lightning rates (Fig. 2.14). The finite location accuracy of PacNet (Section 2.5.2) was taken into account by smoothing the lightning density field so that the lightning density in each grid cell accounted for 70%, and the 8 grid cells surrounding the cell accounted for the remaining 30% of total lightning density in each cell.

The PacNet lightning data used in this study were quality controlled as follows. (a) Only the days when at least three PacNet sensors (Kauai, Kona, Unalaska + LLDN) were up, were included in the analysis. (b) Multiple locations were removed from the database (Section 2.5). A single lightning strike is often detected as two or more PacNet events. Multiple sky-wave locations are possible, because more than one "collection" of sensors can experience a group-consistent propagation path delay. In contrast, there is only one (or zero) ground-wave location. Error statistics were used to select between multiple PacNet locations. The error-ellipse semi-major axis (SMA) and angle and time deviations ( $\chi$ ) are associated with each flash and represent the quality of the location. If there were multiple locations within 1 ms, the flash with the smallest value of  $\frac{SMA}{\sqrt{\chi}}$ , ( $\chi \geq 1$ ) was chosen to represent the flash location. (c) Only the area, where the projected location accuracy of PacNet was better than ~15 km was included in the analysis (Fig. 2.15). Data were also excluded in the areas where the modeled DE was < 3% (in the immediate vicinity of the Hawaiian sensors where DE approaches zero due to the network geometry

and in remote corners of the domain, Figure 2.14). PacNet data quality control results in slightly reduced data set over the three-year period. Data from storms missing from the PacNet dataset may be present in LIS database, resulting in a slightly different set of storms included in the two databases. Given the climatological nature of the study, this difference in the databases is justifiable, as will be discussed in Section 3.3.

### *3.2.2. TRMM data*

All the TRMM orbits, when LIS detected any lightning over the central Pacific, were included in the analysis (over 2000 overpasses). Since the orbital inclination of the TRMM satellite is  $35^\circ$ , TRMM data are available within the latitude band from  $\sim 38^\circ\text{N}$  to  $38^\circ\text{S}$ , depending on the swath width of the instrument (e.g. Kummerow et al. 1998). Precipitation radar (PR) 2A25 (version 6) products are used in this study, including estimated surface rainfall, precipitation water path and vertical profiles of radar reflectivity (Iguchi et al. 2000). PR measures the reflectivity at 80 range bins from surface to 20 km altitude with 250 m vertical resolution. The horizontal sampling resolution is 4.3 km.

The 2A25 PR pixels identified as “convective” (as in 2A23 Rain Type Flag), were used in this study. The only exception to this is the result presented in Section 3.3.3, where estimated surface rainfall rates from pixels identified as “stratiform” are shown and compared to convective rain rates. The rainfall rates used in this study are the 2A25

estimated surface rain rates. These are calculated by assuming a constant slope of dBZ<sub>e</sub> from the bottom of the clutter-free rain echo.

In addition, 2A12 version 6 products are used, including vertical profiles of latent heating and precipitable ice in 14 layers with 5 km horizontal resolution. Below 4 km the vertical resolution is 0.5 km and the resolution decreases upward to 4 km in the highest layer, 14-18 km above the surface.

The TMI measures the intensity of radiation at five separate frequencies; 10.7, 19.4, 21.3, 37.0, and 85.5 GHz. The 2A12 algorithm searches a large database of cloud resolving model (CRM) simulations to find cloud profiles that are radiatively consistent with TMI radiance measurements. The retrieved profile is a composite of those consistent profiles (Kummerow et al. 2001). Some 2A12 products, such as cloud ice data, should be interpreted cautiously, since small ice particles do not have microwave signature, and the vertical cloud ice profiles are solely products of the cloud resolving models. In version 6 of 2A12, a significant improvement of the Bayesian estimation method was implemented. *The revised algorithm is supported by an expanded and physically more consistent database of cloud model simulations.* The CRM simulation database now includes both Goddard Cumulus Ensemble (GCE) and the fifth-generation Pennsylvania State University-National Center for Atmospheric Research Mesoscale Model (MM5) simulations of a tropical cyclone, tropical squall lines over the Pacific and Atlantic, tropical convection over the Pacific and two extratropical cyclones in the North Atlantic. One of the simulated Atlantic extratropical cyclones occurred in the summer and one in the winter. Both warm and cold frontal regions of the cyclones were

simulated. In addition, several other modifications were included to allow better estimates of the storm properties, with a specific goal to obtain improved estimates of the latent heating profiles over the ocean surfaces. The algorithm is described in detail in Olson et al. (2006) and Yang et al. (2006). This was the first attempt to include latent heating estimations within the framework of 2A12. An improved algorithm under development, which utilizes the same Bayesian framework as 2A12, but with a training database derived from PR observations, is described in Grecu and Olson (2006).

TRMM also carries LIS, which contains an optical staring imager that detects brightness changes in the clouds as they are illuminated by lightning discharges (Christian et al. 1992). LIS can detect cloud-to-ground, cloud-to-cloud, and intracloud lightning. LIS views a 600 km x 600 km area with a spatial resolution of 4 km at nadir and 7 km at limb. One downside of LIS is that it observes every point within its field of view for only ~90 seconds, which makes weak oceanic storms with lightning rates less than ~1 flash per minute undetectable by LIS (Boccippio et al. 2000). Lightning rates are corrected for diurnally varying LIS detection efficiency using the DE values of 73% (93%) for day (night) estimated by Boccippio et al. (2002).

### *3.2.3. Methods*

TRMM derived products were averaged over  $0.5^\circ$  latitude x  $0.5^\circ$  longitude grid cells. Lightning strikes from PacNet that occurred  $\pm 15$  minutes of the satellite overpass time over the same grid cells were counted. Both LIS and PacNet lightning counts were normalized as flashes per  $10^4$  km<sup>2</sup> per hour. The size of a  $0.5^\circ$  grid cell is a function of

latitude and was taken into account in the normalization. LIS observation time of 90 s was used for normalization.

The observations show a logarithmic decrease in observation count with increasing lightning rate (Fig. 3.3). The logarithmic fit for the cumulative probability distribution function (PDF) of the data suggests dividing the lightning data into bins using a logarithmic division, e.g. values between  $2^n$  and  $2^{n+1}$  flashes  $\times (10^4 \text{ km}^2 \text{ h}^{-1})^{-1}$  formed a bin ( $n=\text{integer}$ ). Using this method, the bins plotted on a logarithmic axis are nearly equidistant. Because of low number of samples in the highest bin, the two highest bins were combined for both winter and summer data.

Lightning flashes detected by PacNet are mostly cloud-to-ground, whereas LIS detects both cloud-to-ground (CG) and intra-cloud (IC) flashes (Chapter 2). LIS flash rates are not corrected for IC:CG ratio in this study, as the ratio varies with storm type and stage, environmental conditions, and domain (Pierce 1970; Prentice and Mackerras 1977; Mackerras et al. 1998; Boccippio et al. 2001; Chapter 2 in this study). The impact of this on the results is discussed in Section 3.3.2.

### **3.3. Results**

Three years of active lightning days were analyzed over the central North Pacific Ocean during 2004-2007. Most of the summer storms were associated with upper-tropospheric disturbances during July-August (e.g., Fig. 3.4), when a Tropical Upper Tropospheric Trough (TUTT) is most pronounced over the central Pacific (Sadler 1975; Kelley and Mock 1982). Typically during these storms, an upper-level low-pressure

center (TUTT cell), with a well-defined circulation, and cold temperatures aloft were evident in the upper-level charts (Fig. 3.4b). Surface maps showed little sign of a surface trough during the weakest storms, but a surface trough was associated with the stronger storms (Fig. 3.4c).

During the winter, most of the lightning activity was associated with extratropical storms and Kona lows (Morrison and Businger 2001; Otkin and Martin 2004; Caruso and Businger 2006), and in particular with convection along cold fronts or well defined troughs at the surface and aloft (Fig. 3.5). Although most of the storm centers stay north of Hawaii, the cold fronts and associated cold upper-level troughs often reach the islands and cause the majority of the annual lightning and severe weather events locally in Hawaii (e.g., Businger et al. 1998).

The 2A12 version 6 database, discussed in Section 3.2.2, includes both extratropical winter frontal systems and summer convective systems. Therefore, it is expected that 2A12 adequately represents both the winter and summer storms. However, since 2A12 is still under development (specifically the latent heating algorithm), the results from 2A12 should be interpreted as preliminary.

### *3.3.1. Vertical profiles of radar reflectivity and rainfall.*

Vertical profiles of radar reflectivity have been found to be an important indicator of cloud electrification and lightning activity (e.g. Zipser and Lutz 1994; Petersen et al. 1996; Toracinta et al. 1996, 2002; Nesbitt et al. 2000). Several studies have shown that the main thunderstorm charging mechanism is the ice-ice collision process, where the

riming graupel particles collide with smaller ice particles in the presence of supercooled water (e.g. Saunders 1993). This process occurs in the mixed-phase region, from 0°C to -20°C, and is the most efficient from -10°C to -20°C. Radar reflectivity can be used to estimate the amount of mass present in the mixed phase region, which is an important indicator of the robustness of the charging process. The suggested vertical velocity threshold of 6-7 m s<sup>-1</sup> (Zipser and Lutz 1994) can support raindrops in the 1.2 to 1.5 mm range at -10°C (e.g. Foote and Toit 1969), and therefore provide adequate hydrometeor source for electrification.

Figure 3.6 shows that radar reflectivity increases with lightning rate throughout the troposphere. Table 1 summarizes the values found for several altitude (or temperature) and reflectivity thresholds. The average freezing levels given in 2A25 data for winter and summer storms are 3.7 and 4.0 km, respectively. When an average temperature lapse rate of -6.5°C km<sup>-1</sup> is applied, the levels of -10°C and -20°C are ~1.5 km and ~3 km above the freezing level, respectively.

Earlier studies have shown that the decrease in radar reflectivity with height in the mixed phase region is much greater for oceanic than continental thunderstorms. Estimates of the lapse rate for oceanic regime vary between 6.0 and 6.5 dBZ km<sup>-1</sup> (Jorgensen and LeMone 1989; Szoke et al. 1986; Zipser and Lutz 1994). In sharp contrast, continental storms show much lower lapse rates, between 1.3 and 2.0 dBZ km<sup>-1</sup> (Donaldson 1961; Zipser and Lutz 1994). In this study, the lapse rate varied between 5.3 and 3.0 dBZ km<sup>-1</sup> for low lightning rate winter storms and for high lightning rate storms, respectively.

### 3.3.2. Maximum radar reflectivity and altitude of the echo top

Maximum attenuation corrected radar reflectivity is a separate 2A25 product given for each radar beam and should not be confused with lowest-level Z in Figure 3.6. However, the maximum reflectivity is often observed at the lowest levels, making the difference relatively small. Maximum Z increases with lightning rate from 33 to 41 dBZ in the winter and from 32 to 40 dBZ in summer (Fig. 3.7a). The variance decreases with increasing lightning rate.

The echo top altitude increases with lightning rate from ~6.7 km to 12.8 km in the winter, and from 7.0 to 13.5 km during the summer (Fig. 3.7b). As in Figure 3.7a, variance decreases with increasing lightning rate. Coefficients of determination ( $R^2$ ) in both Figures 3.7a and b are between 0.95 and 0.98. Futyán and DelGenio (2007b) investigated the height of the convective storms over African/Atlantic region and also found a strong correlation between the PR echo top altitude and LIS flash rates. It should be noted that the echo top detected by TRMM's PR is not equivalent to cloud top height because of PR's limited sensitivity (~17 dBZ).

Although a direct comparison of reflectivity (Fig. 3.7a) to rainfall rates seems appealing (Fig. 3.8a), the corresponding rain rates cannot be readily determined from the composite radar image, as the Z-R relationship used by 2A25 varies. Parameters a and b in the relationship  $R=aZ^b$  used by 2A25 are both functions of the rain type, the heights of the 0°C isotherm and storm top. Furthermore, the presence or absence of a bright band,

the phase state, the temperature, and the difference in terminal velocity from changes in the air density have effect on parameters a and b (Iguchi et al. 2000).

Lightning rates are generally higher in LIS than in PacNet data set (Fig. 3.7). This is partly because of LIS's intracloud observations and partly because of LIS's view time and limited ability to observe weak oceanic storms. The impact of applying an IC:CG correction to LIS data would be to shift the LIS data points to the left in Figure 3.7 (and other figures with lightning rate as an abscissa) according to IC:CG ratio. However, if the results derived from LIS observations in this study are applied in the future LIS observations, no IC:CG correction is needed, as the same bias exists in both data sets. A similar argument applies for PacNet data. The detection threshold for LIS is ~1 flash per minute (Boccippio et al. 2000). If LIS detects one flash during an overpass over a  $0.5^\circ$  grid cell, the area-normalized minimum flash rate is  $\sim 150 \text{ flashes} \times (10^4 \text{ km}^2 \text{ h}^{-1})^{-1}$  (at  $20^\circ\text{N}$ , using night-time DE of 0.93, and 90 s view time). This value is at the high end of PacNet observations (Fig. 3.7). In addition, some very active thunderstorms occurred near the dateline, which were included in the LIS analysis but were filtered from PacNet analysis because of PacNet's limited location accuracy over that area (Section 3.2.1). The highest non-quality controlled PacNet lightning rates over this area were  $\sim 3700$  and  $940 \text{ flashes} \times (10^4 \text{ km}^2 \text{ h}^{-1})^{-1}$  for winter and summer, respectively. These values are closer to mid- and high end of the LIS flash rates.

### *3.3.3. Lightning vs. rainfall*

The lightning rates from both PacNet and LIS were compared to estimated surface rain from 2A25 convective pixels, as described in Section 3.2. Convective rainfall rate increases with lightning rate during both summer and winter (Fig. 3.8a). This result is not surprising, given that radar reflectivity increases with lightning rate. Winter rainfall rates were generally 1-2 mm h<sup>-1</sup> higher than in the summer. While the values of R<sup>2</sup> of the fitted curves were high (0.92 and 0.96 for winter and summer, respectively), the variance in each bin was relatively large. The standard deviation varied between 3.3 and 5.2 mm h<sup>-1</sup>. The large variance maybe partly due to a varying fraction of warm rain of the total convective rain.

In contrast, the stratiform rainfall was poorly correlated with lightning rate (Fig. 3.8b). Stratiform rain rates remained nearly constant at ~2 mm h<sup>-1</sup> despite of lightning rate or season.

Despite the relatively good correlation between lightning and convective rainfall rates, it should be noted that a large fraction of oceanic rain comes from warm clouds that show no lightning. Such convective systems are naturally not included in this study, as only storms with some lightning activity are incorporated in the analysis.

### *3.3.4. Latent heating*

Vertical latent heating profiles are 2A12 products that combine both convective and stratiform profiles. The low lightning rate curves show a double-peak shape (Fig. 3.9).

This may be due to the shape of the stratiform profile, often characterized by evaporative cooling at 2-3 km altitude (as illustrated in Olson et al. 2006). This feature disappears in the high lightning rate storms, where the convective-shape curve presumably dominates over stratiform, as shown in Figure 3.9. Both winter and summer data show evaporative cooling near the surface (Figs. 3.9a and b).

Although the maximum latent heating at 2-3 km level consistently increases with increasing lightning rate, winter data shows an odd feature. The latent heating rate in the highest category decreases rapidly with altitude above 2 km and reaches the same value at ~4 km as the lowest category. Sensitivity tests performed using different samples of high-lightning rate data did not change the result; highest lightning rate storms have less latent heating above ~3 km than moderate lightning rate storms. The reason for this may be an insufficient 2A12 database or uncertainties in the latent heating algorithm, or a feature in the storm dynamics.

Maximum latent heating rates were obtained by taking the highest latent heating values occurring at any TMI level (Fig. 3.9c). The level of maximum latent heating is usually at 2-3 km altitude and does not change significantly with lightning rate, although a little lift is observed during the summer. The maximum latent heating increases with lightning rate, consistent with Figures 3.9a and b. Although the  $R^2$  values are high (0.94), variance is very large. Again, this may be because of the uncertainties in TMI measurements and latent heating algorithm, or because of complex storm dynamics.

### 3.3.5. Vertical profiles of precipitable ice

Precipitable ice content increases with lightning rate both in winter and summer. As discussed in Section 3.3.1, the presence of ice in the mixed-phase region is instrumental for cloud electrification. The level of maximum precipitable ice shifts upward from winter to summer, whereas the content decreases (Fig. 3.10). The peak precipitable ice content is observed just above the freezing level for both winter and summer (3.5-5.0 km and 4.0-6.0 km, respectively). The profile for the highest lightning category in winter has a greater peak ice content than the moderate category (~4 km), but has a lower content above 5 km. A similar feature was observed in the latent heating profiles (Fig. 3.9a). Interestingly, the altitude of the peak ice content during the winter decreases with increasing lightning categories (from ~5 to ~3.5 km), although this difference is ~ one TMI level (Fig. 3.10a). In the summer, the level of the peak ice content is nearly the same for each lightning category (Fig. 3.10b). Given the limited 2A12 winter database and uncertainties in the algorithm, these subtle differences in altitude should be interpreted with caution.

Del Genio and Kovari (2002) used TMI and LIS data and categorized data into tropical oceanic lightning and non-lightning, and land lightning and non-lightning storms. They constructed profiles of precipitable ice content and found maximum precipitable ice content of  $320 \text{ mg m}^{-3}$  in oceanic storms both with and without lightning. In this study, the maximum content varied between 100 and  $600 \text{ mg m}^{-3}$  for low and high lightning rate storms, respectively (Fig. 3.10). As this study concentrated only on storms with some lightning activity, the values for comparison to *non-lightning storms are not available*.

### *3.3.6. Precipitation water path and ice water path*

Precipitation water path (PWP) from PR data is the vertically integrated precipitation water content calculated from  $Z_e$  at each range bin, from top of the rain to the surface. Both liquid and solid phase regions are included in the calculation. PWP increases with lightning rate with very little difference between summer and winter (Fig. 3.11a).

Ice water path (IWP) is calculated from 2A12 vertical precipitable ice profiles as observed by TMI. IWP increases with lightning rate with slightly higher values during the winter in the low- and moderate lightning rates (Fig. 3.11b). Although the  $R^2$  values are a little higher in IWP than in PWP data, the variance is significantly lower in PWP data. This may be partly due to the robustness of the PR observations and 2A25 compared to TMI observations and 2A12 algorithm.

## **3.4. Summary, conclusions, and discussion**

The objective of this study is to investigate the correlation between lightning rates and various storm characteristics that are physically connected to lightning production via storm dynamics. These storm properties can then be estimated from lightning rates and assimilated into numerical models in data sparse regions, such as the open oceans.

Long-range lightning data from Pacific Lightning Detection Network (PacNet) and Lightning Imaging Sensor (LIS) were compared with TRMM 2A25 Precipitation Radar

and 2A12 hydrometeor products. The PacNet lightning rates were quantified by applying a detection efficiency (DE) model correction to account for spatial and temporal differences in lightning detection efficiency over the domain.

Three years of lightning-active days during summer and winter were analyzed over the central North Pacific Ocean. The winter storms were mostly extratropical cyclones, with most of the electrical activity associated with cold fronts. The summer cases were mostly convective storms triggered by cold upper-tropospheric disturbances associated with the TUTT. Vertical profiles of radar reflectivity, latent heating, and precipitable ice were constructed.

#### *3.4.1 Conclusions*

The results of the data analysis show a consistent logarithmic increase in convective rainfall rate with increasing lightning rates. Moreover, other storm characteristics, such as radar reflectivity, storm height, IWP, and PWP show a similar type of increase. The probability distribution function for PacNet lightning rate (Fig. 3.3) shows an exponential decrease in occurrence with increasing lightning rates.

Radar reflectivity increased throughout the troposphere with lightning rate. Specifically, the reflectivity in the mixed-phase region increased significantly with lightning rate and the lapse rate of Z decreased; both are well-known indicators of the robustness of the cloud electrification process. In addition, the height of the echo tops showed a strong logarithmic correlation with lightning rate.

A similar slope in the lightning-convective rainfall relationship for both summer- and winter cases indicate that over the central North Pacific, the average lightning-rainfall relationship is relatively independent of the season and storm type. Stratiform rain rate, however, was poorly correlated with lightning and remained nearly constant despite of the lightning rate.

Precipitation water path (PWP) and ice water path (IWP) each showed a logarithmic increase with lightning rate, with nearly similar  $R^2$  values. PWP was similar both in winter and summer, whereas IWP was generally higher during the winter.

#### *3.4.2. Discussion*

Probability distribution function for PacNet lightning rate (Fig. 3.3) shows that the majority of the population is at the low end of the lightning rates. Previous studies have shown similar cumulative distributions for oceanic lightning (Nesbitt et al. 2000; Petersen et al. 2005). The PDF for convective rainfall rate (Fig. 3.3) also shows an emphasis on the low end of the rainfall rates, although the slope of the curve is less steep as with the lightning PDF.

Logarithmic and exponential distributions, such as those found the in analysis presented here, commonly occur in the atmosphere. The number density of the cumulus clouds has been observed to decrease nearly exponentially with increasing cloud size (e.g. Plank 1969). Drop-size distribution is exponential (Marshall and Palmer 1948). Junge et al. (1969) and Bullrich et al. (1966) studied aerosol distribution in Pacific airmasses and found sharp decay in the number of aerosol with aerosol radius. The

distribution was approximated by a power law with an exponent between -3 and -4.

Takahashi (1976), in a numerical study, found a logarithmic increase in rain rate when the number of cloud nuclei was decreased and approached a threshold value of  $\sim 150 \text{ cm}^{-3}$ .

Foster et al. (2003) found an exponential growth of rain rate with precipitable water in Hawaii.

A suggestion is presented here to interpret physically the logarithmic PDFs and logarithmic relationship between lightning and convective rainfall: Assuming some CAPE and low-level moisture convergence over a limited area, a cloud starts to grow and the rainfall production is initiated in the cloud. The number of CCN has a great impact on the precipitation initiation and development (e.g. Takahashi 1976; Göke 2007), but assuming relatively uniform aerosol content over the ocean, the available moisture content determines the maximum potential rainfall rate. Other environmental conditions have weaker impact on the rainfall rate.

In contrast, the requirements for a robust charge-separation process are much more complex. Updraft speed, supercooled liquid water content, and ice content all need to be sufficient at the right altitude within a cloud. Other, yet to be defined, conditions also may play a role. Although weak cloud electrification is fairly common, the highest potential lightning rates are observed only on rare occasions when all the conditions for active lightning are met in a complex convective system.

These environmental circumstances and the results presented here suggest that the estimation of, for instance, rainfall rates from lightning rates is relatively insensitive at high lightning rates and more sensitive at low lightning rates. This is an encouraging

result for lightning data assimilation applications, since the areas of strong storm activity and high rainfall rates, although less common, are the most important for NWP modeling.

Several studies have shown that lightning data can be assimilated into numerical models to help to improve the model forecasts (Alexander et al 1999; Chang et al. 2001; Papadopoulos et al. 2005; Pessi et al. 2006). The lack of in situ data over the Pacific Ocean for initializing numerical models can lead to large forecast errors for storms that impact the west coast of North America or Hawaii. The results of this study suggest that the data from PacNet can be used as a proxy to estimate convective rainfall, latent heating, and hydrometeor profiles from lightning rates over the open ocean.

In the next Chapter, the results presented here are utilized to assimilate PacNet lightning data into a NWP model.

Table 3.1 Summary of heights and reflectivities at various dBZ and altitude thresholds.

Winter (summer)	20 dBZ	30 dBZ	0°C [3.7 (4.0) km]	-10°C [5.2 (5.5) km]	-20°C [6.7 (7.0) km]	Average lapse rate of Z (0°C...-20°C)
Low lightning rate	3.8 (3.7) km	2.2 (N/A) km	21 (19) dBZ	11 (11) dBZ	5 (6) dBZ	5.3 (4.3) dBZ km <sup>-1</sup>
Moderate lightning rate	6.4 (6.5) km	4.2 (3.6) km	31 (28) dBZ	25 (24) dBZ	18 (18) dBZ	4.3 (3.3) dBZ km <sup>-1</sup>
High lightning rate	8.4 (9.2) km	5.3 (5.5) km	35 (36) dBZ	30 (30) dBZ	26 (27) dBZ	3.0 (3.0) dBZ km <sup>-1</sup>

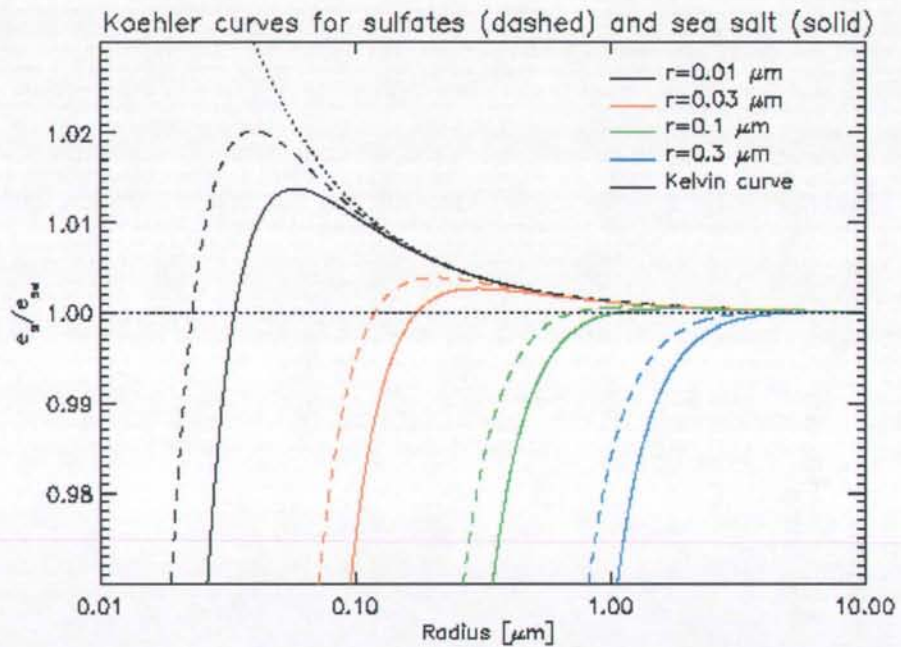


Figure 3.1 Kohler curves for different size sulfates and sea salt. If a cloud condensation nuclei is small and supersaturation is low, particle does not reach the critical size and eventually evaporates. Larger CCN reach their critical size in lower supersaturation values and continue to grow.

### GRAVITATIONAL COLLISION EFFICIENCY

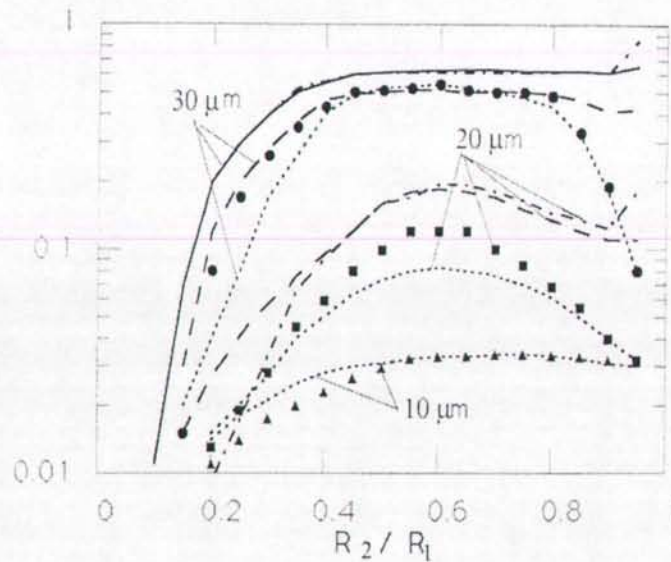


Figure 3.2 Collision efficiencies vs ratio of colliding drop radii. Triangles ( $10 \mu\text{m}$  radius drop collector), squares ( $20 \mu\text{m}$  radius drop collector) and circles ( $30 \mu\text{m}$  radius drop collector) (Pinsky et al, 1999). The theoretical results obtained in different studies (Pruppacher and Klett 1978) are also presented; dotted lines, Jonas (1972); dashed lines, Klett and Davis (1973); dashed-dotted lines, Lin and Lee (1975); solid line, Schlamp et al. (1976).

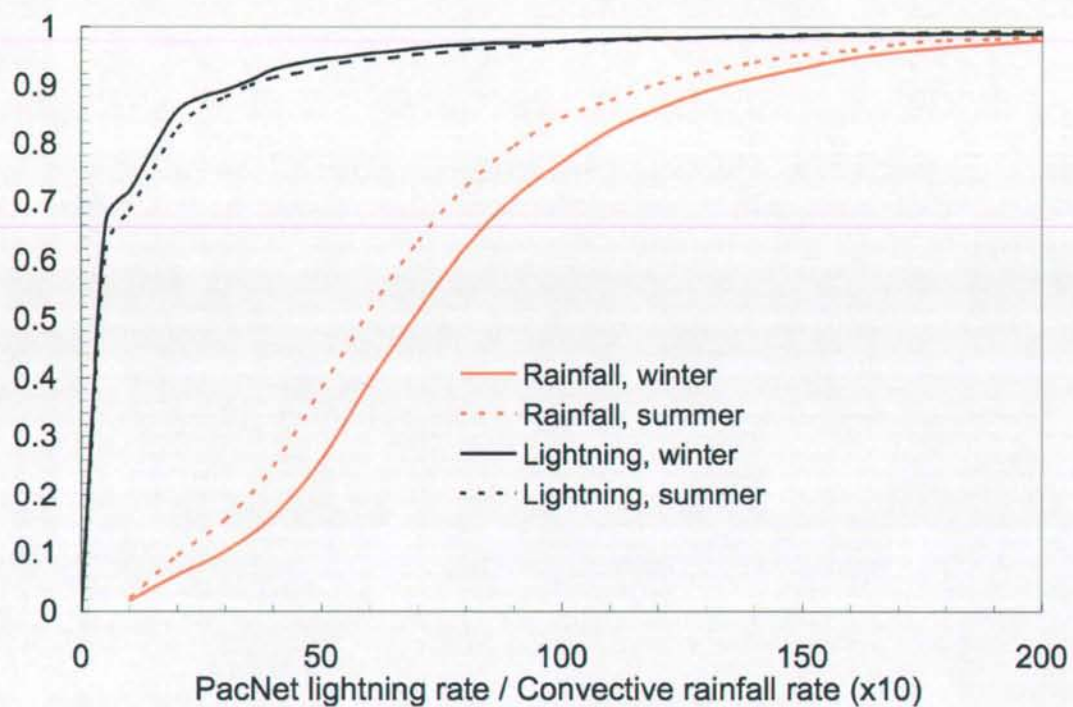


Figure 3.3 Cumulative probability distribution function for PacNet lightning rate [flashes  $\times (10^4 \text{ km}^2 \text{ h}^{-1})^{-1}$ ] and PR convective rainfall rate [ $\text{mm h}^{-1} \times 10$ ]. The x-axis is suppressed with  $\sim 99\%$  of the highest rates shown.

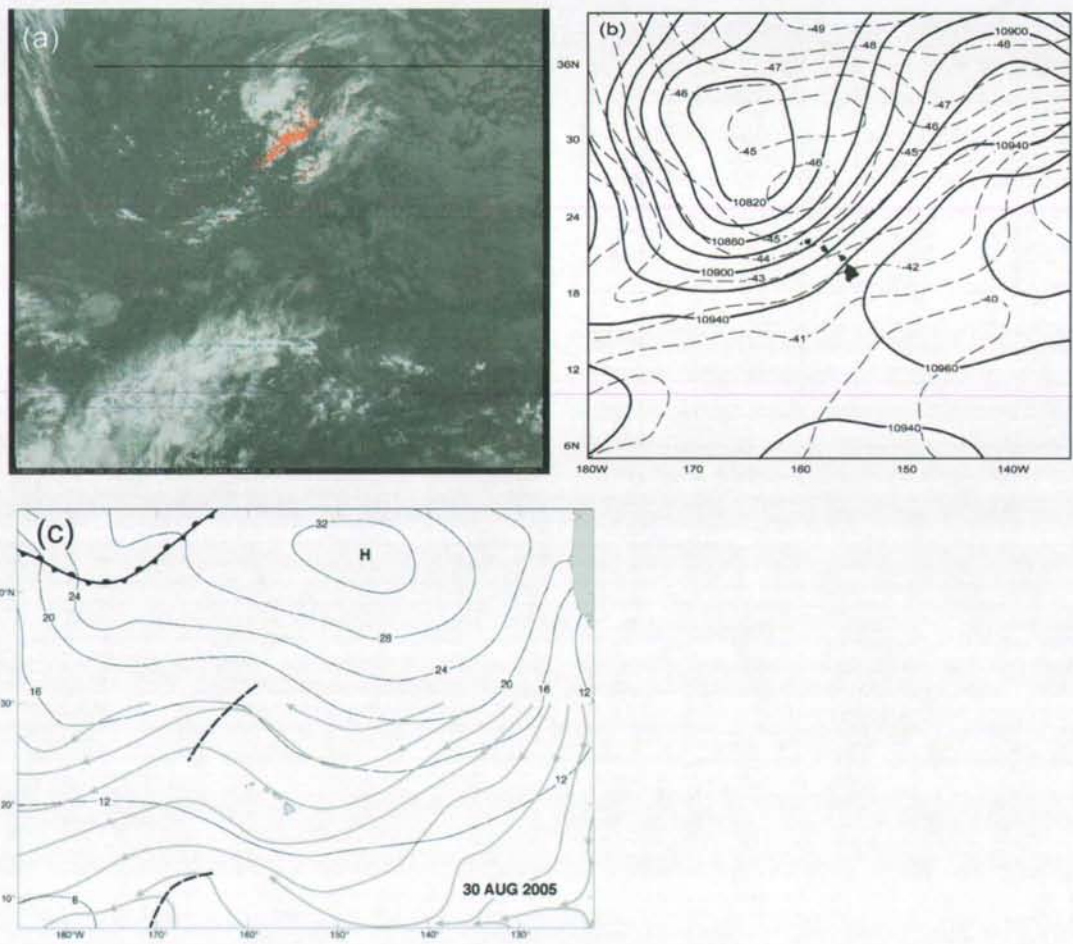


Figure 3.4 (a) GOES-10 infrared image at 1130 UTC on 30 August 2005 overlaid with one-hour of PacNet lightning observations. (b) NCEP Reanalysis at 1200 UTC on 30 August 2005 at 250 hPa shows a low northwest of Hawaii. (c) NWS subjective surface analysis of the central Pacific at 1200 UTC on 30 August 2005 shows a surface trough northwest of Hawaii. Streamlines are plotted in gray south of 30°N.

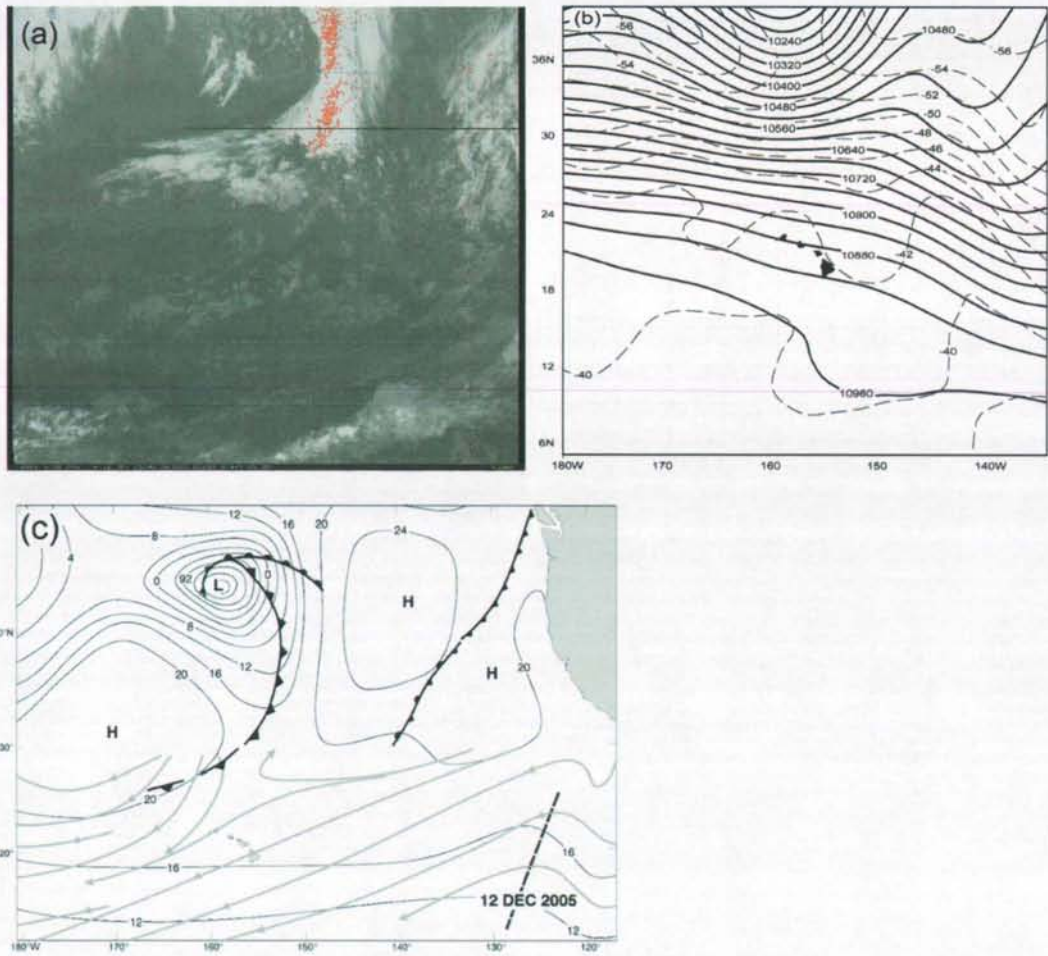


Figure 3.5 As in Figure 3.4 but for 0600 UTC on 12 December 2005. Satellite image in (a) is valid at 0630 UTC.

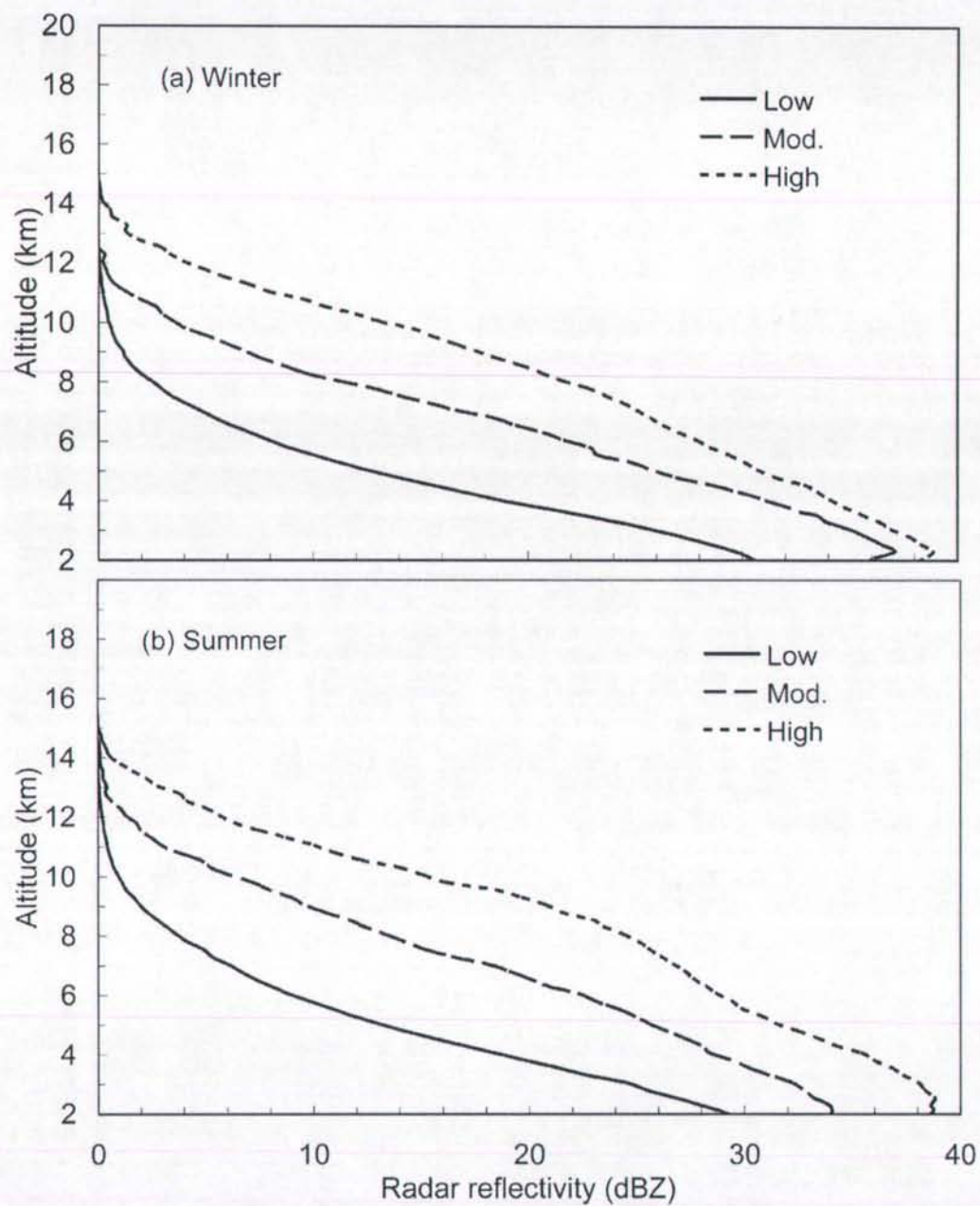


Figure 3.6 Vertical profiles of PR reflectivity in (a) winter and (b) summer for three different lightning rate categories (low, moderate, and high lightning rate). Low lightning rate category is the lowest bin from PacNet data, moderate category is the highest PacNet data bin, and high category the highest LIS bin, as described in Section 3.2.3. Lowest levels are not shown since the near-surface range bins were frequently filled with surface clutter, or missing data. Despite a sensitivity threshold for PR echos of  $\sim 17$  dBZ, values start from zero because of the compositing method.

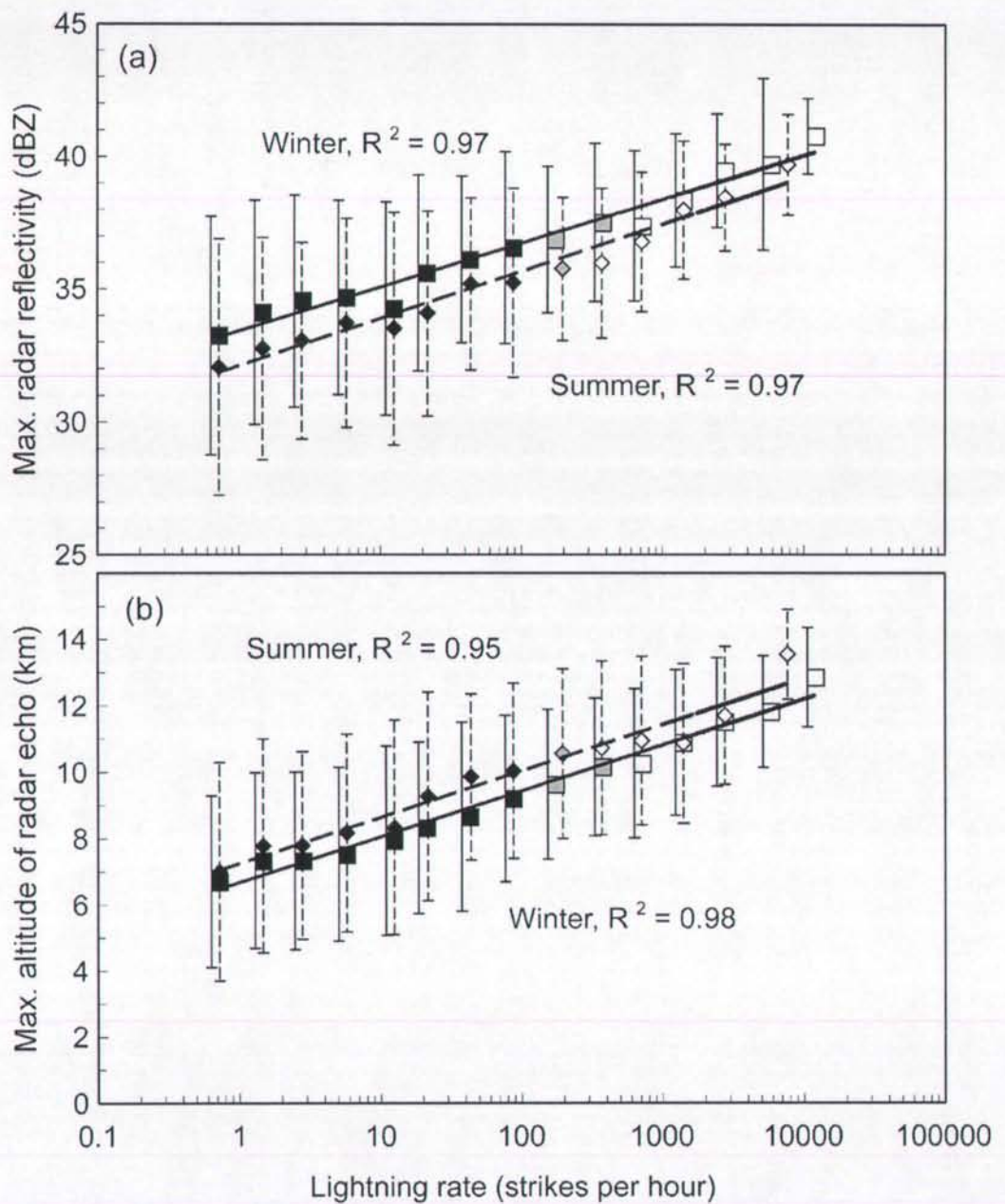


Figure 3.7 (a) Maximum PR reflectivity and (b) maximum height of radar echo. Squares and solid lines are for winter data and diamonds and dashed lines for summer data. Filled symbols are PacNet data, open symbols are LIS data, and grey symbols are combined PacNet and LIS data. Abscissa shows the number of lightning flashes per hour normalized over  $10^4 \text{ km}^2$ . The error bars are  $\pm 1 \sigma$ .

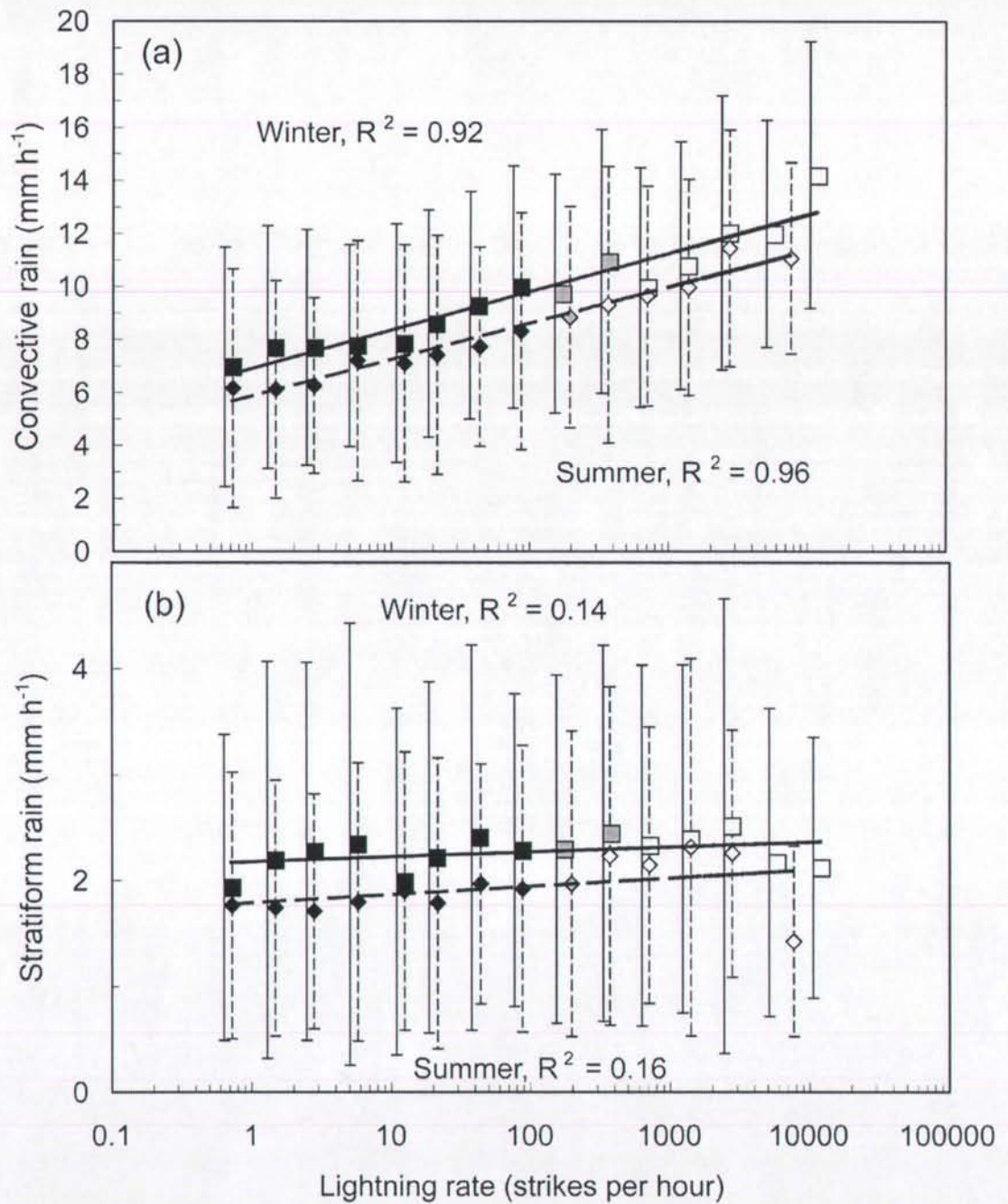


Figure 3.8 (a) Convective rainfall vs. lightning rate and (b) stratiform rainfall vs. lightning rate. Symbols and lines as in Figure 3.7.

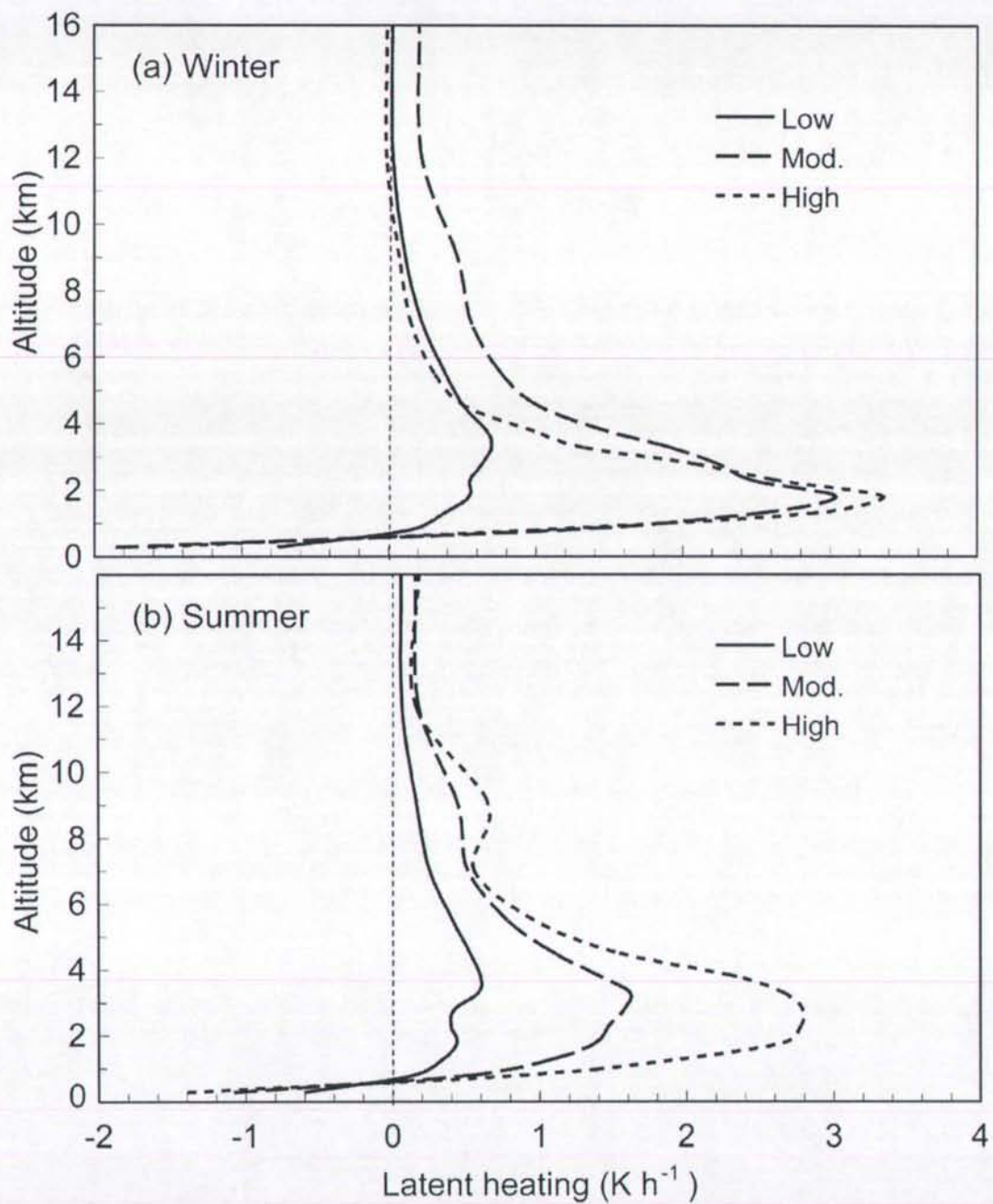


Figure 3.9 As in Figure 3.6, but vertical profiles of latent heating in (a) winter and (b) summer for low, moderate and high lightning rates. Lines and symbols as in Figures 3.6 and 3.7.

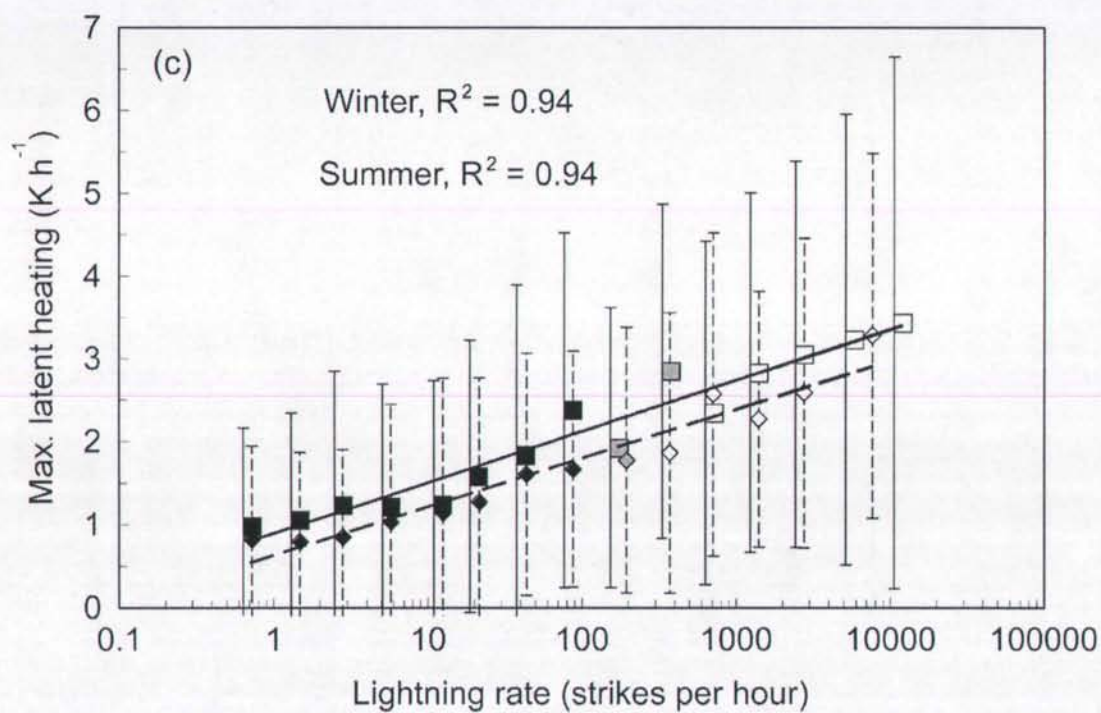


Figure 3.9 continued. (c) Maximum latent heating rate vs. lightning rate. Lines and symbols as in Figures 3.6 and 3.7.

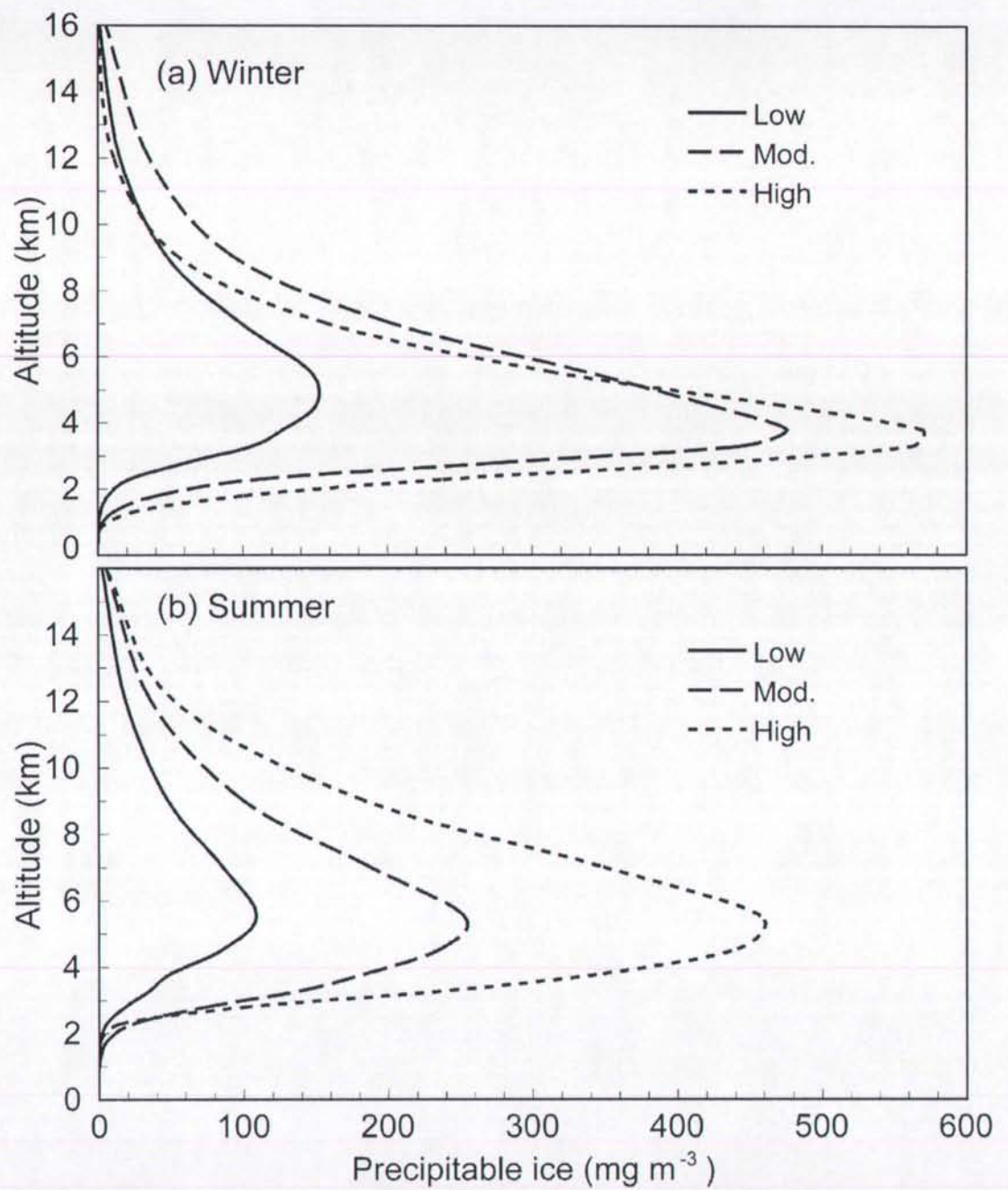


Figure 3.10 As in Figure 3.6, but precipitable ice content, derived from TMI data, as a function of height and lightning rate.

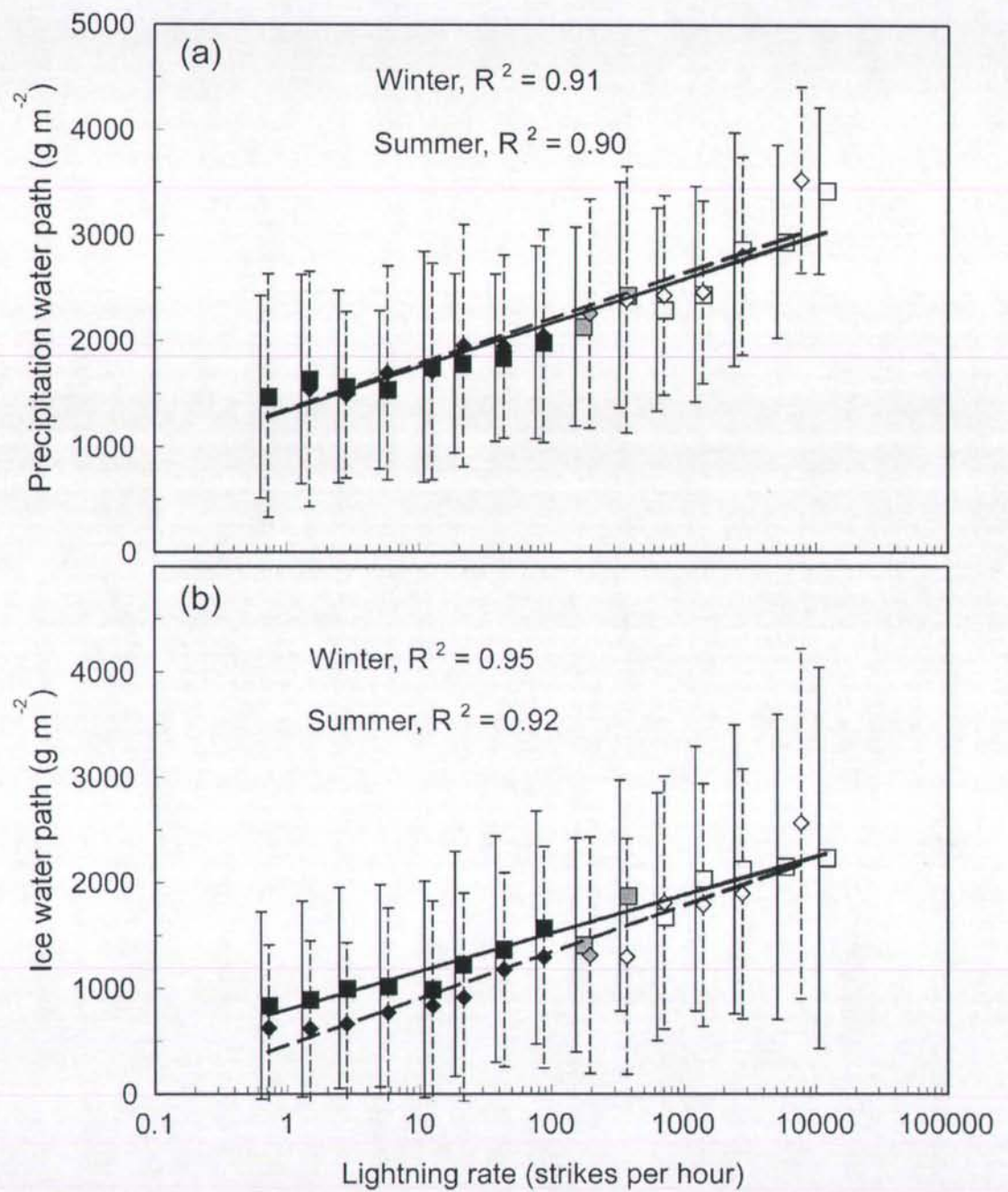


Figure 3.11 (a) Precipitation water path derived from PR and (b) ice water path derived from TMI. Lines and symbols as in Figure 3.7.

# CHAPTER 4. THE IMPACT OF LIGHTNING DATA ASSIMILATION ON TWO WINTER STORM SIMULATIONS OVER THE NORTH PACIFIC OCEAN<sup>4</sup>

## 4.1 Introduction

Diabatic heating sources, especially latent heat release in deep convective clouds, can play an important role in storm development and dynamics (e.g. Anthes et al. 1983; Brennan and Lackmann 2005). Lack of observations over the Pacific Ocean can lead to inadequate initial conditions in the moisture and vertical motion fields of the NWP models, and result in well-documented spin-up problem (e.g. Davidson and Puri 1992). This can subsequently result in large errors in storm central pressure and rainfall forecasts (e.g., McMurdie and Mass 2004). Specifying diabatic heating sources or moisture distribution in the early hours of a forecast can improve the model's performance (Bauman et al. 1997; Businger et al. 2005).

Manobianco et al. (1994) assimilated satellite-derived precipitation into a regional-scale numerical model. The assimilation was implemented by scaling the model generated profiles of latent heating according to rainfall rates derived from satellite observations. At grid points where the model was not producing precipitation, the

---

<sup>4</sup> Pessi, A. and S. Businger, 2008: The Impact of Lightning Data Assimilation on two Winter Storm Simulations over the North Pacific Ocean. Manuscript to be submitted to *Monthly Weather Review*.

vertical distribution of latent heating was specified using model-generated profiles at adjacent grid points with similar rainfall rates as estimated from satellite observations.

Alternatively, observed rainfall rates can be assimilated by “inverting” or “reversing” the precipitation parameterization. The scheme adjusts the moisture (and to some extent the temperature) profiles so that the CPS reproduces the observed rainfall rate. This type of scheme has been used to initialize the model in order to reduce the spin-up time (e.g. Donner 1988; Puri and Miller 1990).

Jones and Macpherson (1997a) used latent heat nudging to assimilate surface rain rate estimates derived from radar data to United Kingdom Meteorological Office (UKMO) Mesoscale Model. The model generated profiles of latent heating were scaled by the ratio of observed and model precipitation rates. The scheme increased the forecast skill for precipitation distribution in the first six to nine hours of the forecast.

Several other studies have shown skill using the nudging method, where rain rates from various sources were assimilated into NWP models to improve forecasts of various storm systems – including tropical convection and tropical cyclones, (e.g. Karyampudi et al. 1998; Davolio and Buzzi 2004).

Jones and Macpherson (1997b) assimilated long-range lightning data from the UKMO Arrival Time Difference (ATD) network into a limited area model. They did not see any consistent improvement in forecast skill, and suggested that this may have been due to the uncertainties in both the detection efficiency of the ATD network and the lightning-rainfall relationship.

Alexander et al. (1999) investigated the impact of assimilation of precipitation data from various sources on 1993 Superstorm. They used lightning data from the National Lightning Detection Network (NLDN) and UKMO VLF networks, and rainfall data from Special Sensor Microwave/Imager (SSM/I) and Geostationary Operational Environmental Satellite-Infrared (GOES-IR). They derived a lightning-rainfall relationship using the available SSM/I and lightning data over the storm. They found that the assimilation of satellite derived rainfall rates alone was not sufficient to reproduce in observed development of the storm; the cyclogenesis occurred at a time inconveniently placed in between SSM/I overpasses, and GOES-IR imagery only responded to the convection six hours after it actually occurred, when tall clouds and cirrus anvils had formed. However, the addition of continuous lightning data assimilation (LDA) resulted in dramatic improvement of the model prediction.

Chang et al. (2001) used sferics observations from a VLF lightning detection network and rainfall data from Tropical Rainfall Measuring Mission (TRMM) satellite to derive the relationship between convective rainfall and lightning on 1998 Groundhog Day Storm. Assimilation of latent-heating profiles derived from the lightning data along with SSM/I and TRMM precipitation- and integrated water vapor data resulted in improved short-term (9-18h) forecasts.

Papadopoulos et al. (2005) assimilated lightning data from a long-range ZEUS network operating in Europe. They nudged model-generated moisture profiles to empirical profiles according to lightning intensity. The empirical humidity profiles were produced from atmospheric soundings during thunderstorm days. The assimilation

method improved significantly convective rainfall prediction during the assimilation period and maintained the improvement in short-term forecasts up to 12 h.

Mansell et al. (2007) used lightning data from NLDN and Lightning Mapping Array in the U.S. midwest. They used another approach and added water vapor to the boundary layer in lightning active areas. Water vapor was added in small increments up to  $1 \text{ g kg}^{-1}$  until cloud depth reached 7 km and vertical velocity  $10 \text{ m s}^{-1}$ . Thus the convection parameterization scheme was forced to produce convection in the lightning active areas. Conversely, the convection parameterization scheme (CPS) can be prevented from producing vigorous convection where lightning is not observed using several options. The updraft width can be reduced, increasing the entrainment and dilution of updraft air or by limiting the vertical velocity given to parcels and thus making it harder to reach the LFC. Another option is to skip the CPS altogether in that column.

Earlier studies have found that assimilating latent heating in the correct location is more important than accurate estimation of the precipitation intensity (Manobianco et al. 1994; Chang et al. 2001). These results are encouraging for lightning data assimilation, as they may relax the requirements of quantifying lightning rates and deriving lightning-rainfall relationships.

It should be noted that the storms incorporated in this study were very lightning active. As discussed earlier, many oceanic storms show no lightning due to the efficient warm rain process and other causes which prevent cloud electrification from occurring.

Obviously, lightning location systems cannot detect such storms and lightning data assimilation methods are ineffective.

In this study, data from a long-range Pacific Lightning Detection Network (PacNet) are used to identify the areas and intensities of convective activity and latent heat release in thunderstorms over the Pacific Ocean. For the first time, lightning data from a long-range network, corrected for detection efficiency, are assimilated into a numerical model over the open ocean.

## **4.2 Data and assimilation method**

### *4.2.1 Lightning data*

Lightning data for this study were obtained from Pacific Lightning Detection Network/Long-Range Lightning Detection Network (PacNet/LLDN, hereafter just PacNet), described in Chapter 2. Two lightning active storm cases were analyzed, (i) an extratropical cyclone over the northeast Pacific Ocean on 18-20 December 2002, and (ii) a squall line passage over Hawaii on 28 February 2004.

The lightning rates were corrected for temporal and spatial variation of detection efficiency over the Pacific domain according to flash location and local time at that location, and multiple flashes were removed from the data set, as described in Chapter 2.

The LDA method uses rainfall rates as input to adjust the latent heating rates accordingly, as will be described in the next subsection. Therefore, the lightning rates were converted to rainfall rates using an empirical lightning-convective rainfall

relationship (Fig. 4.1). The relationship was derived by comparing rainfall data from TRMM's Precipitation Radar (PR) and lightning data from PacNet over  $0.5^\circ$  grid cells (Chapter 3). Lightning strikes occurring within 30-minute time window, centered at the satellite overpass time, were counted over the grid cells and compared to average convective rainfall rate derived from TRMM's PR 2A25 data.

The observed lightning rate field was smoothed horizontally in this study using a weighted average method, where the lightning rate at each grid point was the sum of its own value and the values of the eight adjacent gridpoints. The gridpoint value itself had a weight of 0.7, and the remaining weight was distributed among the eight grid cells surrounding it. The same method was used in deriving the lightning-rainfall relationship (Chapter 3). The results shown in Figure 4.1 were adjusted to take into account the smaller model grid size used in this study ( $0.25^\circ$ ), as opposed to grid size that was used deriving the curve ( $0.5^\circ$ ). This was done simply by assuming a uniform lightning density over the grid cell and dividing the lightning rates by four. Finally, the convective rainfall rates derived from lightning observations are written to an assimilation file, covering each gridpoint and timestep during the assimilation period.

#### *4.2.2 Model setup and assimilation method*

The model used in this study is the Fifth-Generation National Center for Atmospheric Research (NCAR) - Penn State Mesoscale Model (MM5), version 3 (Grell et al. 1994). The horizontal resolution of the model is 27 km and it has 39 vertical levels. The model is non-hydrostatic and the time step used was 81 s. A nesting option,

available for the model, was not used to simplify physical interpretation of the results. The Kain-Fritsch (KF) convection parameterization scheme was used (Kain and Fritsch 1993). Boundary conditions were provided by the Global Forecast System (GFS) model and were read every six hours. The spectral GFS model adopts a triangular truncation of 254 waves in horizontal with 64 vertical levels (at the time of the case study forecasts). The corresponding horizontal resolution is  $\sim 55$  km or  $0.5^\circ$ .

Before the model run is started, the MM5 initialization process reads the assimilation file into internal arrays. The assimilation technique was implemented in the KF convective parameterization scheme by modifying the model-generated vertical latent heating profiles. The method scales the model's vertical latent heating profiles at each grid point and model level depending on the ratio between rainfall predicted by the model and rainfall derived from lightning data. The scheme was successfully used by Manobianco et al. (1994) to assimilate satellite-derived rainfall rates into a mesoscale model during a rapidly intensifying extratropical cyclone. Similar type of scheme has been later used by Karyampudi et al. (1998), Alexander et al. (1999) and Chang et al. (2001) to assimilate rainfall rates derived either from satellite or/and lightning data.

The scheme considers three regimes. (i) If both the observed rainfall ( $R_o$ ) (derived from lightning rates) and model predicted rainfall ( $R_m$ ) are greater than zero ( $R_o > 0, R_m > 0$ ), the scaling coefficient  $c = (R_o - R_m)/R_m$ . The adjusted latent heating at each model level  $i$  is  $\Delta T_i = (1+c)\Delta T_i^{mdl}$ . To prevent excessive latent heating values and model instability, the scaling coefficient was limited to three. Scaling is done only if the observed rain rate (derived from lightning rate) is greater than the model produced rain

rate. This approach was taken because it is possible to have significant warm rainfall with low lightning rates (or absence of lightning). Moreover, in areas with observed lightning, the model rainfall was consistently less than that suggested by the lightning-rainfall rate relationship. (ii) If the observed lightning rate was zero ( $R_o = 0$ ), no assimilation was done, as the absence of lightning does not imply the absence of rain. (iii) If the rain rate derived from lightning observations at any grid point was greater than zero, but the model rain rate was zero ( $R_o > 0, R_m = 0$ ), a search algorithm was used. Initially the algorithm searches adjacent model grid points for similar rainfall rates ( $\pm 1 \text{ mm h}^{-1}$ ) as those observed. First, the grid points within 10 grid length radius are searched and further grid points are gradually included in the search until a match is found. If no match is still found, model rain rates within  $\pm 2, 3, 5, 10, 15,$  and  $20 \text{ mm h}^{-1}$  of observed are gradually included in the search. After the match is found, the vertical latent heating profile from the matching grid point is used. Because latent heat is insensitive to changes in temperature, but saturation mixing ratio is strongly a non-linear function of temperature, the moisture profile from the matching grid point is not used, as it can originate from different thermodynamic environment. Instead, the levels where the heating rate is positive are saturated.

Radius of influence values of  $0.125^\circ$  and  $0.25^\circ$  were used for the Hawaii and the northeast Pacific cases, respectively. If a flash is observed within the radius of influence from a grid point, it has impact on that particular grid point.

Currently, in the operational system at the University of Hawaii, the MM5 model run starts ~8 hours after the analysis time (Cherubini et al. 2006). MM5 uses the initial

conditions from GFS model which are delivered ~3.5 hours after the analysis time. After MM5 initial analysis is completed, the time integration begins. Lightning data is disseminated near real time, thus allowing assimilation of data during the initial 7-8 hours of the forecast period. Lightning data were assimilated the first eight hours of the model simulation. This time period was chosen because we wanted to simulate conditions in a real-time operational forecasting system. In other words, the results shown in this study could have been produced operationally, if the assimilation system had been implemented at the time. Several other lightning data assimilation studies have shown the impact of the assimilation in test-bed type simulations that could not be implemented directly in a real-time forecasting system.

### **4.3. Results**

Two oceanic storms were analyzed using the available PacNet data: a poorly forecast mid-latitude cyclone over the northeast Pacific Ocean that approached the west coast of the United States and a squall-line passage over Hawaii.

#### *4.3.1. Extratropical storm on the northeast Pacific*

Beginning on 18 December 2002, an extratropical cyclone started to produce lightning as it moved across the east Pacific Ocean. The surface analysis valid at 0000 UTC on 18 December shows a trough located at 46°N and 146°W with surface pressure of 994 hPa (Fig. 4.2a). This is approximately 1700 km west of the U.S. west coast and

~3000 km north-northeast of Honolulu, Hawaii. Only a few lightning strikes were observed at this time (Fig. 4.2b). Six hours later, the storm had deepened to 990 hPa (center at 47°N, 144°W) and increasing lightning activity was observed over the cold-front. At 1200 UTC 18 December, the storm had developed a well-defined closed circulation with central pressure of 986 hPa (Fig. 4.2c). Abundant lightning was observed along the cold-front (Fig. 4.2d). At 1800 UTC on 18 December, the central pressure was 985 hPa and a secondary low center (992 hPa) had developed to the south-southeast of the original center. The storm continued to move slowly eastward, and six hours later, at 0000 UTC on 19 December, the two centers had merged, with the secondary center becoming the primary center (Fig. 4.2e). Storm central pressure of 984 hPa was observed with abundant lightning along the cold-front (Fig. 4.2f). The low center stalled near 45°N, 135°W while the cold-front continued to move westward producing a large amount of lightning. In addition, abundant lightning was observed over the cold pool area trailing the cold-front. The surface analysis at 1200 UTC on 19 December 2002 showed 972 hPa storm central pressure (Fig. 4.2g) with lightning active cold-front and cold pool (Fig. 4.2h).

#### 4.3.1.1 24-HOUR MODEL RUN

The storm deepened rapidly – from 984 to 972 hPa – between 0000 and 1200 UTC on 19 December 2002. Twelve-hour MM5 control forecast initialized at 0000 UTC and valid at 1200 UTC on 19 December 2002 showed 982 hPa storm central pressure (Fig. 4.3a), whereas the observed value was 10 hPa lower (Fig. 4.2g). Eta model's 12-

hour forecast was similarly 9 hPa too high, whereas Eta 24-hour forecast showed 11 hPa error (valid at 1200 UTC 19 December). When lightning data were assimilated into MM5, the 12-hour central pressure forecast error reduced to 2 hPa (Fig. 4.3b). Three hours later (15-hour forecast), the MM5 central pressure forecast with LDA reached 972 hPa – the same value as was observed at 1200 UTC.

The biggest differences in rainfall between the 12-hour LDA and control runs are found near the cold-front and over the cold pool which were very lightning-active, but also around the storm center to the north and west (Fig. 4.4). It is interesting to note that very little lightning was observed north of 45°N during the assimilation period (Fig. 4.2f). However, the LDA run shows a large increase in rainfall compared to control run in some areas between 45°N and 50°N. Presumably this moisture has advected there from the lightning active areas to the south. This moisture is later advected to the west side of the storm (Fig. 4.5). Note that in some areas in Figures 4.4 and 4.5, the increase in rainfall is accompanied by adjacent areas with decreased rainfall. This presumably indicates shift in the rainfall patterns rather than just increase in rainfall amount.

The largest difference in sea-level pressure between the 12-hour LDA and control runs are near the LDA run low center and over the sharp trough to the east of the center (Figs. 4.3 and 4.4). The pressure difference remains similar even after 24 hours (Fig. 4.5), although over slightly different locations.

If the majority of the lightning was observed over a narrow cold-front, hundreds of kilometers (~300-1200 km) away from the storm center, what caused the storm central pressure to drop? Figures 4.6 a-d show the evolution of 700 hPa equivalent potential

temperature field between 0000 and 1200 UTC 19 December. Although the equivalent potential temperature is conserved in a reversible moist adiabatic process and thus latent heating itself does not change it, convective temperature and moisture are adjusted in the assimilation method, resulting in altered  $\theta_e$ . Equivalent potential temperature was chosen to illustrate the evolution of warmer and moister air mass resulting from the lightning data assimilation.

Three-hour forecast show increased  $\theta_e$  values over the cold-front and to the east of the storm center. Six hours after the start of the run,  $\theta_e$  has further increased over the cold-front and cold pool area, and some increase can be also seen near the storm center. At 0900 UTC, the lightning data assimilation has stopped, but high  $\theta_e$  air have advected over the storm center resulting in reduced surface pressure. At 1200 UTC, high  $\theta_e$  air lies over the storm center from the surface up to  $\sim 300$  hPa, with largest anomalies at  $\sim 700$  hPa (Fig. 4.7a). As the atmospheric pressure at any given point is equal to the weight of the column of air overlying the point (vertically integrated density),  $\theta_e$  exclusively cannot be used to determine the surface pressure. However, the cross section of virtual temperature shows a similar distribution as  $\theta_e$  (Fig. 4.7b).

Latent heating also increased the temperature gradient across the cold-front resulting in increased winds, as stated by the thermal wind balance (Fig. 4.8).

The conclusion of this analysis is that the assimilation method adjusted the mass (and to some extent the moisture) field in the lightning-active areas. The model responded to the altered mass field by geostrophically adjusting the pressure and wind fields. The assimilation increased the temperature gradient across the front, with thermal

wind balance ensuring an increase in the along-front winds. This enhanced the advection of warm air over the storm center and dropped the surface pressure hydrostatically.

Besides changing the large-scale pressure field, LDA enhanced convective elements and post-frontal rainbands in the cold air side of the cyclone (Businger and Hobbs 1987; Businger and Walter 1987; Matejka et al.1980) (Figs. 4.6a, b). For instance, two mesoscale features with horizontal length scale of 100-150 km can be seen in Figure 4.6b near 42°N, 130°W and 42°N, 132°W. These features are associated with lower surface pressure and higher  $\theta_e$  values than the environment and are often observed in the cold air following a cold front passage. After the assimilation ended, the pressure field smoothed (Figs. 4.6c, d), likely because the model resolution was insufficient to maintain the relatively isolated convection.

The LDA run simulates relatively well the rapid pressure drop between 0000 and 1200 UTC, but raises the pressure slightly slower than observed (Fig. 4.9). The control run fails to simulate the deepening of the storm and keeps the pressure between 984 and 981 hPa. The history of the observed storm location and central pressure is based on the best subjective analysis of the surface data (e.g. Figs. 4.2a, c, e, g).

Compared to the 12-hour control forecast, the location of the low center shifted slightly to the northeast using LDA (Figs. 4.3 and 4.4). The surface analysis showed the low center at approximately 45°N, 134°W. The control forecast placed the center at 45.5°N, 134°W and the LDA run at 46.5°N, 132.5°W. Thus, the location errors are in the order of 50 and 200 km for the control and LDA runs, respectively. This may have happened because the strongest advection of high  $\theta_e$  air occurred over the eastern part of

the storm center, thus contributing to pressure falls on the storm's eastern side. However, this bias diminishes in 24-hour forecast, and the location errors are in the order of 100 and 50 km for control and LDA runs, respectively (Fig. 4.10).

#### 4.3.1.2 36-HOUR MODEL RUN

The impact of LDA on a longer simulation was investigated by starting the model run 12 hours earlier, at 1200 UTC on 18 December 2002 and similarly assimilating lightning data during the first eight hours of the model run.

Frequent lightning was observed over the cold front of the storm at the time of the model run start (Fig. 2d). The front moved towards east and north and remained very lightning active throughout the LDA period.

The MMS 24-hour forecast with LDA shows increased rainfall rates over the cold front and around the storm center compared to the control run (Fig. 4.11). The storm center has shifted slightly to the east and the surface pressure has dropped dramatically compared to the control run. At 1200 UTC 19 December, the storm central pressure in control and LDA runs were 981 and 970 hPa, respectively. During the first nine hours of the forecast, the pressure in LDA run stays within 2 hPa of the control run and observed values (Fig. 4.12). Thereafter, pressure starts to drop steeply. The rate of deepening is similar to that observed, but the LDA run deepens the storm ~3 hours earlier than observed. Similarly, the pressure in LDA run remains slightly lower than observed after the storm starts to weaken (hours 24-36 in Fig. 4.12).

#### 4.3.1.3 48-HOUR MODEL RUN

An attempt was made to start the model run at 0000 UTC on 18 December 2002 and similarly assimilate lightning data the first eight hours of the model run. Lightning over the storm started approximately at 0000 UTC, but only a few flashes were detected during the first 6 hours (Fig. 2b). More lightning was observed during the last couple of hours of the assimilation period, although these observations were far south (~700-1000 km) of the storm center. The control forecast valid at 1200 UTC on 19 December shows the storm central pressure of 981 hPa, whereas the LDA run shows 984 hPa. The observed value was 972 hPa (Fig. 2g). The storm center in LDA run is further east than in the control run and observations. LDA run keeps the secondary center to the west larger and deeper than the control run. Time series of the central pressure shows that the LDA run tracks closer to the observations than control run the first 27 hours, although the differences are relatively small (Fig. 4.13). The separation occurs at forecast hour 30, at 0600 UTC on 19 December, when the two centers merged together. LDA run kept the two centers separate, the storm center larger, and the central pressure higher than control run or observations.

The reason for the poorer performance of this LDA run may be the result of the relatively low lightning activity in the vicinity of the storm during the period of data assimilation (Fig. 2b).

#### 4.3.1.4 SENSITIVITY TESTS

Errors in lightning and rainfall measurements impact the latent heating rates that are assimilated into the model. Errors in lightning measurements have direct effect on the rainfall- and latent heating rates that are assimilated (Fig. 4.1, x-error bars). On the other hand, standard deviation in convective rainfall rates is quite large (Fig. 4.1, y-error bars) and it is important to know the impact of these uncertainties on modeling results. Errors in quantified lightning rates may result from uncertainties in the DE-model, terminator effects, and power- or network outages that disable a sensor location.

The sensitivity of the model simulations on rainfall rates was investigated by using the upper and lower boundaries for convective rainfall rate shown in Figure 4.1. These curves correspond to  $\pm$  one standard deviation in rainfall rates. The results from these two runs (hereafter referred as “+stdev” and “-stdev”) were compared to the “standard” LDA model run using the middle curve in Figure 4.1.

The difference between the standard LDA run and the +stdev run for the 24-h forecast is negligible (Fig. 4.14a). The difference in sea-level pressure field is less than 1 hPa over the whole domain and the difference in rainfall rates less than 3 mm (per three hours).

When the -stdev run was compared to standard LDA run, the differences were slightly larger, but still minor. The differences in rainfall field were generally small, except in two locations near the storm center, between 45° and 49°N (Fig. 4.14b). It should be noted that the higher rainfall rates in standard LDA run (yellow-red colors) are accompanied by higher rain rates in -stdev run (blue-white colors), indicating a shift in

rainfall pattern rather than just difference in rain rates. The difference in sea-level pressure field is generally less than 1 hPa, except near 46.5°N, 132°W, reaching 7 hPa. It should be emphasized that this difference *is not* the difference in storm central pressure. This difference is located just west of the storm center, where the pressure gradient was very high and isobars tight (Fig. 4.11b). Thus even a slight variation in storm location is emphasized in Figure 4.14b. The difference in storm central pressure was 2 hPa.

Figure 4.15 shows that the difference in central pressure during the 36-hour forecast period remains below 2 hPa between all three LDA runs. The -stdev run has slightly higher pressure than the standard LDA run. This is understandable, as the reduced latent heating forcing results in decreased  $T_v$  values over the storm center and higher central pressure. Interestingly, the +stdev run did not reduce the storm central pressure below the standard LDA run, but kept it the same or 1 hPa higher. The reason for the model's insensitivity on increased rain rates may be in the assimilation method. The latent heating scaling coefficient is limited to three (Section 4.2.2), resulting in the same heating rates with all the rainfall rates that reach the threshold.

The x-error bars in Figure 4.1 show a hypothetical  $\pm 50\%$  error in lightning rates. The corresponding two curves show that a  $\pm 50\%$  error in lightning rates has very small impact on the assimilated rainfall rates. Thus it is expected that an error of this magnitude has much less impact than  $\pm 1\sigma$  error in rainfall rates, and does not change the model results significantly.

The analysis shows that the model is relatively insensitive to errors in lightning-rainfall relationship and very insensitive to assimilated lightning rates. These results are

encouraging for lightning data assimilation, as they relax the requirements for accuracy in quantifying lightning rates (DE-model) and in deriving lightning-rainfall relationship.

#### *4.3.2. Tropical squall line over Hawaii*

A subtropical cyclone (Kona low) impacted the islands of Hawaii during the period 26-29 February 2004 (Fig. 4.16a), causing heavy rain, thunderstorms, extensive flooding and two storm-related deaths (Businger et al. 1998, Morrison and Businger 2001). The lightning associated with the squall line began around ~0000 UTC on 28 February, making an LDA run initialized at 0000 UTC feasible.

At 0600 UTC on 28 February, lightning and satellite observations show a rainband extending from southwest of the island of Hawaii, going along the west coast of Hawaii through Alenuihaha Channel to the northeast side of Maui (Fig. 4.16b). The MM5 6-hour precipitation forecast without lightning data placed the squall line over the eastern side of Oahu, ~200 km to the west of the observed position (Fig. 4.17a). Assimilation of lightning data enhanced latent heating and convection in the vicinity of the lightning active areas and shifted the squall line closer to the observed location (Figs. 4.17b, c). It should be noted that the precipitation fields shown in the MM5 simulation figures are the 3-hour accumulated rain ending at the time shown in each figure. Thus the rain band shown is slightly lagging behind the actual rain at the image time over this eastward moving system.

Six hours later in the simulation, at 1200 UTC 28 February, the control forecast places the squall line over Maui (Fig. 4.18a), whereas the LDA run shows it over the

island of Hawaii (Fig. 4.18b). Satellite image placed the squall line over the eastern side of Hawaii (Fig. 4.18c). Six hours later, at 1800 UTC, the control forecast rain band has reached Hawaii (Fig. 4.19a), whereas the LDA run rain band is ~200 km east of Hawaii, close to 153-154°W (Fig. 4.19b). The satellite image shows the coldest cloud tops approximately at the same longitude (Fig. 4.19c). At 0000 UTC 29 February, the squall line has moved further eastward as shown both in the control run and LDA simulations, and satellite observations (Fig. 4.20). Rainfall rates are higher in the LDA run throughout the forecast period, specifically during the assimilation period (Fig. 4.17b).

LDA introduces perturbations to the pressure field, specifically during the early hours of the forecast (Fig. 4.17b). The pressure field smooths after the assimilation has ended and shows lower values than the control forecast, specifically over and behind the squall line. The surface analyses showed that the lowest pressure was observed behind the squall line and remained at 1000 hPa ( $\pm 1$  hPa) during the period from 0600 UTC 28 February to 0000 UTC 29 February. During the same period, LDA run kept the low pressure behind the front at 1000 hPa, whereas in the control run, the pressure was 2-4 hPa higher (Figs. 4.17-4.20). This in turn, resulted in increased pressure gradient across the squall line and slightly stronger winds in LDA run (Fig. 4.21). A few (9) available open-ocean surface observations are plotted in Figure 4.21 with the modeled wind field. Both the control and LDA runs are in relatively good agreement with the observations.

During the LDA period, the latent heating forcing in the KF scheme produces very high vertical velocities. Vertical cross section across the squall line reveals that LDA increases  $\theta_e$  and vertical velocity in the front. In Figure 4.22a (control run), the

maximum vertical velocity is  $0.6 \text{ m s}^{-1}$ , whereas in the LDA run (Fig. 4.22b) vertical velocity of  $4.5 \text{ m s}^{-1}$  is shown at 500 hPa, above the highest  $\theta_e$  anomaly. The cross section also shows that the front in the LDA run is placed  $\sim 2$  degrees longitude more to the east than in the control run. Six hours later, after the assimilation period has ended,  $\theta_e$  field has smoothed and vertical velocities reduced (Fig. 4.23). However, the LDA run still shows higher vertical velocities than the control run ( $1.8$  and  $0.7 \text{ m s}^{-1}$ , respectively). At 1800 UTC, the control-run front is poorly defined with a relatively uniform  $\theta_e$  field and with several weak areas of upward motion (Fig. 4.24a). The LDA-run front has one well-defined area of upward motion with higher  $\theta_e$  values (Fig. 4.24b). Similar characteristics are found six hours later, although the control forecast shows better-defined area of upward motion than six hours earlier. The LDA forecast front is still  $\sim 1.8$  degrees longitude ahead of the control run front (Fig. 4.25).

To summarize the impact of LDA for this case, the analysis showed that lightning and latent heating increased  $\theta_e$  and vertical velocity where lightning was observed to the east of the control run front. Simultaneously, this increased near-surface convergence below the heat source, consistent with mass continuity. This in turn resulted not only in increased rainfall rates over the front, but also suppressed values of rainfall, vertical velocity, and  $\theta_e$  behind the front. As a result the whole system was shifted to the east.

#### **4.4. Another approach – Four Dimensional Data Assimilation**

A second lightning data assimilation method was investigated. We used MM5's Four-Dimensional Data Assimilation (FDDA) module to nudge the model's vertical

moisture profiles according to observed lightning rate at each grid point. This method also uses a lightning – convective rainfall relationship, but an extra step is required to convert the rainfall rates to vertical mixing ratio profiles. Seven different vertical moisture profiles were constructed using MM5 data over the simulation domain. Each profile was a composite of profiles found in seven different rainfall categories. Lightning rate at each grid point then determined which profile to use in FDDA observational nudging method.

We simulated the same two storms as described in the previous section. The results were qualitatively similar to the results presented in Section 4.3: compared to the control run, LDA resulted in improved storm central pressure forecast of the northeast Pacific winter storm (Figs. 4.26, 4.27) and more realistic positioning of the Hawaii squall line (Fig. 4.28).

However, it is expected that this method will not perform as robustly as the latent heating assimilation method when applied in an operational setting, because quantitative estimation of moisture profiles for FDDA runs is difficult due to uncertainties in rainfall-moisture profile relationship. Since mixing ratio is a strongly nonlinear function of temperature, the temperature must be well known when the moisture profiles for the model run are constructed. Therefore, the results using FDDA are especially sensitive to the choice of moisture profiles used. To address the sensitivity of the moisture profile to surface temperature, the relationship between rainfall and moisture profile could be divided into several temperature categories. Subsequently, the relationship would be determined between rainfall rate at certain temperature range and moisture profile.

However, this methodology is difficult to implement as the temperature at each grid point and each time step should be known before the model run begins, at the time when FDDA input file is created. The estimate of the temperature field could be retrieved from previous model forecast, but especially in the case of fast moving frontal systems, there would be uncertainties in the temperature field using this method.

#### **4.5. Summary and discussion**

The objective of this study was to investigate the impact of assimilation of quantified, long-range lightning data into a NWP model over the open ocean. Lightning data for this study were obtained from PacNet/LLDN and the data were corrected for spatially and temporally varying detection efficiency (DE) over the North Pacific, using a DE model (Chapter 2). The assimilation method was programmed in MM5's Kain-Fritsch convective parameterization scheme. The method utilizes an empirically derived lightning-rainfall relationship and nudges the model's vertical latent heating profiles according to rainfall rates derived previously from lightning and satellite data (Chapter 3).

The LDA method can be "tuned" by modifying the convective parameterization scheme, but the modifications have to be carefully chosen in order to conserve mass balance (or to keep it within certain limits) and keep the model stable. The LDA method can be made operational relatively easily allowing 8 hours of assimilation at the beginning of the model run.

Two storms over the North Pacific Ocean with quite different characteristics were simulated using the available PacNet lightning data: a poorly forecast mid-latitude cyclone over the northeast Pacific and a squall line associated with a Kona low over Hawaii.

The control forecast performed poorly and was unable to predict the rapid deepening of the storm. The forecast error in storm central pressure was 10 and 9 hPa in 12 and 24 hour forecasts, respectively. In contrast, the LDA run predicted the central pressure within  $\sim 2$  hPa of that observed, in both 12 and 24 hour forecasts.

A detailed analysis of the modeled storm revealed that latent heating increased the temperature gradient across the cold front resulting in an increase in along-front winds though thermal wind considerations. This enhanced flow increased the advection of warm air over the storm center, hydrostatically dropping the surface pressure.

Sensitivity tests showed that the model is relatively insensitive to errors in lightning-rainfall relationship and very insensitive to assimilated lightning rates.

The squall line that passed over Hawaii was a smaller, mesoscale system, with longitudinal scale of 200-300 km, representing roughly 10 model grid lengths. LDA during the first eight hours of the simulation caused the squall line to move closer to the observed location. This shift occurred during the first hours of the model run. After the assimilation had ended, the LDA simulation was able to continue the eastward movement of the rain band, keeping its location closer to observed than the control run did.

The analysis of the thermodynamic fields showed that lightning and latent heating increased  $\theta_e$  and the vertical velocity to the east of the control run front, where lightning

activity was observed. Due to the mass conservation, increased convergence developed simultaneously near surface, below the heat source. This in turn resulted not only in increased rainfall rates over the front, but also suppressed values of rainfall, vertical velocity, and  $\theta_e$  behind the front, causing an eastward shift of the whole system.

These results hold promise for the positive impact that assimilation of the long-range lightning data stream may have as a part of an operational forecasting system. The next step is to undertake a rigorous comparison of model performance with and without lightning data in an operational setting.

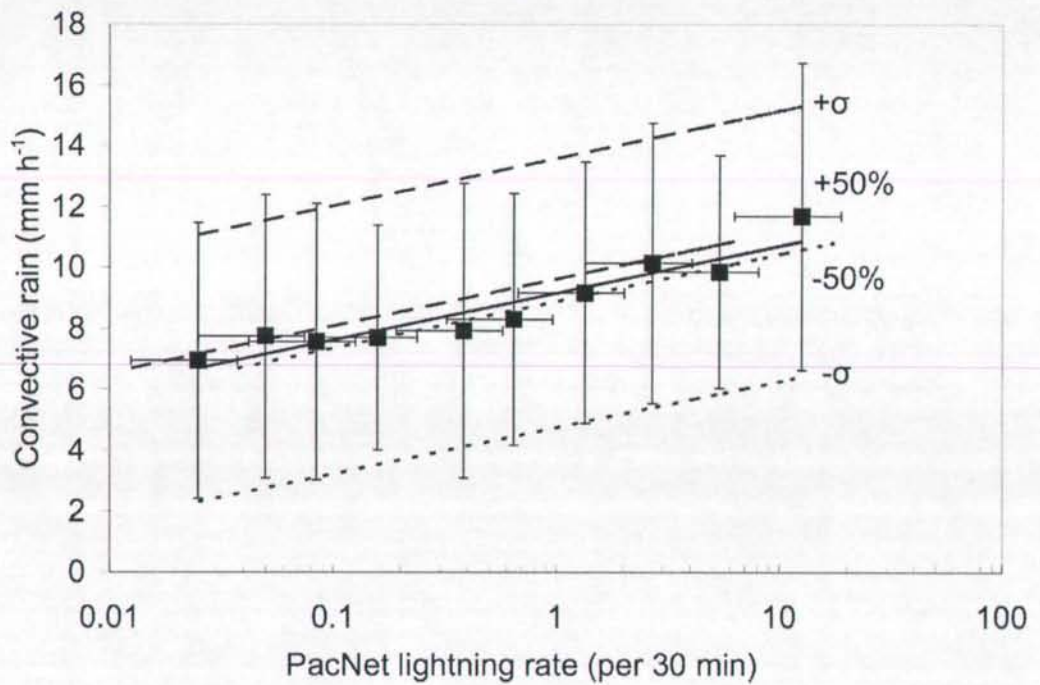


Figure 4.1 Lightning – convective rainfall relationship using PacNet lightning data and TRMM's PR rainfall data. The fitted curve in the middle (solid) is described by the equation  $y=0.67*\ln(x)+9.2$  ( $R^2=0.89$ ). The y-error bars represent  $\pm 1\sigma$  in rainfall rates. The corresponding fitted curves are described by equations  $y=0.68*\ln(x)+13.6$  ( $R^2=0.75$ ) and  $y=0.66*\ln(x)+4.8$  ( $R^2=0.92$ ), respectively. The x-error bars and corresponding curves illustrate a hypothetical  $\pm 50\%$  error in lightning rates. The upper and lower curves are described by equations  $y=0.67*\ln(x)+9.6$  and  $y=0.67*\ln(x)+8.9$ , respectively.

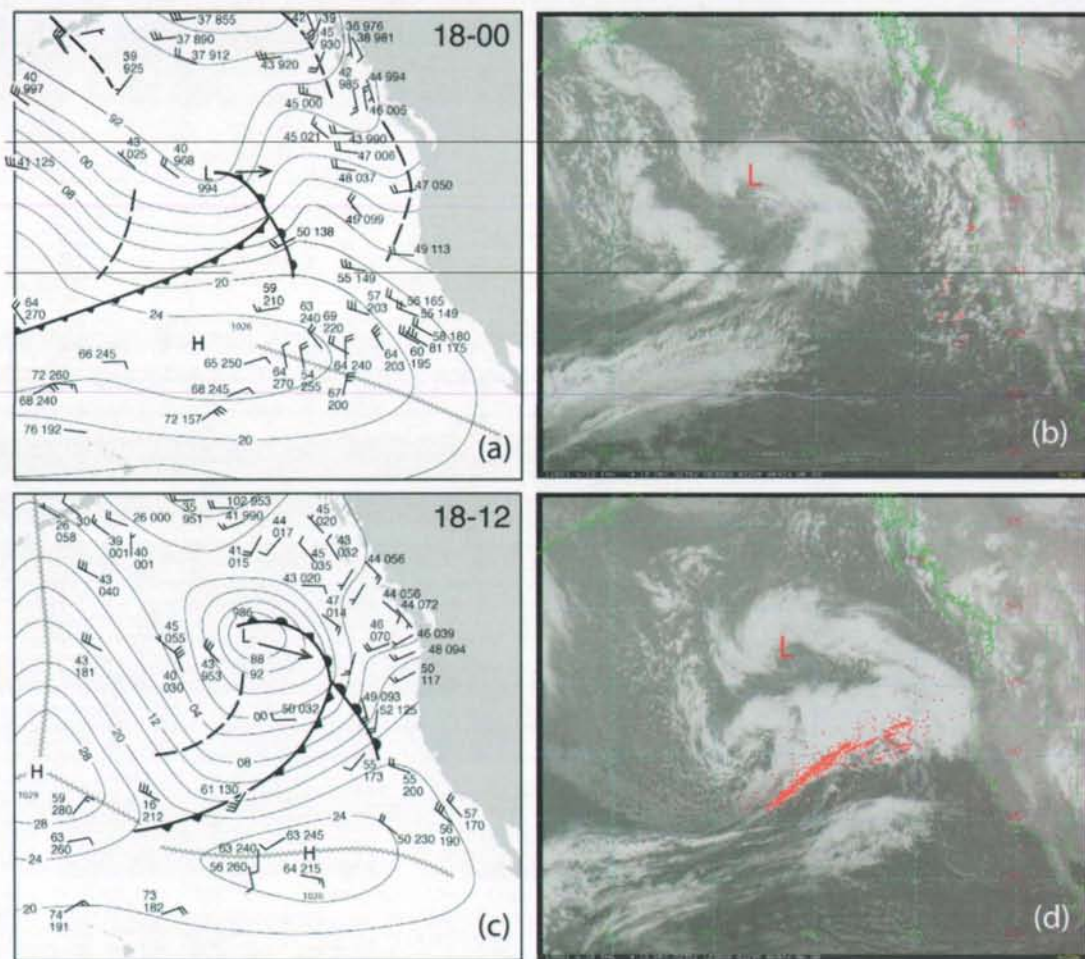


Figure 4.2 (a) Surface analysis of the eastern North Pacific Ocean valid at 0000 UTC on 18 December 2002. (b) GOES-10 IR satellite image valid at 0030 UTC on 18 December 2002 overlaid with one hour of lightning observations. Each red dot indicates a lightning flash detected by LLDN  $\pm$  30 minutes from the satellite image time. "L" marks the low center. (c) Surface analysis valid at 1200 UTC and (d) satellite image valid at 1230 UTC 18 December 2002.

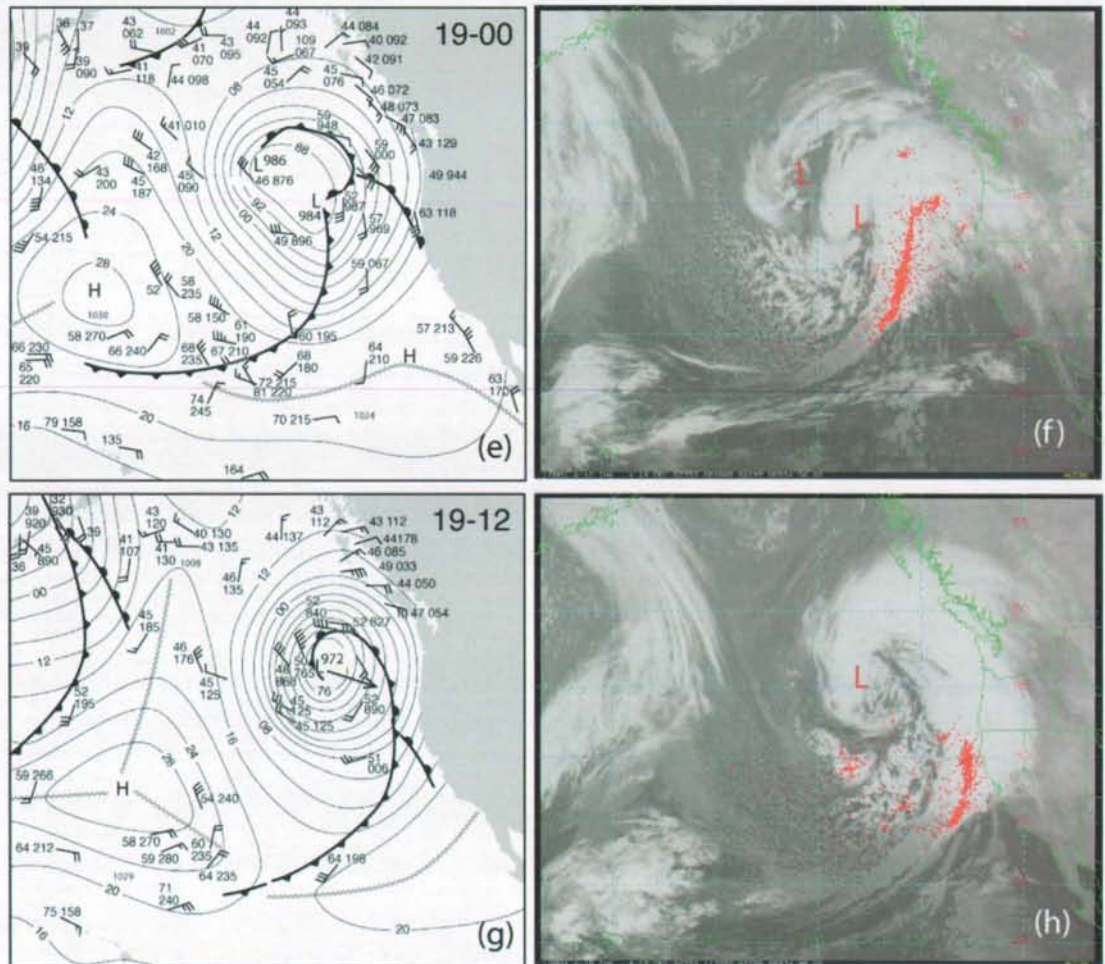


Figure 4.2 continued (e) Surface analysis valid at 0000 UTC and (f) satellite image valid at 0030 UTC 19 December 2002. (g) Surface analysis valid at 1200 UTC and (h) satellite image valid at 1130 UTC 19 December 2002.

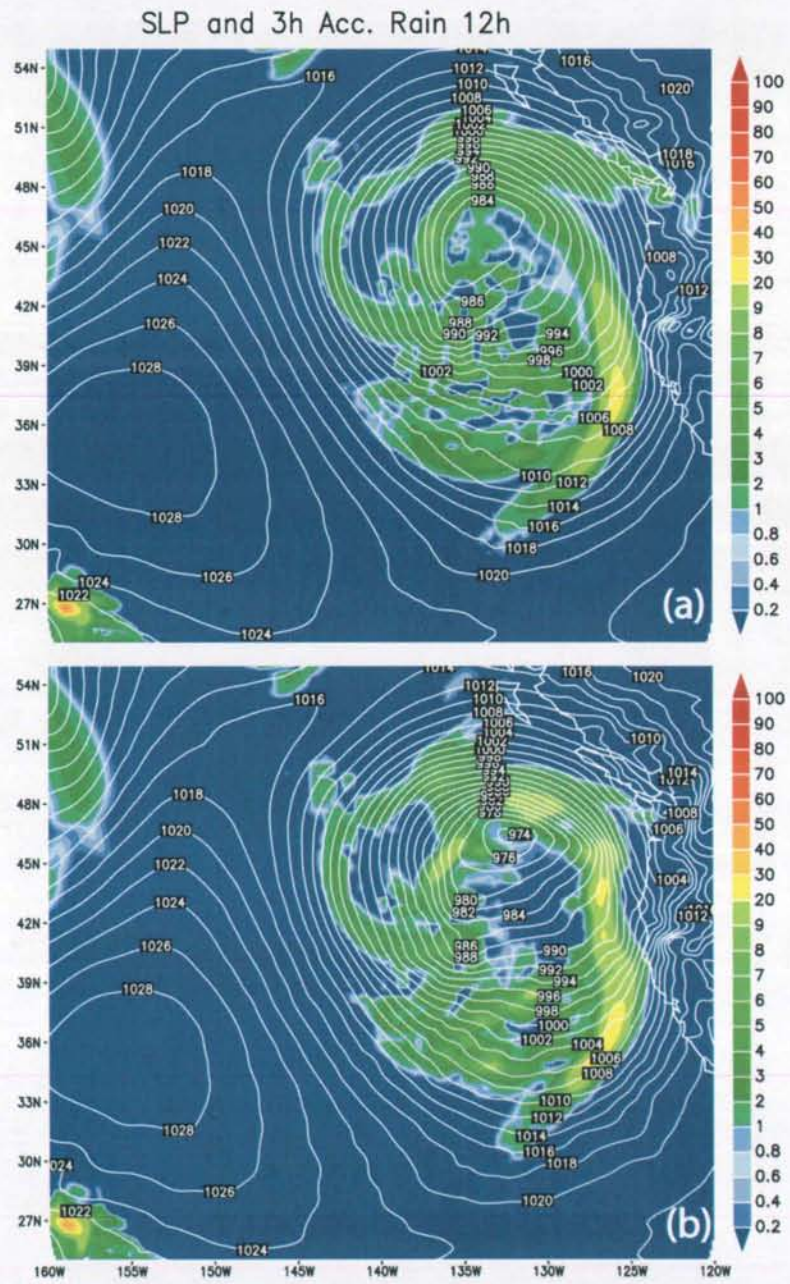


Figure 4.3 Twelve-hour MM5 forecast of sea-level pressure (hPa) and 3-h accumulated rainfall (mm) valid at 1200 UTC on 19 December 2002. (a) Control run and (b) LDA run.

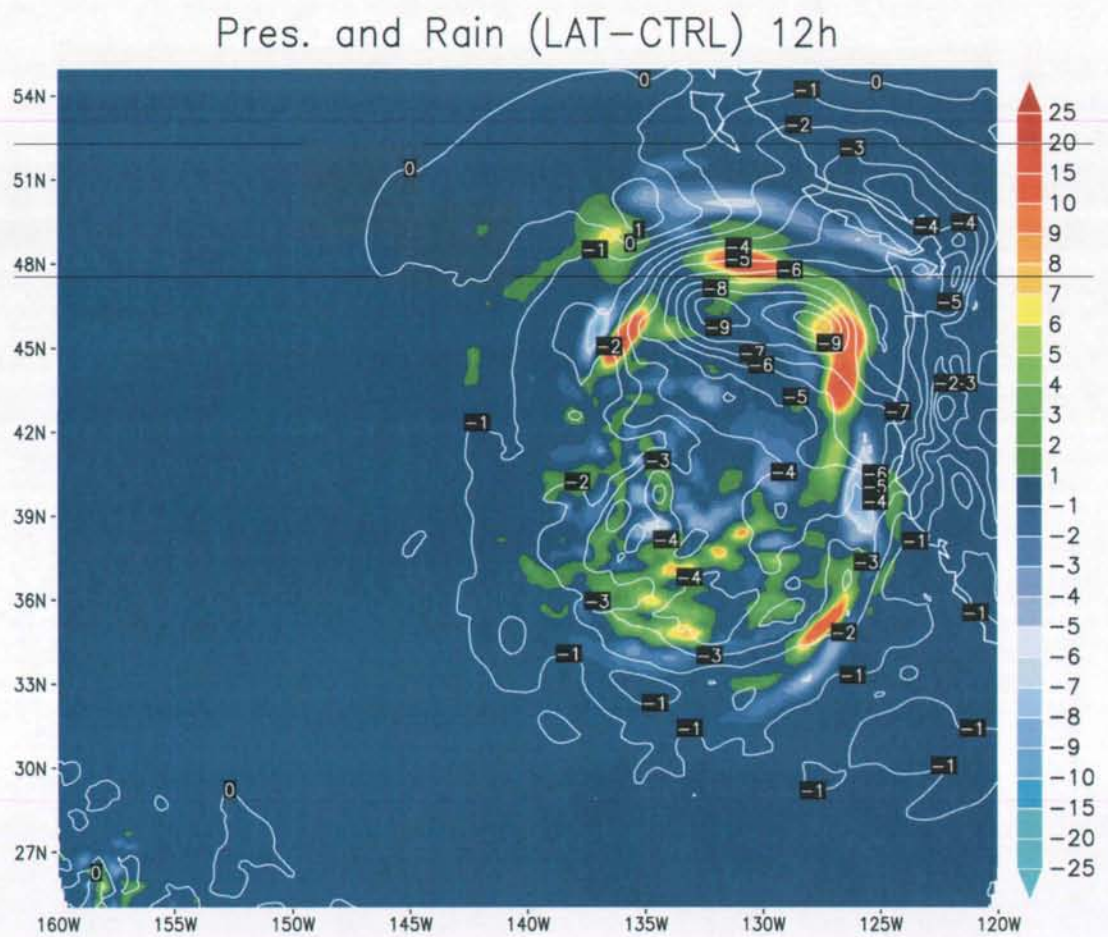


Figure 4.4 Difference in sea-level pressure (hPa) and rainfall (mm) between the LDA and control runs (as shown in Fig. 4.3). Valid at 1200 UTC on 19 December 2002. “LAT” in figure titles indicates latent heating LDA run and “CTRL” indicates control forecast.

### Pres. and Rain (LAT-CTRL) 24h

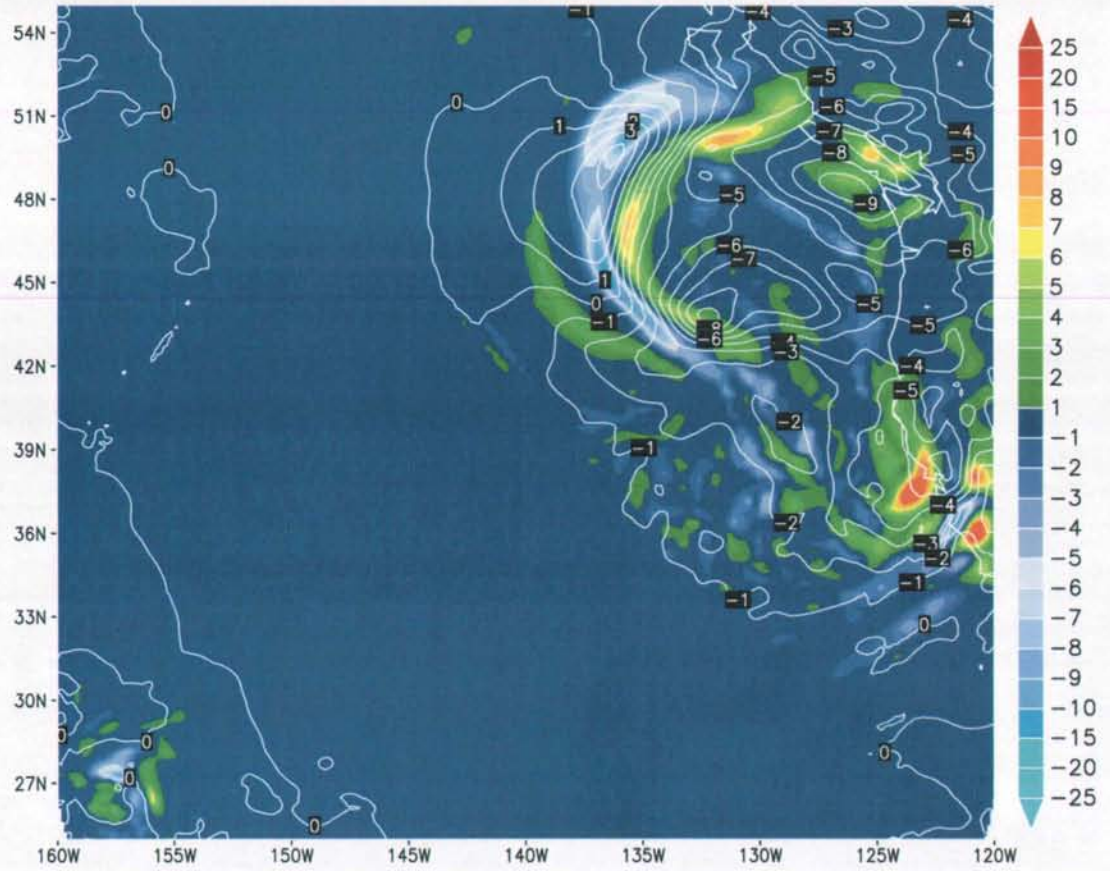


Figure 4.5 As Figure 4.4, but valid at 0000 UTC on 20 December 2002.

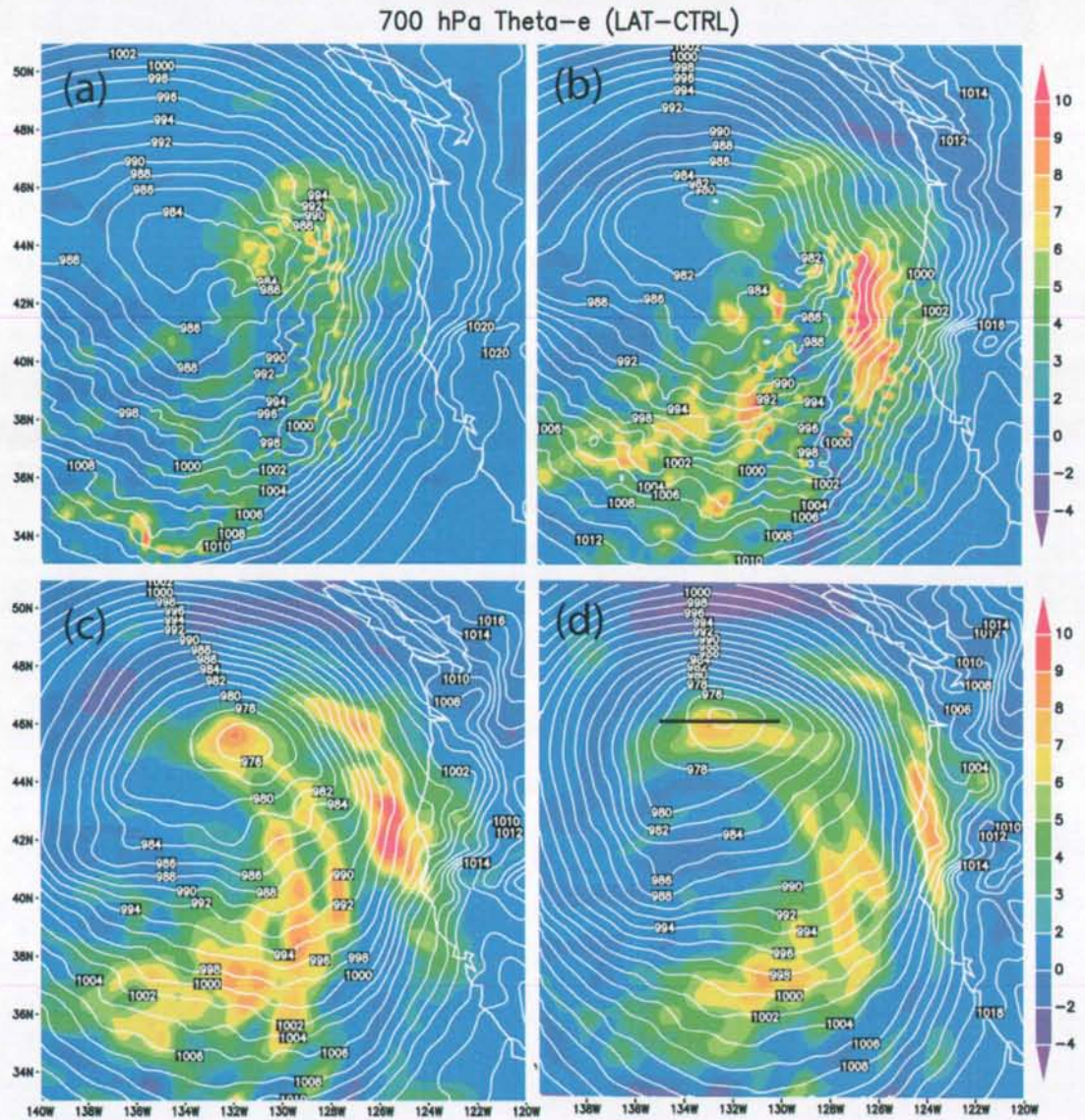


Figure 4.6 Difference in 700 hPa  $\theta_e$  between the control and LDA runs at (a) 0300 UTC, (b) 0600 UTC, (c) 0900 UTC, and (d) 1200 UTC on 19 December 2002 (shaded, [K]). Sea-level pressure is shown from the LDA run at given hour (contours, [hPa]).

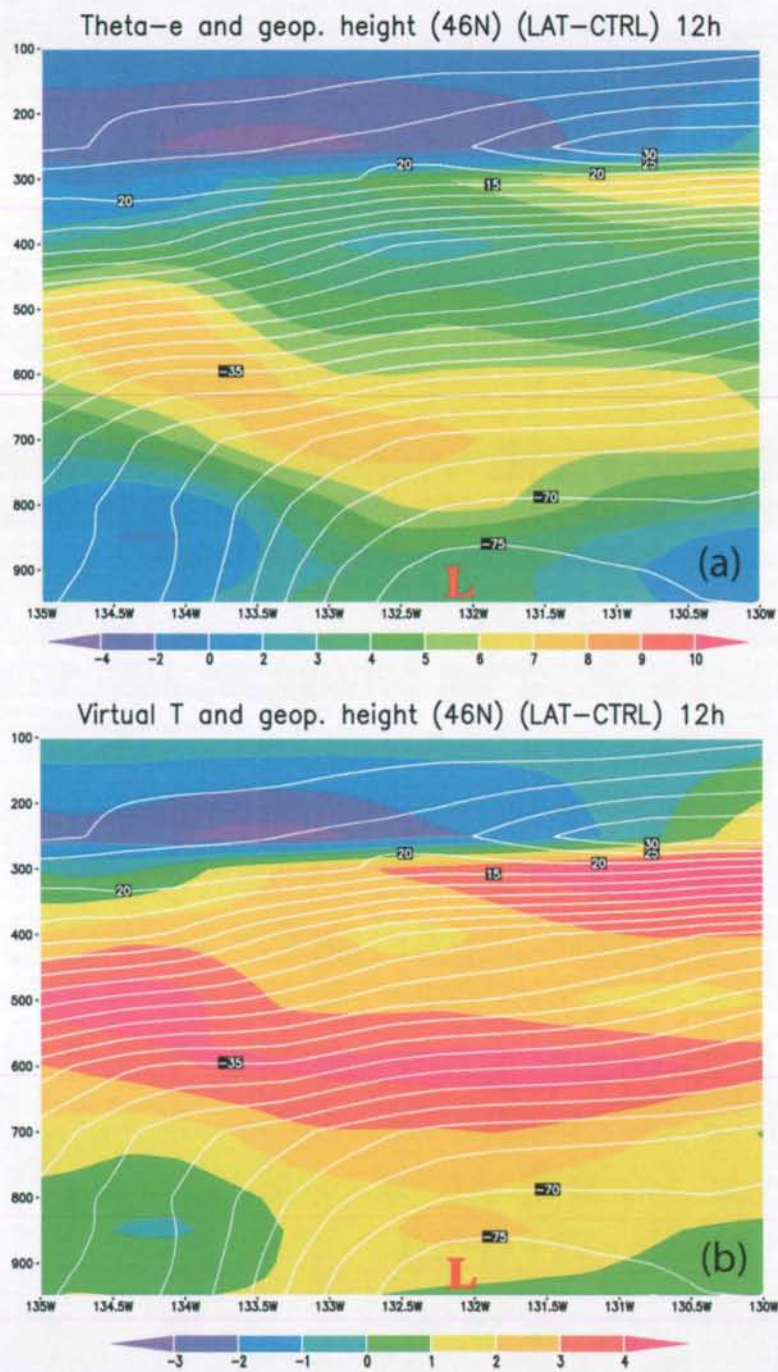


Figure 4.7 Cross-section across the storm along 46°N (horizontal line in Fig. 4.6d) valid at 1200 UTC on 19 December 2002. (a) Difference in  $\theta_e$  (K) and geopotential height (m) between the LDA and control runs. (b) Difference in  $T_v$  (K) and geopotential height (m). The red “L” indicates the position of the surface low center.

### 500 hPa Wind (LAT-CTRL) 06h

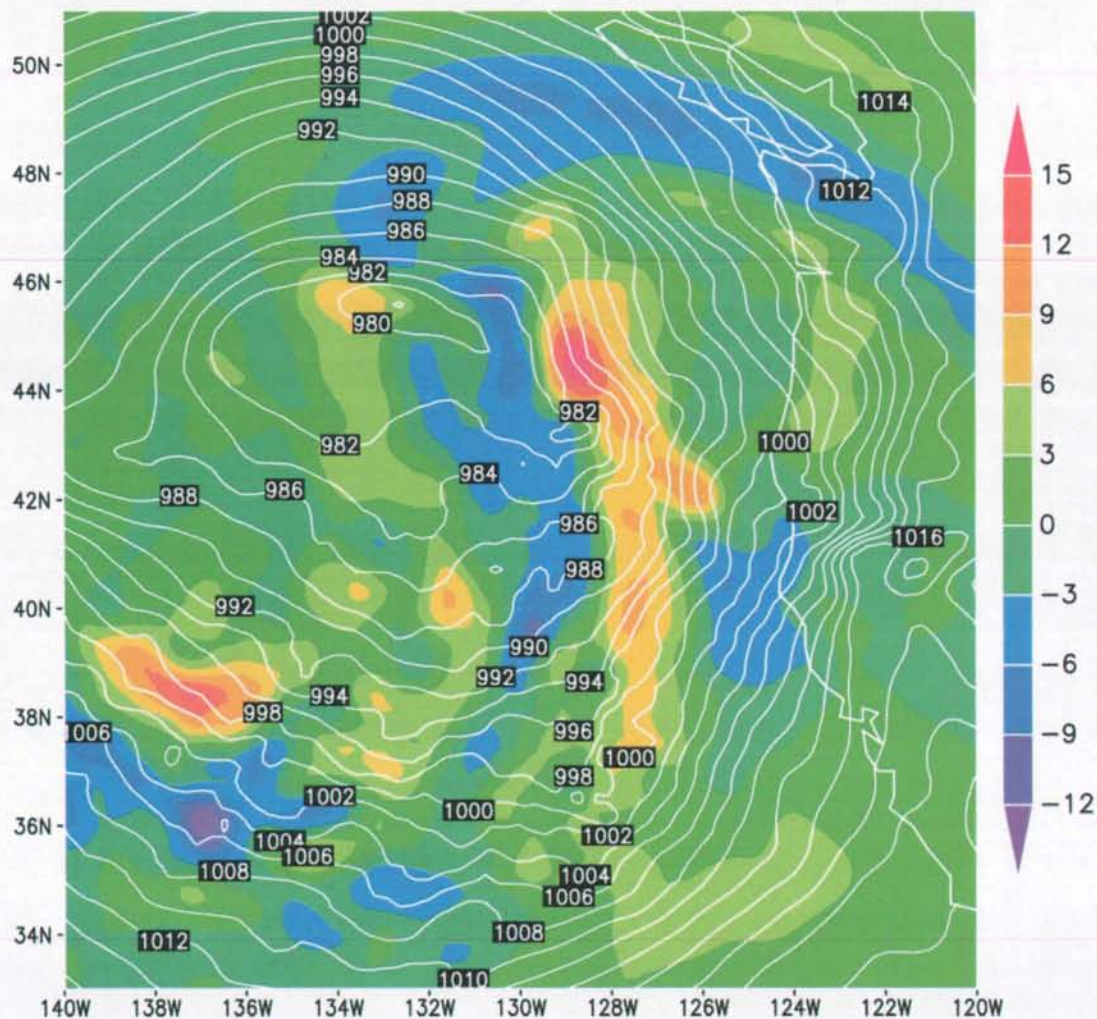


Figure 4.8 Difference in 500 hPa wind speed ( $\text{m s}^{-1}$ ) between the LDA and control runs at 0600 UTC on 19 December 2002 (shaded). Sea-level pressure (hPa) is shown from the LDA run (contours).

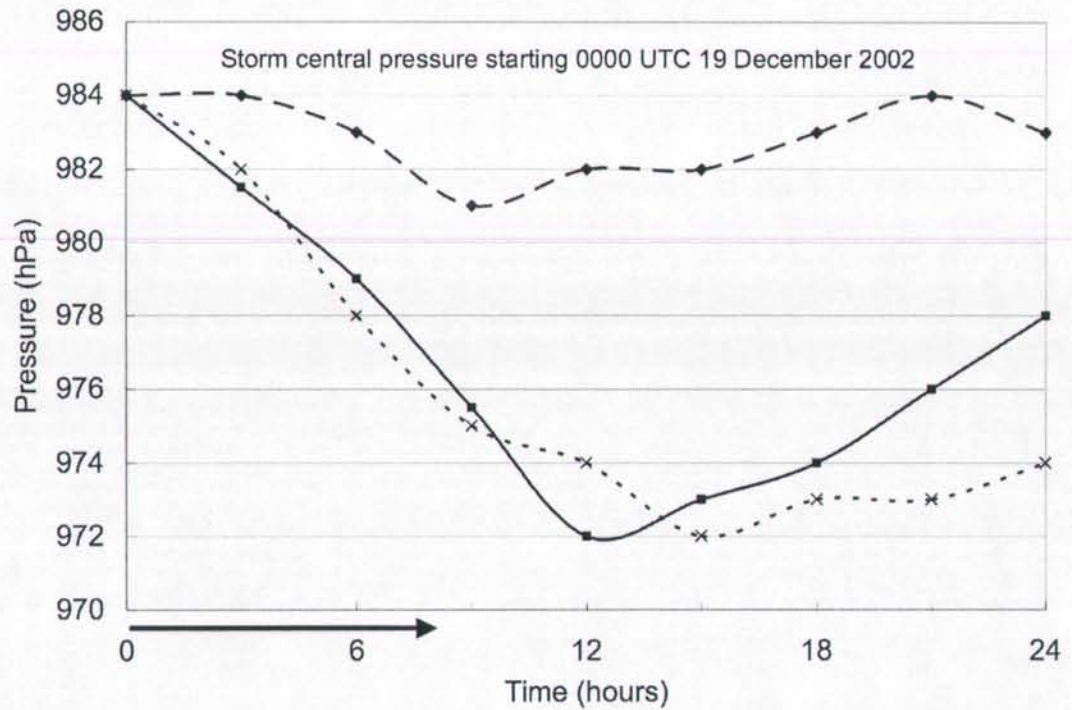


Figure 4.9 Comparison of observed storm central pressure (solid) with that predicted by MM5 with (dotted) and without (dashed) lightning data. The model was initialized at 0000 UTC 19 December 2002 and ran for 24 hours. The observed values are from the NWS North Pacific surface analyses at 0000, 0600, 1200, and 1800 UTC, and the values between them are linearly interpolated. The arrow shows the LDA period.

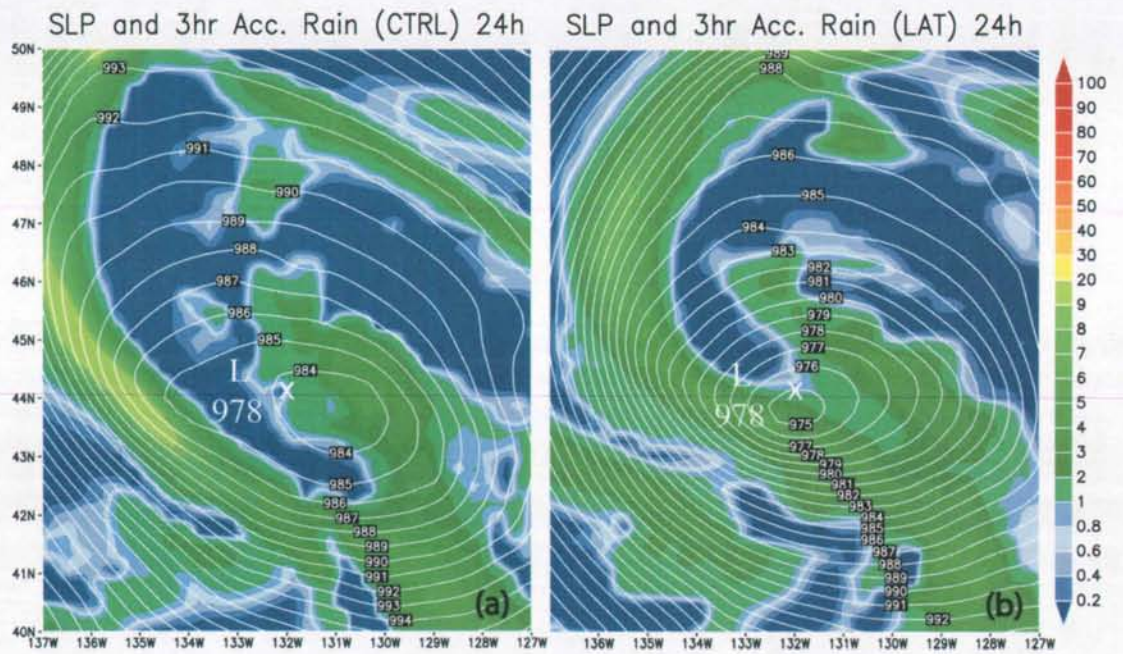


Figure 4.10 24-hour forecast of sea-level pressure and 3-h accumulated rainfall. (a) Control run and (b) LDA run. Forecast valid at 0000 UTC 20 December 2002. The observed storm central pressure was 978 hPa (marked with "x").

### SLP and 3h Acc. Rain 24h

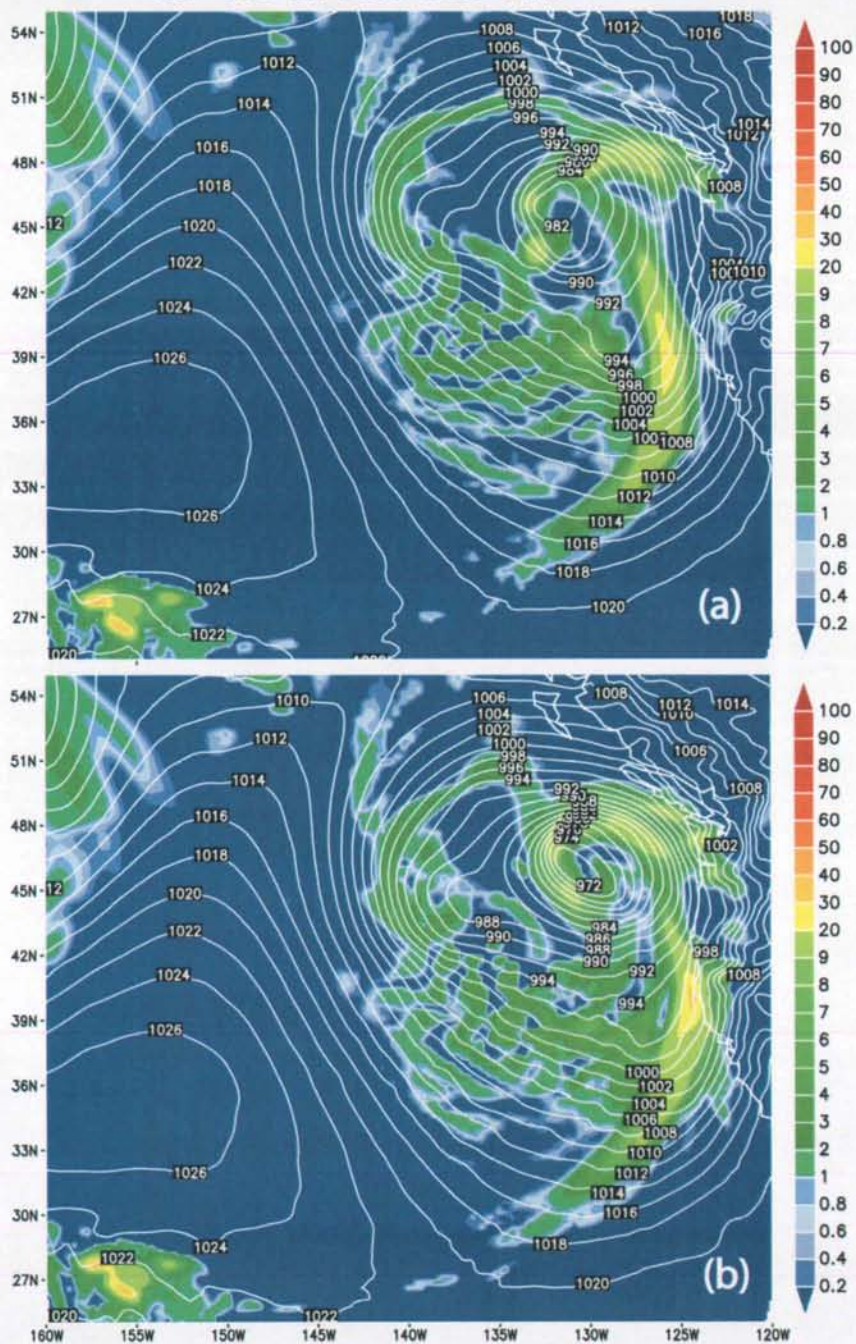


Figure 4.11 24-hour MM5 forecast of sea-level pressure (hPa) and 3-h accumulated rainfall (mm) valid at 1200 UTC on 19 December 2002. (a) Control and (b) LDA run.

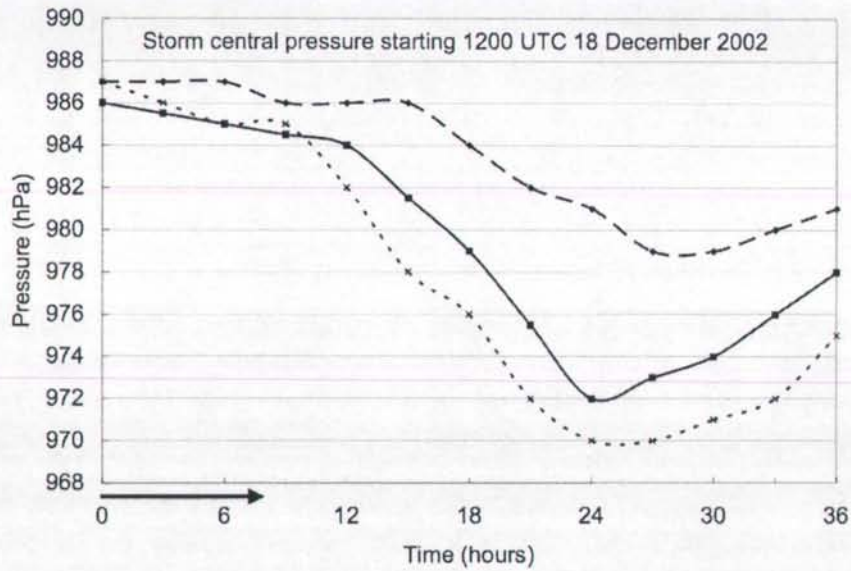


Figure 4.12 As in Figure 4.9, but the model was initialized at 1200 UTC 18 December 2002 and ran for 36 hours.

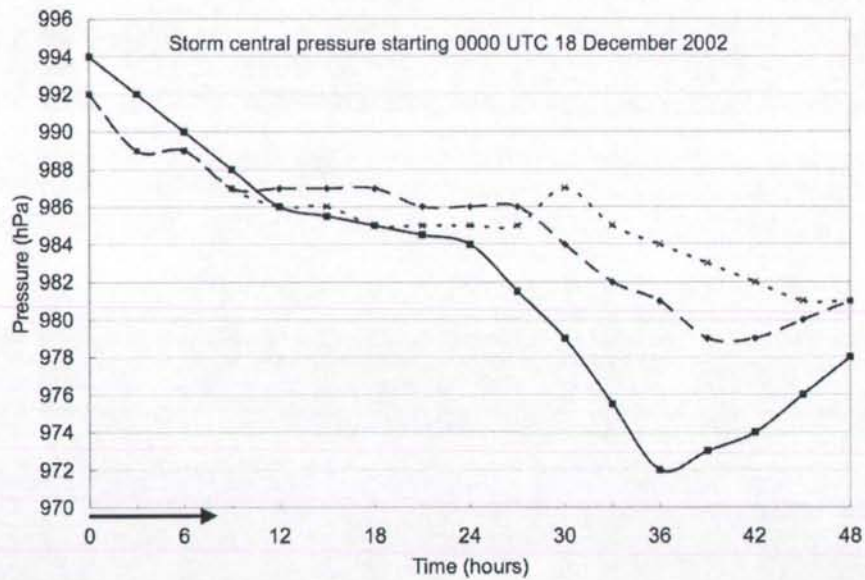


Figure 4.13 As in Figure 4.9, but the model was initialized at 0000 UTC 18 December 2002 and ran for 48 hours.

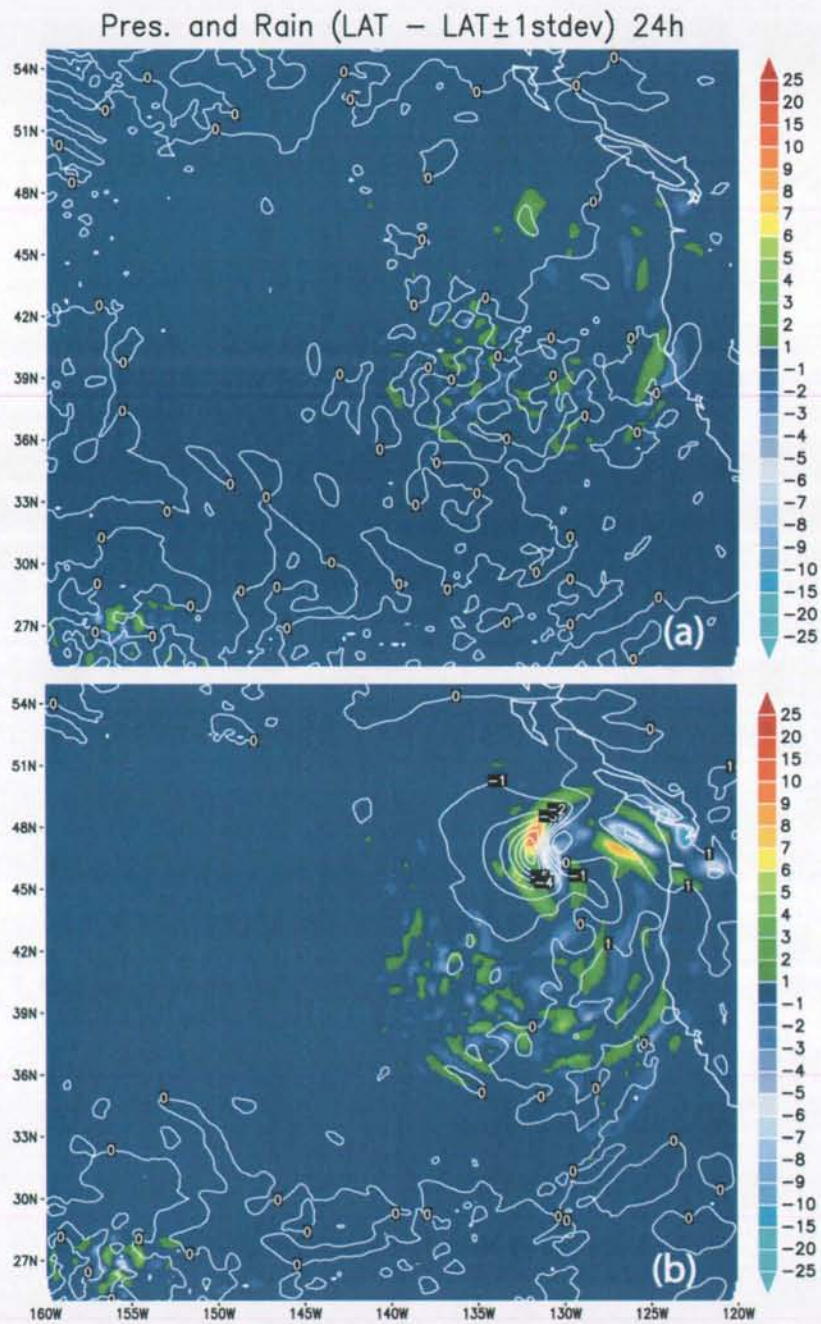


Figure 4.14 Difference in sea-level pressure (hPa) and rainfall (mm) between the “standard” LDA run and LDA run using (a)  $+1\sigma$  rainfall rates, and (b)  $-1\sigma$  rainfall rates (see Fig. 4.1). 24-h forecast valid at 1200 UTC on 19 December 2002.

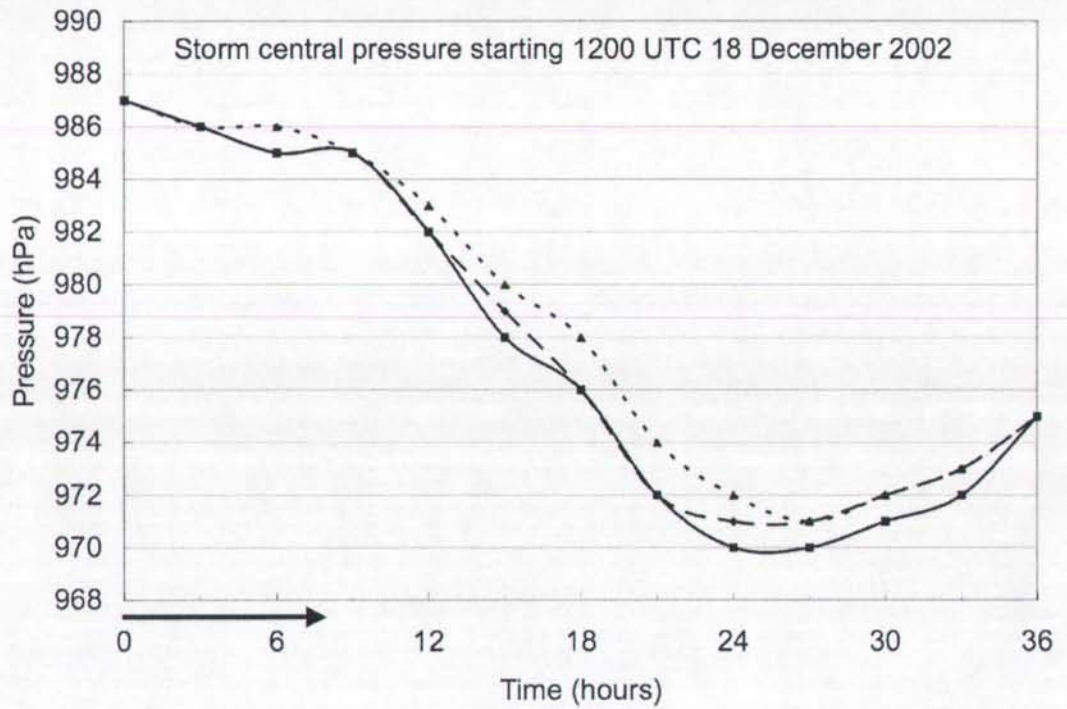


Figure 4.15 Comparison of “standard” LDA run storm central pressure (solid) with pressure from LDA run using  $+1\sigma$  rainfall rates (dashed) and  $-1\sigma$  rainfall rates (dotted). The model was initialized at 1200 UTC 19 December 2002 and ran for 36 hours.

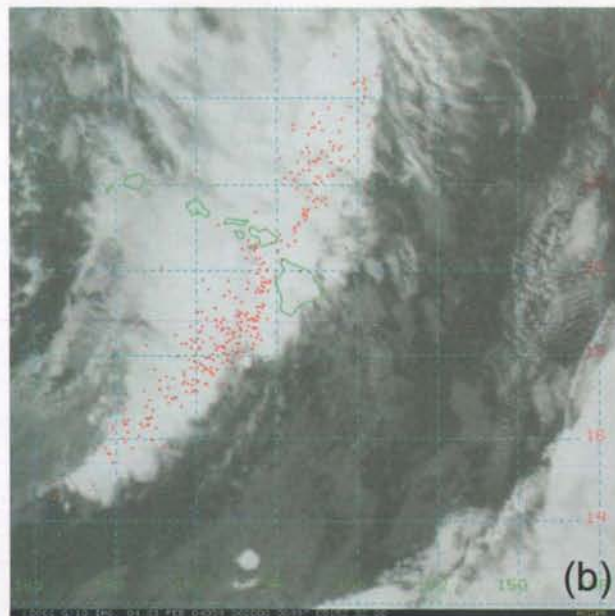
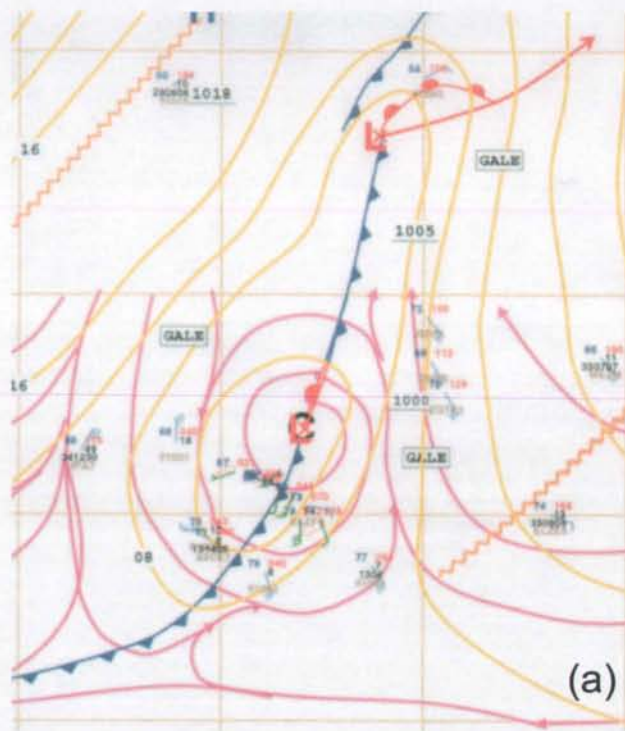


Figure 4.16 (a) Surface analysis and (b) GOES-10 IR satellite image valid at 0600 UTC on 19 February 2004. Image is overlaid with  $\pm$  one hour of lightning observations from the image time.

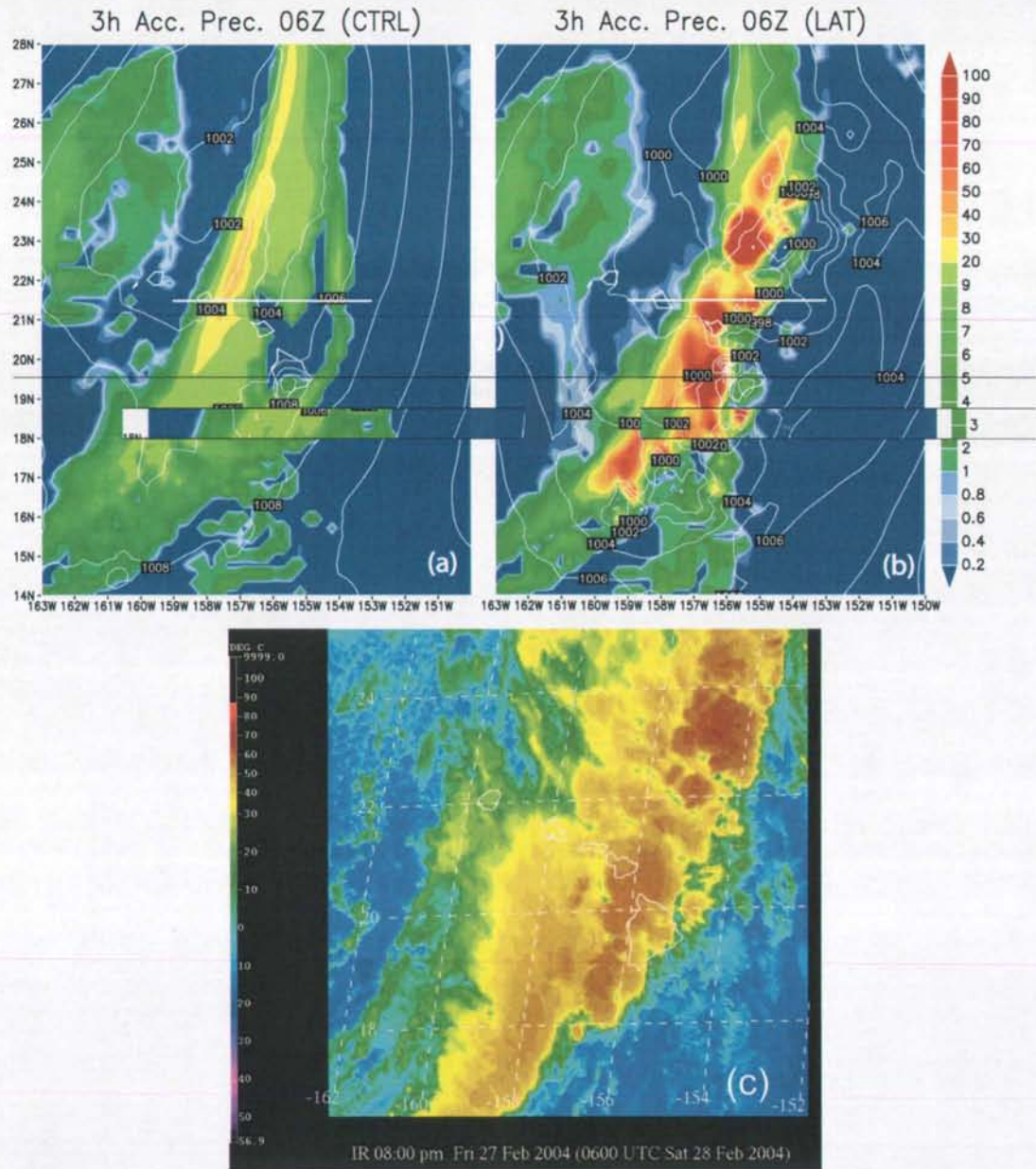


Figure 4.17 a) MM5 6-hr forecast without lightning data of precipitation (shading) and sea-level pressure (contours). b) MM5 6-hr forecast with lightning data. (c) Satellite IR image. All valid at 0600 UTC on 28 February 2004



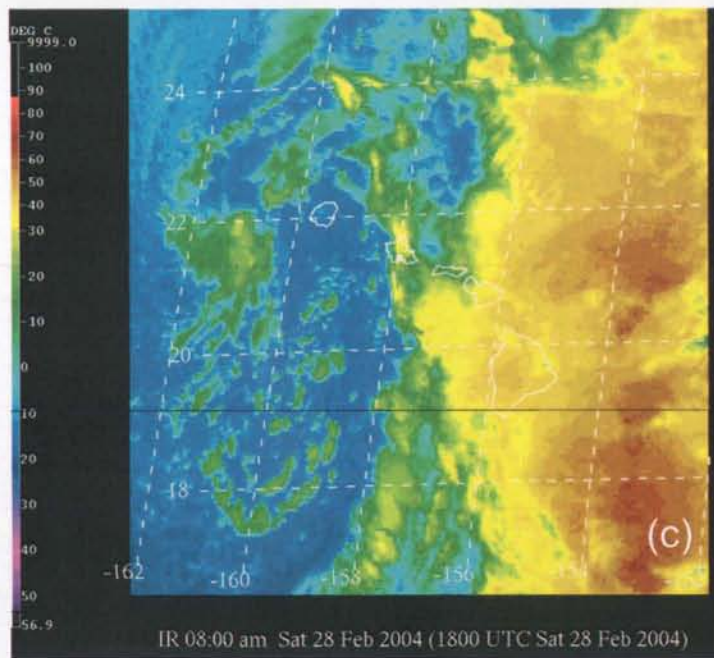
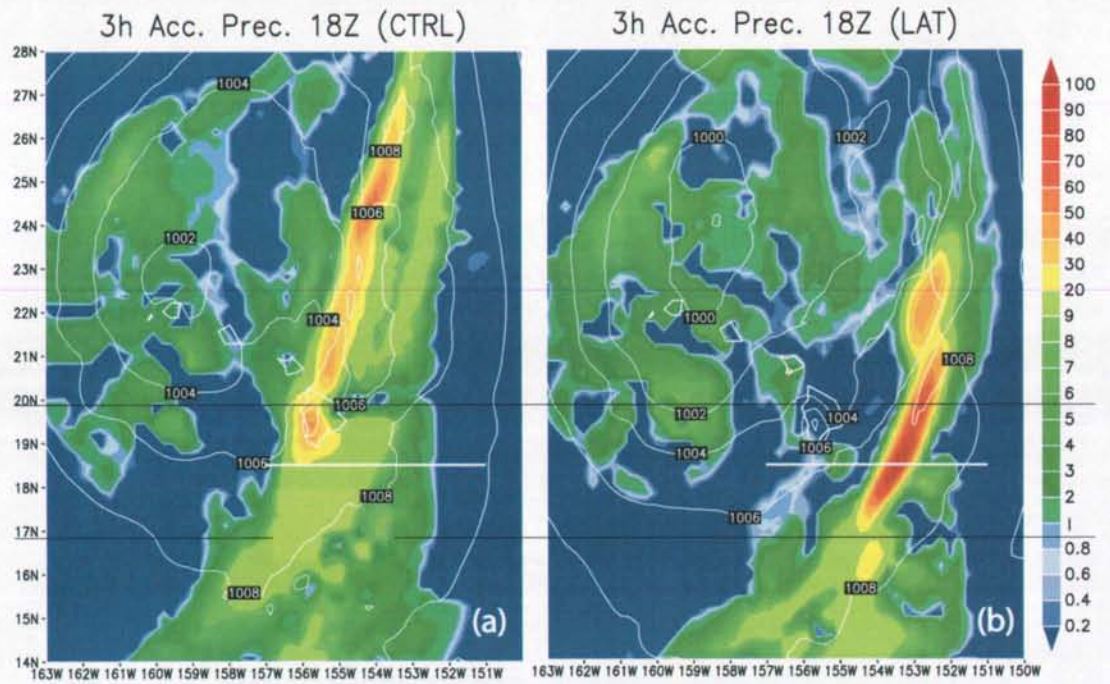


Figure 4.19 as in Figure 4.17, but valid at 1800 UTC on 28 February 2004.

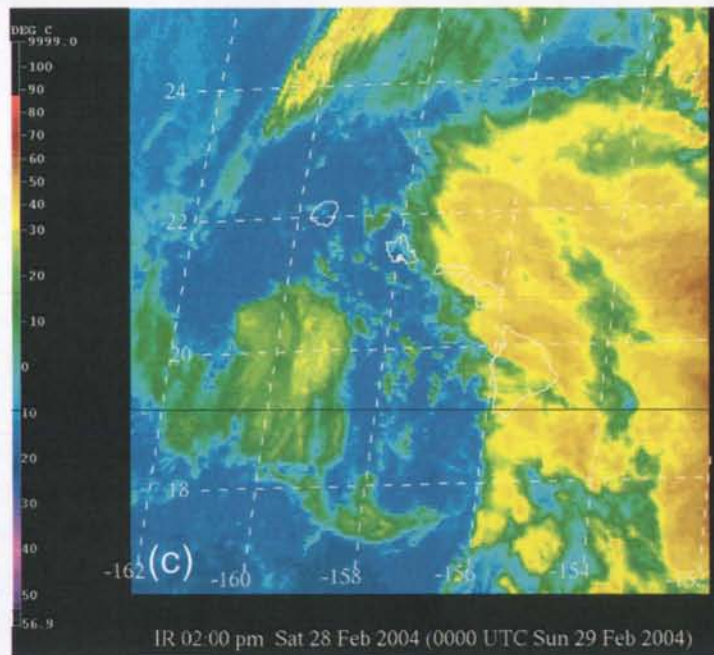
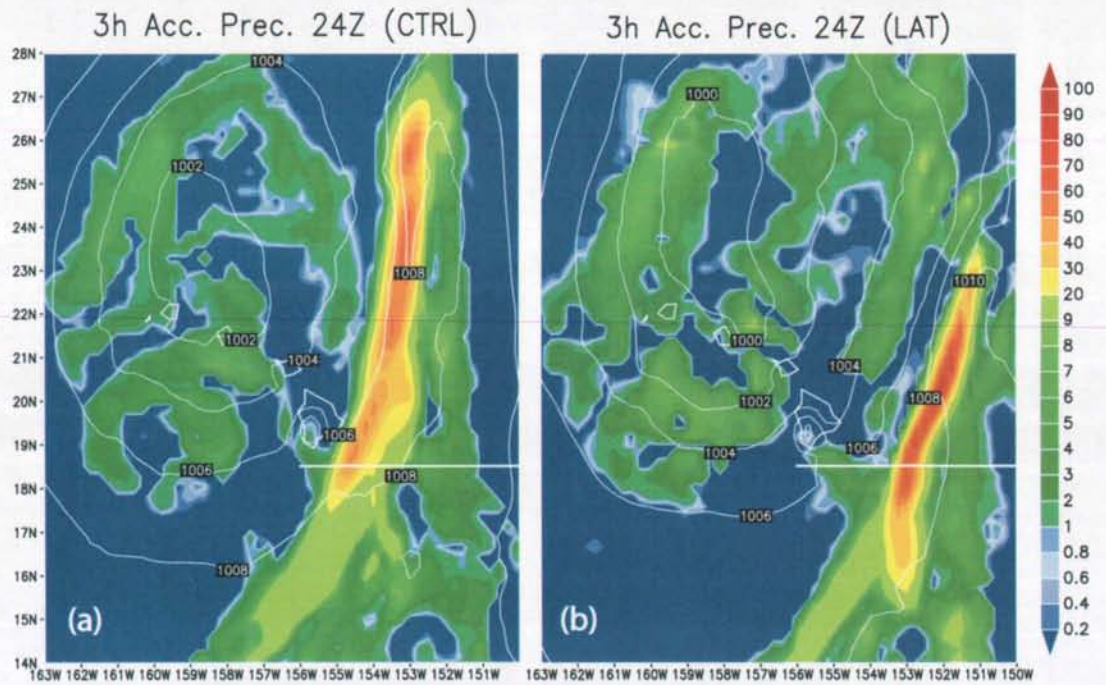


Figure 4.20 as in Figure 4.17, but valid at 0000 UTC on 29 February 2004.

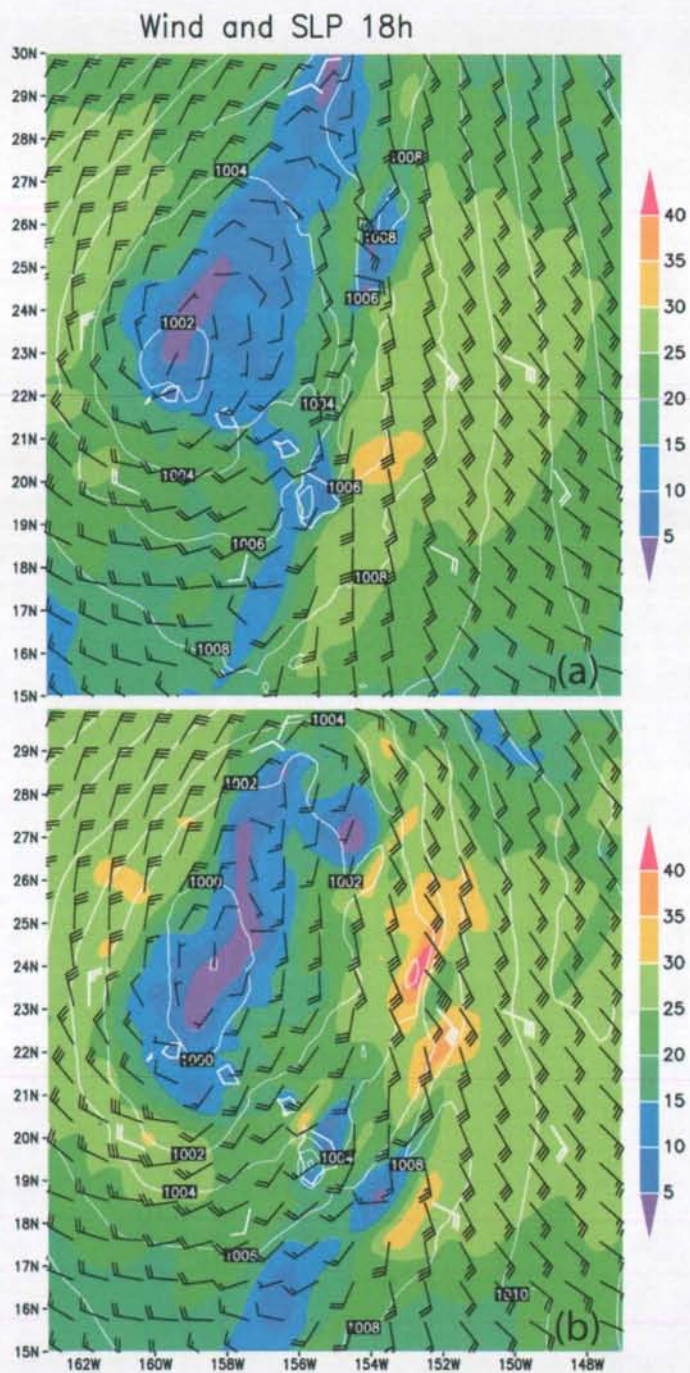


Figure 4.21 Wind speed (shaded [knots]) and sea-level pressure (contours [hPa]) valid at 1800 UTC 28 February 2004 for (a) control and (b) LDA run. White wind barbs are surface observations.

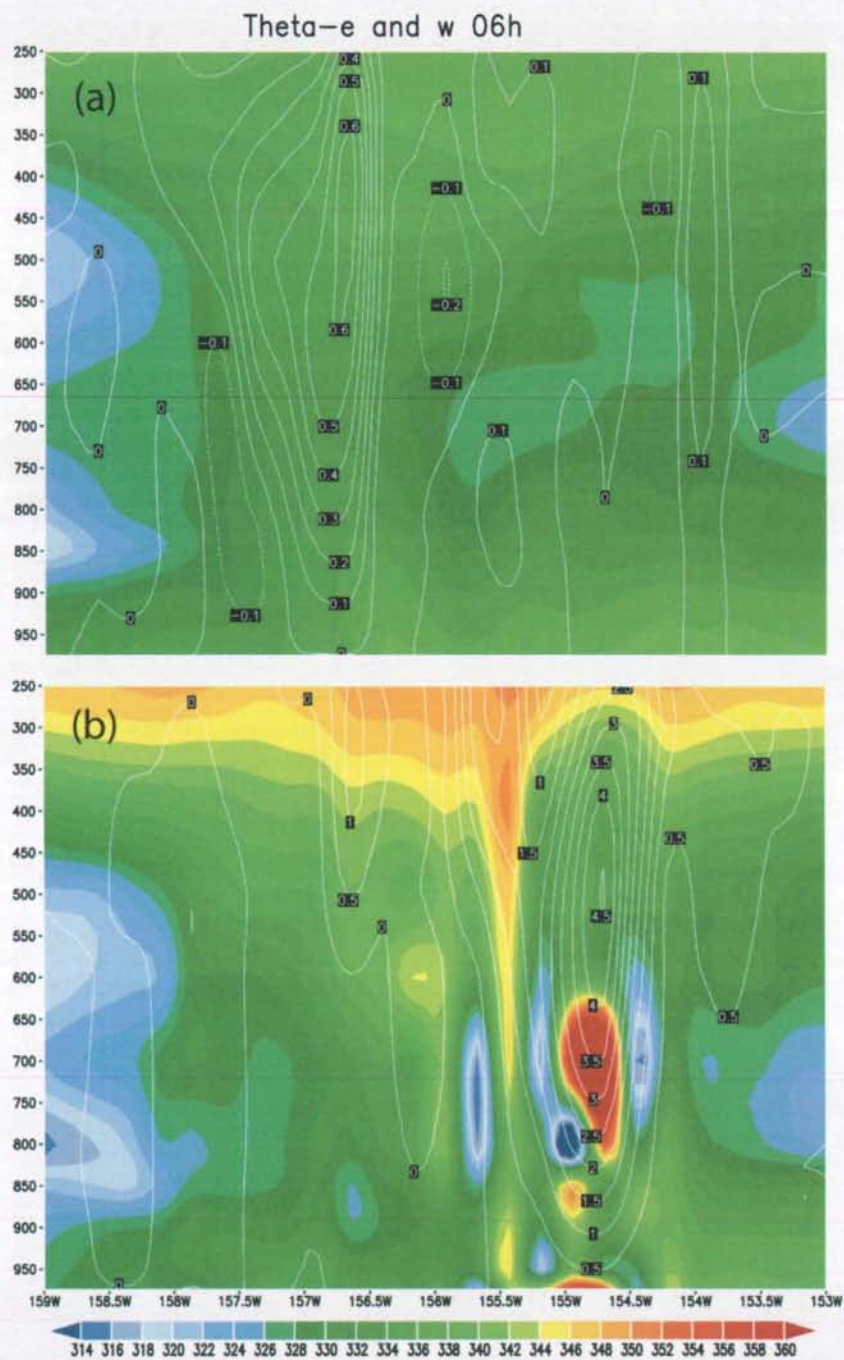


Figure 4.22 Vertical cross section across the squall line (see Figs. 4.17-4.20 for location) for (a) control run and (b) LDA run. Shaded areas show  $\theta_e$  (K) and contours show vertical velocity ( $\text{m s}^{-1}$ ). The forecast initialization time was 0000 UTC and the forecast is valid at 0600 UTC on 28 February 2004.

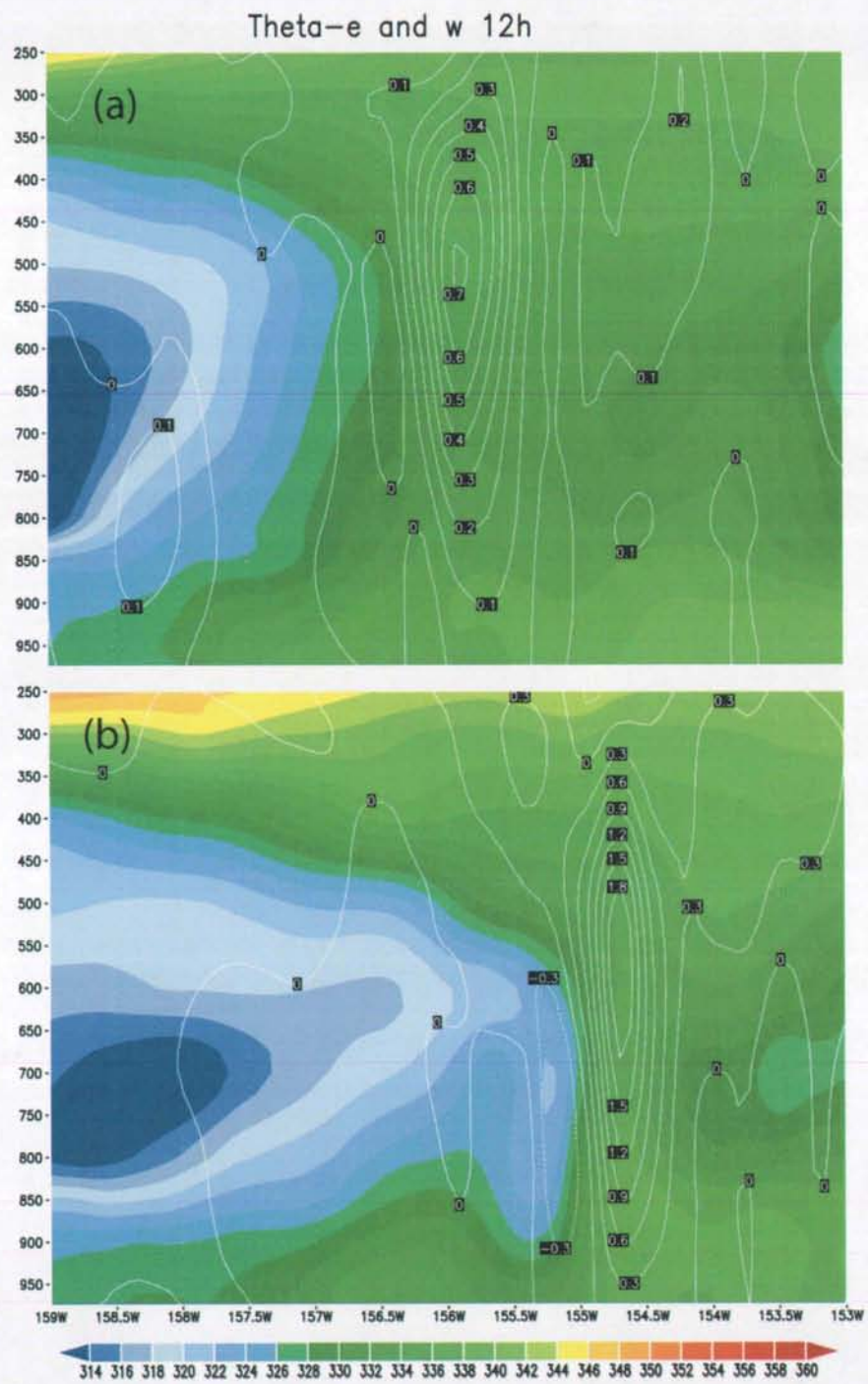


Figure 4.23 As in Figure 4.22, but forecast is valid at 1200 UTC on 28 February 2004.

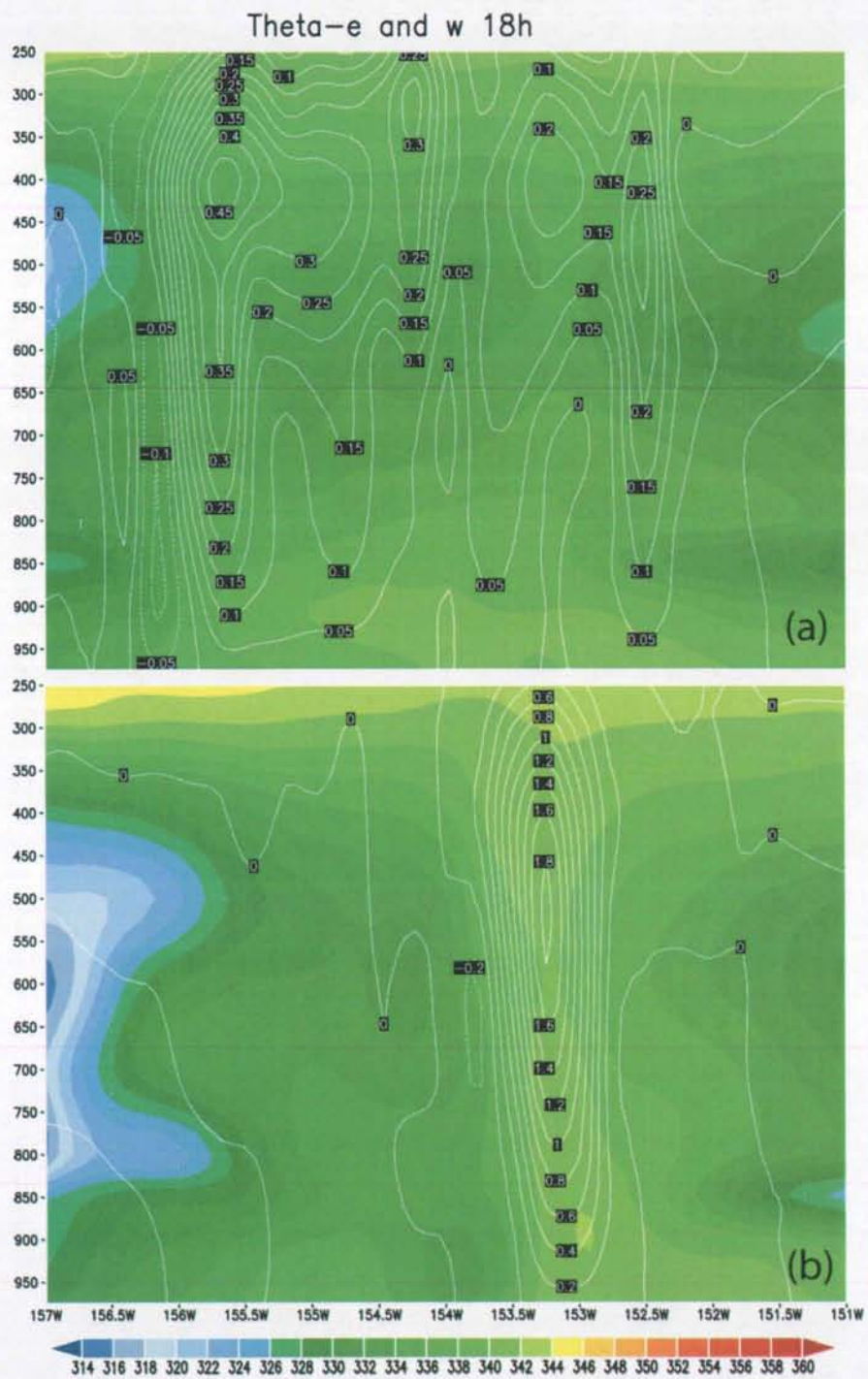


Figure 4.24 As in Figure 4.22, but forecast is valid at 1800 UTC on 28 February 2004.

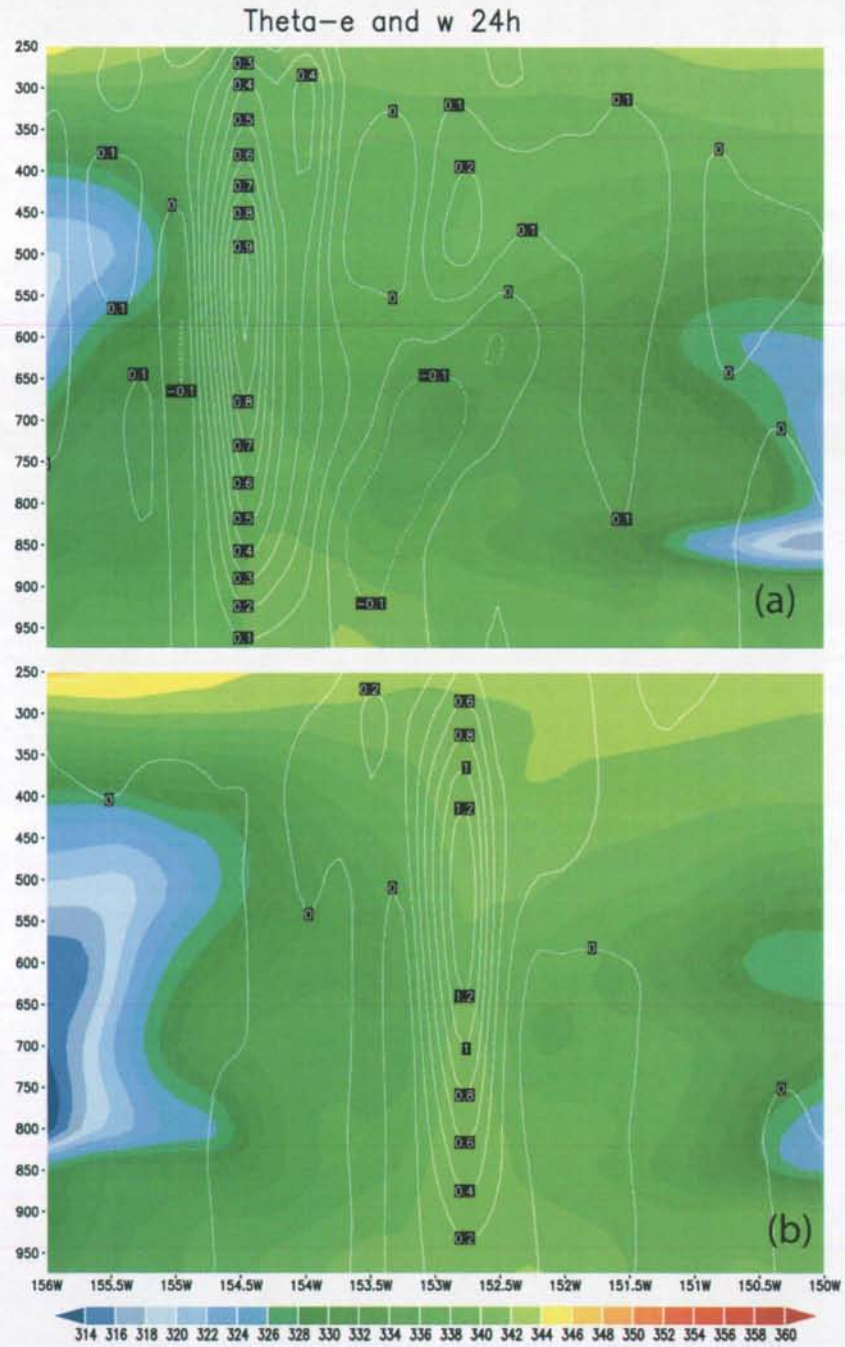


Figure 4.25 As in Figure 4.22, but forecast is valid at 0000 UTC on 29 February 2004.

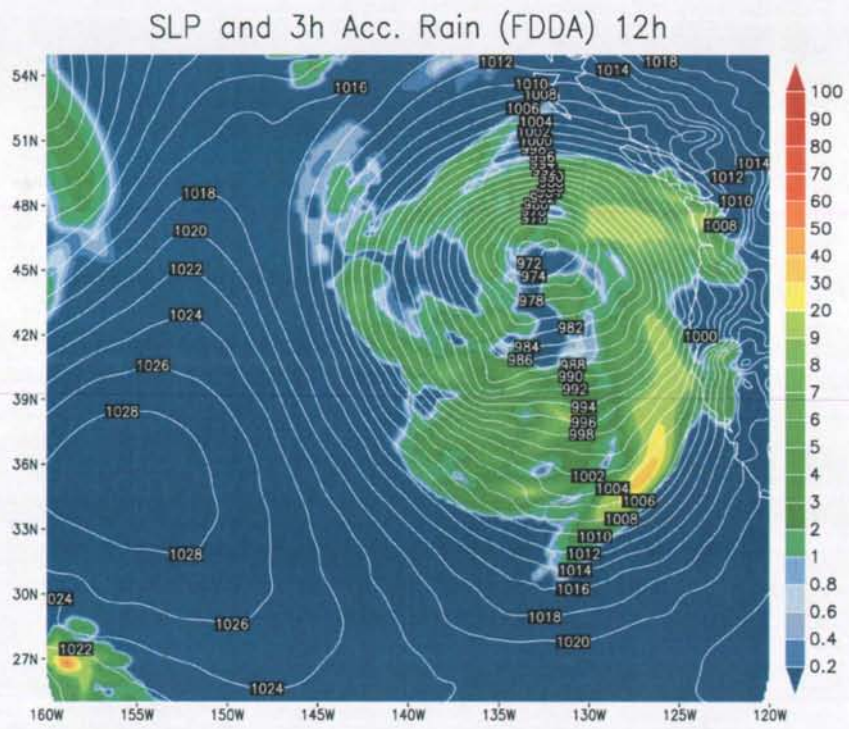


Figure 4.26 12-hour forecast of sea-level pressure and 3-h accumulated rainfall. Valid at 1200 UTC on 19 December 2002. Lightning data was assimilated using FDDA.

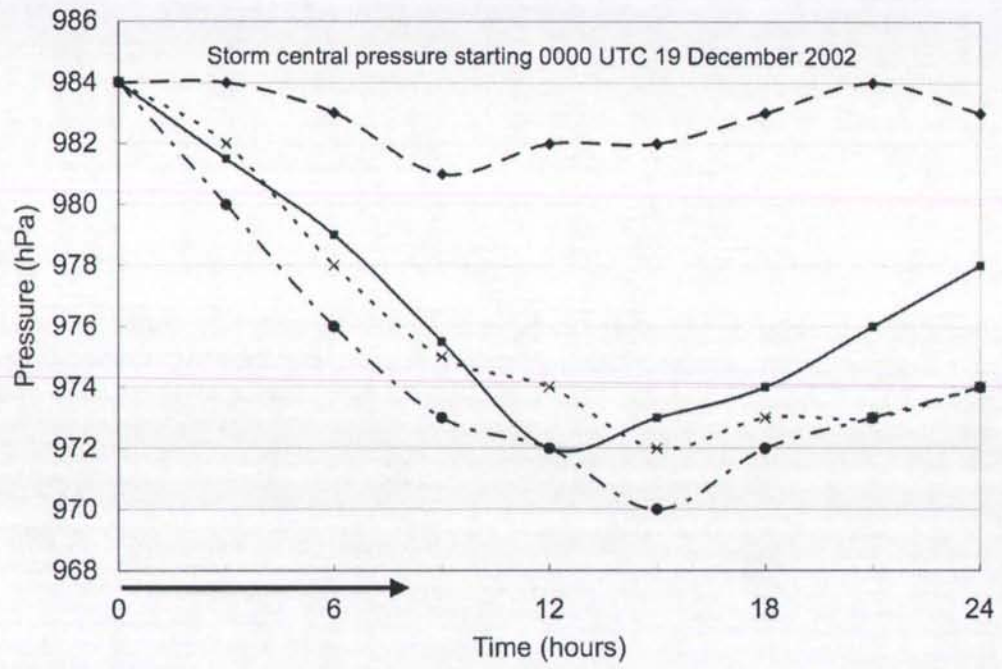


Figure 4.27 As Figure 4.10, but FDDA run added (dashed-dotted curve).

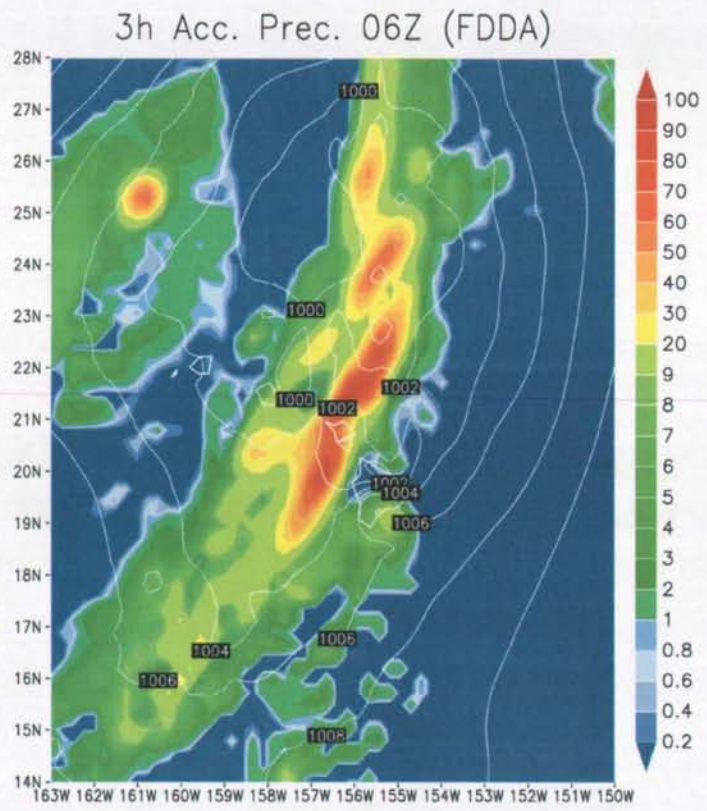


Figure 4.28 MM5 6-hr forecast of precipitation (shading) and sea-level pressure (contours) valid at 0600 UTC on 28 February 2004. Lightning data was assimilated using FDDA.

## CHAPTER 5. SUMMARY

Lightning discharges in thunderstorms generate radio frequency electromagnetic radiation called sferics. The waveguide between the earth's surface and the ionosphere allows these emissions to propagate over long distances. The new Pacific Lightning Detection Network (PacNet), as a part of a larger long-range lightning detection network (LLDN), utilizes this attribute to monitor lightning activity over the central and eastern North Pacific Ocean with a network of *ground-based lightning detectors* that have been installed on four widely spaced Pacific islands. As a result, *PacNet/LLDN* is one of the few observing systems, outside of geostationary satellites, that provide continuous real-time data concerning thunderstorms throughout a synoptic-scale area over the open ocean.

### 5.1 Focus of this research

Eastward propagating extratropical storms over the North Pacific Ocean can bring hazardous conditions to the west coast of North America. These storms' intensity and track are often poorly forecast due to the lack of observations over the Pacific Ocean and inaccurate initial conditions in NWP models. Similarly, the evolution, timing, and track of subtropical storms (Kona lows), which pose a special threat to Hawaii, are often poorly predicted.

VLF sferics observations provided by PacNet offer continuous monitoring of the location and intensity of thunderstorms over the open oceans. PacNet can be used to

derive estimates of the rainfall rate and hydrometeor characteristics from lightning data over the Pacific Ocean. Thus, lightning data can be used as a proxy for convective rainfall and latent heating rates in deep convective clouds and assimilated into numerical models over the Pacific Ocean.

## **5.2 Research conducted and main results**

Four PacNet lightning detectors have been installed on the islands of the North Pacific Ocean. Three of the sensors (Unalaska, Kona, Lihue) were installed by the author. The performance of the PacNet/LLDN was carefully assessed. Long-range lightning flash detection efficiency (DE) and location accuracy (LA) model parameters were derived with reference to accurate data from the U.S. National Lightning Detection Network (NLDN) and Puerto Rico Electric Power Authority (PREPA) lightning detection network. Model calibration procedures were detailed, and comparisons of model results with lightning observations from the PacNet/LLDN in correlation with NASA's Lightning Imaging Sensor (LIS) were presented. The daytime and nighttime flash DE in the north-central Pacific is in the range of 17-22 and 40-45 percent, respectively. DE over the Hawaii region is in the range of 21-23% and 57-61% for day and night, respectively. The median LA is in the range of 13-40 km. The results of this analysis suggest that the DE and LA models are reasonably able to reproduce the observed performance of PacNet/LLDN.

The DE and LA model output was utilized in quantitative applications of the PacNet/LLDN data-stream over the North Pacific Ocean. Thunderstorm morphology and

cloud microphysics over the central North Pacific Ocean were investigated. Lightning data from PacNet and LIS were compared to precipitation, hydrometeor, and latent heating data from TRMM's precipitation radar and microwave imager. Three years of data over the central North Pacific Ocean were analyzed, including over 2000 TRMM overpasses. The data were divided into winter (October-April) and summer (June-September) seasons. During the winter, the thunderstorms were typically embedded in cold fronts associated with eastward propagating extratropical cyclones. Summer thunderstorms were triggered by cold upper-level lows associated with the tropical upper-tropospheric trough (TUTT). Concurrent lightning and satellite data associated with the storms were averaged over  $0.5^\circ \times 0.5^\circ$  grid cells and a DE correction model was applied to quantify the lightning rates.

The results of the data analysis show a consistent logarithmic increase in convective rainfall rate with increasing lightning rates. Moreover, other storm characteristics, such as radar reflectivity, storm height, IWP, and PWP show a similar logarithmic increase. Specifically, the reflectivity in the mixed-phase region increased significantly with lightning rate and the lapse rate of Z decreased; both are well-known indicators of the robustness of the cloud electrification process. In addition, the height of the echo tops showed a strong logarithmic correlation with lightning rate.

These results have application over data-sparse ocean regions by allowing PacNet lightning data to be used as a proxy for related storm properties. By virtue of the relationship between lightning and convective rainfall rates, these data were assimilated into a mesoscale NWP model as a proxy for latent heat release in convection. A

lightning data assimilation system was programmed to Kain-Fritsch convective parameterization scheme used by MM5 mesoscale model. The method utilizes an empirical lightning-convective rainfall relationship, derived specifically for North Pacific storms. The assimilation method nudges the model's latent heating rates according to rainfall rates derived from lightning observations. Lightning data was assimilated the first 8 hours of the model run.

Two storms over the North Pacific Ocean with quite different characteristics were simulated and analyzed: a poorly forecast mid-latitude cyclone over the northeast Pacific and a squall line associated with a Kona low over Hawaii.

The control forecast performed poorly and was unable to predict the rapid deepening of the northeast Pacific storm. The forecast error in storm central pressure was 10 and 9 hPa in 12 and 24 hour forecasts, respectively. In contrast, the model run using lightning data assimilation (LDA) simulated the rapid deepening well and predicted the central pressure within ~2 hPa of that observed, in both 12 and 24 hour forecasts.

Lightning over the storm was mostly located over the cold front, several hundreds of kilometers away from the storm center. A detailed analysis of the modeled storm revealed that latent heating over the lightning active areas increased the temperature gradient across the cold front resulting in an increase in along-front winds through thermal wind balance. This enhanced flow increased the advection of warm air over the storm center, dropping the surface pressure hydrostatically.

The squall line that passed over Hawaii was placed ~200 km too far to the west by the control forecast. LDA caused the squall line to move closer to the observed location.

This shift occurred during the first hours of the model run. After the assimilation had ended, the LDA simulation was able to continue the eastward movement of the rain band, keeping its location closer to observed than the control run did.

The analysis showed that lightning and latent heating increased  $\theta_e$  and vertical velocity where lightning was observed to the east of the control run front. Simultaneously, this increased near-surface convergence below the heat source. This in turn resulted not only in increased rainfall rates over the front, but also suppressed values of rainfall, vertical velocity, and  $\theta_e$  behind the front. As a result the whole system was shifted to the east.

Sensitivity tests showed that the model is relatively insensitive to errors in lightning-rainfall relationship and very insensitive to assimilated lightning rates. These results are encouraging for lightning data assimilation, as they relax the requirements for accuracy in quantifying lightning rates and in deriving lightning-rainfall relationship.

### **5.3 Future studies**

Plans have been made to install several new PacNet sensors on the west Pacific islands, expanding the PacNet coverage further to the west. This will require re-assessment of the network performance. Some of the tools presented in this study, such as DE and LA models, can be used to re-evaluate the expanded network performance. In addition, observational assessment needs to be conducted.

Lightning data assimilation methods will be studied further. Specifically, the current system will be tuned by using several modifiable options in the assimilation

method. It will also be investigated whether lightning data can be assimilated using an existing and validated radar- or satellite data assimilation method. In that case, lightning data could be used as a proxy for vertical radar reflectivity profiles or radiances (as indicated by storm height) (Section 3.3).

Another important future study is the forecast verification. Before the operational lightning data assimilation system can be implemented, the model with LDA will be run in parallel with the operational model without LDA. A rigorous evaluation of the model performance will be undertaken using forecast verification tools.

## **APPENDIX. ESTIMATION OF IC:CG CORRECTION FOR OBSERVATIONAL DETECTION EFFICIENCY ANALYSIS**

Since no high-quality lightning data were available over the central North Pacific, data from the Puerto Rico Electric Power Authority (PREPA) LLS, described in Section 2.4, were used to estimate the IC:CG ratio. Although Puerto Rico is in the different basin than PacNet, PREPA provided suitable high-quality lightning data for determining the IC:CG ratio over the subtropical ocean. No tropical cyclone activity occurred near Puerto Rico during the period of the data set, making the data representative of a tradewind regime that characterizes both Puerto Rico and Hawaii.

The IC:CG ratio was assessed using all days in 2006 during which there were at least three LIS flashes detected over the high quality lightning data region provided by the PREPA. Only the flashes occurring over the ocean were included in the analysis. There were a total of 29 days and 347 LIS flashes that met these criteria. Each LIS flash was classified as either an IC or a CG flash. A LIS flash was classified as a CG flash if it occurred within  $\pm 100$  ms of a PREPA CG flash (first stroke time) (LIS flash duration was considered, i.e. within 100 ms of the beginning or end of a LIS flash). In order to be classified as a CG flash, a LIS flash also had to occur within 15 km of a PREPA CG flash. Two LIS flashes could not be classified as CG if they both met these criteria for only one PREPA flash (i.e. when a LIS flash was classified as a CG flash, that PREPA

CG flash was consumed and not used again for classifying any other LIS flashes). In addition, when multiple PREPA flashes matched one LIS flash, duplicate PREPA events were removed. This analysis yielded an oceanic IC:CG ratio of 4.8, which was used to normalize the LIS flash rates for the PacNet/LLDN DE estimation over the Hawaii region.

Previous studies have shown a weak correlation between IC:CG ratio and latitude, with IC:CG decreasing with increasing latitude (Pierce 1970; Prentice and Mackerras 1977; Mackerras et al. 1998). Therefore, we used a IC:CG ratio of 4.0 over the central-north region (28-38°N) to normalize the LIS flash rates. This value is consistent with the aforementioned studies.

It is possible that LIS will miss more CG flashes than cloud discharges due to the lower height of illuminated channels in the clouds, as suggested by Boccippio et al. (2001) for Optical Transient Detector (OTD). This issue was assessed by determining the number of PREPA CG flashes occurring within  $\pm 5$  s of a LIS flash, but which were not consumed by the tighter time correlation test discussed above. These flashes set a conservative bound on the number of CG flashes missed by LIS. This method yielded a slightly reduced IC:CG ratio of 4.4 for the Hawaii region, which was used to set a lower bound on the DE. IC:CG ratio for the central-north region was reduced to 3.5, accordingly.

## REFERENCES

- Alexander, G. D., J. A. Weinman, V. M. Karyampudi, W. S. Olson, and A. C. L. Lee, 1999: The effect of assimilating rain rates derived from satellites and lightning on forecasts of the 1993 Superstorm. *Mon. Wea. Rev.*, **127**, 1433-1457.
- Al'pert Y.A., 1963: Radio wave propagation and the ionosphere. *Consultants Bureau Enterprises*, New York, New York, 394 p. (pp. 245-248).
- Anderson, N. A., C. A. Grainger, and J. L. Stith, 2005: Characteristics of strong updrafts in precipitation systems over the central tropical Pacific Ocean and in the Amazon. *J. Appl. Meteor.*, **44**, 731-738.
- Anthes, R., Y-H Kuo, and J. R. Gyakum, 1983: Numerical simulations of a case of explosive marine cyclogenesis. *Mon. Wea. Rev.*, **111**, 1174-1188.
- Bauman, W.H., M.L. Kaplan, and S. Businger, 1997: Nowcasting convective activity for space shuttle landings during easterly flow regimes. *Wea. Forecasting*, **12**, 78-107.
- Beard, K.V.K., and H. T. Ochs, 1986: Charging mechanisms in clouds and thunderstorms, in the earth's electrical environment. *National Academy Press*, pp. 114-130, Washington D.C.
- Biagi, C., Cummins, K., Kehoe, K. and Krider, E., 2007: National Lightning Detection Network (NLDN) performance in southern Arizona, Texas, and Oklahoma in 2003-2004. *J. Geophys. Res.* **112(D5)**: doi: 10.1029/2006JD007341.
- Blanchard, D. O., 1998: Assessing the vertical distribution of convective available potential energy. *Wea. Forecasting*, **13**, 870-877.

- Boccippio, D. J., S. J. Goodman, and S. Heckman, 2000: Regional differences in tropical lightning distributions. *J. Appl. Meteor.*, **39**, 2231–2248.
- Boccippio, D.J., K.L. Cummins, H.J. Christian, and S.J. Goodman, 2001: Combined satellite- and surface-based estimation of the intracloud–cloud-to-ground lightning ratio over the continental United States. *Mon. Wea. Rev.*, **129**, 108–122.
- Boccippio D. J., W. J. Koshak, R. J. Blakeslee, 2002: Performance assessment of the Optical Transient Detector and Lightning Imaging Sensor. Part I: Predicted diurnal variability. *J. Atmos. Oceanic Technol.*, **19**, 1318–1332.
- Boe, B. A., J. L. Stith., P. L. Smith, J. H. Hirsch, J. H. Helsdon Jr., A. G. Detwiler, H. D. Orville, B. E. Martner, R. F. Reinking, R. J. Meitin, and R. A. Brown, 1992: The North Dakota Thunderstorm Project: A cooperative study of High Plains thunderstorms. *Bull. Amer. Meteorol. Soc.* **73**, 145-160.
- Budden, K. G., 1961: The waveguide mode theory of wave propagation. Prentice Hall, Englewood, Cliffs, N. J.
- Brennan, M.J., and G.M. Lackmann, 2005: The influence of incipient latent heat release on the precipitation distribution of the 24–25 January 2000 U.S. east coast cyclone. *Mon. Wea. Rev.*, **133**, 1913–1937.
- Bullrich, K., R. Eiden, R. Jacnicke, and W. Nowak, 1966: Optical transmission of the atmosphere in Hawaii, II. *Final Tech. Rept.*, J. Gutenberg U., Mainz, Germany, Contract No. DA-91-591-EUC-3458, 3479 pp.
- Businger, S., and P.V. Hobbs, 1987: Mesoscale structures of two comma cloud systems over the Pacific Ocean. *Mon. Wea. Rev.*, **115**, 1908–1928.

- Businger, S., and B. Walter, 1988: Comma cloud development and associated rapid cyclogenesis over the Gulf of Alaska: A case study using aircraft and operational data. *Mon. Wea. Rev.*, **116**, 1103–1123.
- Businger, S., T. Birchard, Jr., K.R. Kodama, P.A. Jendrowski, and J-J Wang, 1998: A bow echo and severe weather associated with a Kona Low in Hawaii. *Wea. Forecasting*, **13**, 576-591.
- Businger, S., T.M. Graziano, M.L. Kaplan, and R.A. Rozumalski, 2005: Cold-air cyclogenesis along the gulf-stream front: investigation of diabatic impacts on cyclone development, frontal structure, and track. *Meteor. Atmos. Phys.*, **88**, 65-90.
- Byers, H. R., and R. R. Braham Jr., 1949: The thunderstorm. U.S. Department of Commerce, 287 pp.
- Caranti J. M., A. J. Illingworth, and S. J. Marsh, 1985: The charging of ice by differences in contact potential. *J. Geophys. Res.*, **90**, 6041–6046.
- Caruso, S. and S. Businger, 2006: Synoptic climatology of subtropical cyclogenesis. *Wea. Forecasting*, **20**, 193-205.
- Cecil, D.J., S.J. Goodman, D.J. Boccippio, E.J. Zipser, and S.W. Nesbitt, 2005: Three years of TRMM precipitation features. Part I: Radar, radiometric, and lightning characteristics. *Mon. Wea. Rev.*, **133**, 543–566.
- Chang, D-E., J. A. Weinman, C. A. Morales, and W. S. Olson, 2001: The effect of spaceborne microwave and ground-based continuous lightning measurements on forecasts of the 1998 Groundhog Day Storm. *Mon. Wea. Rev.*, **129**, 1809-1833.
- Cherubini, T., S. Businger, C. Velden, and R. Ogasawara, 2006: The impact of satellite-

- derived atmospheric motion vectors on mesoscale forecasts over Hawaii. *Mon. Wea. Rev.*, **134**, 2009-2020.
- Cheze, J-L., and H. Sauvageot, 1997: Area-average rainfall and lightning activity. *J. Geophys. Res.*, **102**, 1707-1715.
- Christian, H. J., R. J. Blakeslee, and S. J. Goodman, 1992: Lightning Imaging Sensor (LIS) for the Earth Observing System. *NASA Technical Memorandum 4350*, MSFC, Huntsville, Alabama, Feb. 1992.
- Christian H. J., and Coauthors, 2003: Global frequency and distribution of lightning as observed from space by the Optical Transient Detector, *J. Geophys. Res.*, **108** (D1), 4005, doi:10.1029/2002JD002347.
- Christian, H. J., 2006: Geostationary Lightning Mapper (GLM). *12th Conference on Aviation Range and Aerospace Meteorology*, 30 January – 2 February 2006, Atlanta, GA.
- Chronis, T. G., and E. N. Anagnostou, 2003: Error analysis for a long-range lightning monitoring network of ground-based receivers in Europe, *J. Geophys. Res.*, **108**(D24), 4779, doi:10.1029/2003JD003776.
- Church, C. R., 1966: The electrification of hail. Ph.D thesis, University of Durham, 55-57.
- Clilverd, M. A., N. W. Watkins, A. J. Smith, and K. H. Yearby, 1999a: Diurnal and annual variations in 10-kHz radio noise. *Radio Sci.*, **34**(4), 933–938.
- Clilverd M.A., Thomson N.R. and Rodger C.J., 1999b: Sunrise effects on VLF signals propagating over a long north-south path. *Radio Sci.*, **34** (4), 939.

- Cram, R., and H. Tatum. 1979. Record torrential rains on the island of Hawaii, 1979. *Mon. Wea. Rev.* **107**, 1653–1662.
- Crombie, D. D., 1964: Periodic fading of VLF signals received over long paths during sunrise and sunset. *Journal of Research National Bureau of Standards, Radio Sci.*, **68D**, 27–34.
- Cummins K.L., E.P. Krider, and M.D. Malone, 1998a: The U.S. national lightning detection network™ and applications of cloud-to-ground lightning data by electric power utilities. *IEEE Transactions on Electromagnetic Compatibility*, Vol. 40, No. 4, 464-480.
- Cummins K.L., M. J. Murphy, E. A. Bardo, W. L. Hiscox, R. D. Pyle, and A. E. Pifer, 1998b: A combined TOA/MDF technology upgrade of the U.S. National Lightning Detection Network. *J. Geophys. Res.*, **103**, 9035-9044.
- Dash, J. G., and J. Wettlaufer 2003: The surface physics of ice in thunderstorms. *Can. J. Phys.*, **81**, 201–207.
- Davidson, N. E., and K. Puri, 1992: Tropical prediction using dynamical nudging, satellite-defined convective heat sources, and a cyclone bogus. *Mon. Wea. Rev.*, **120**, 2501-2522.
- Davolio, S., and A. Buzzi, 2004: A nudging scheme for the assimilation of precipitation data into a mesoscale model. *Wea. Forecasting*, **19**, 855–871.
- Del Genio, A. D., and W. Kovari, 2002: Climatic properties of tropical precipitating convection under varying environmental conditions. *J. Climate*, **15**, 2597–2615.
- Demetriades, N.W.S. and R.L. Holle, 2005: Long-range lightning applications for

- hurricane intensity and precipitation nowcasting. *Preprints, Conf. on Meteor. Appl. of Lightning Data*, San Diego, California, Jan. 9-13, Amer. Meteor. Soc., 9 pp.
- Donaldson, R.J., 1961: Radar reflectivity profiles in thunderstorms. *J. Atmos. Sci.*, **18**, 292–305.
- Donner, L.J., 1988: An initialization for cumulus convection in numerical weather prediction models. *Mon. Wea. Rev.*, **116**, 377–385.
- Ebert, E. E., and G. J. Holland, 1992: Observations of record cold cloud-top temperatures in tropical cyclone Hilda (1990). *Mon. Wea. Rev.*, **120**, 2240–2251.
- Ferguson, J. A., and F. P. Snyder, 1990: Computer programs for assessment of long wavelength radio communications, version 1.0: Full FORTRAN code user's guide. *Naval Ocean Syst. Cent. Tech. Doc. 1773, DTIC AD-B144 839*, Defense Tech. Inf. Cent., Alexandria, Va.
- Foote, G.B., and P.S. Du Toit, 1969: Terminal velocity of raindrops aloft. *J. Appl. Meteor.*, **8**, 249–253.
- Foster, J., M. Bevis, Y.-L. Chen, S. Businger, and Y. Zhang, 2003: The Ka'u storm (November 2000): Imaging precipitable water using GPS. *J. Geophys. Res.*, **108**, 4585, doi:4510.1029/2003JD003413, 002003.
- Fulton, R. and G. M. Heymsfield, 1991: Microphysical and radiative characteristics of convective clouds during COHMEX. *J. Appl. Meteor.*, **30**, 98–116.
- Futyan, J. M., and A. D. Del Genio, 2007a: Deep convective system evolution over Africa and the tropical Atlantic. *J. Climate*, **20**, 5041–5060.

- Futyan, J. M., and A. D. Del Genio, 2007b: Relationships between lightning and properties of convective cloud clusters, *Geophys. Res. Lett.*, **34**, L15705, doi:10.1029/2007GL030227.
- Gaskell, W. A., A. J. Illingworth, J. Latham, and C. B. Moore, 1978: Airborne studies of electric fields and the charge and size of precipitation elements in thunderstorms. *Quart. J. Roy. Meteor. Soc.*, **104**, 447-460.
- Gaskell W., and A. J. Illingworth, 1980: Charge transfer accompanying individual collisions between ice particles and its role in thunderstorm electrification. *Quart. J. Roy. Meteor. Soc.*, **106**, 841-854.
- Greco, M., and W.S. Olson, 2006: Bayesian estimation of precipitation from satellite passive microwave observations using combined radar-radiometer retrievals. *J. Appl. Meteor. Climatol.*, **45**, 416-433.
- Grell, G.A., J. Dudhia, and D.R. Stauffer, 1994: A description of the fifth generation Penn State/ NCAR Mesoscale Model. *NCAR Tech. Note NCAR/TN-398+STR*, 138pp.
- Göke, S., H.T. Ochs, and R.M. Rauber, 2007: Radar analysis of precipitation initiation in maritime versus continental clouds near the Florida coast: Inferences concerning the role of CCN and giant nuclei. *J. Atmos. Sci.*, **64**, 3695-3707.
- Harris-Hobbs, R., K. Giori, M. Bellmore, and A. Lunsford, 1994: Application of Airborne Field Mill data for use in launch support. *J. Atmos. Oceanic Technol.*, **11**, 738-750.
- Hiscox, W. L., E. P. Krider, A. E. Pifer, and M. A. Uman, 1984: A systematic method for

- identifying and correcting “site errors” in a network of magnetic direction finders. *International Aerospace and Ground Conference on Lightning and Static Electricity, Natl. Interagency Coord. Group, Natl. Atmos. Electr. Hazard Program, Orlando, Fla., 26–28 June.*
- Iguchi, T., T. Kozu, R. Meneghini, J. Awaka, and K. Okamoto, 2000: Rain-profiling algorithm for the TRMM Precipitation Radar. *J. Appl. Meteor.*, **39**, 2038–2052.
- Illingworth, A. J. and J. M. Caranti, 1985: Ice conductivity restraints on the inductivity theory of thunderstorm electrification. *J. Geophys. Res.*, **90**, 6033-6039.
- Johnson R. L., D. E. Janota, and J.E. Hay, 1982: An operational comparison of lightning warning systems. *J. Appl. Meteor.*, **21**, 703–707.
- Jonas, P. R., 1972: The collision efficiency of small drops. *Quart. J. Roy. Meteor. Soc.*, **98**, 681–683.
- Jones C. D., and B. Macpherson, 1997a: A latent heat nudging scheme for the assimilation of precipitation into an operational mesoscale model. *Meteor. Appl.*, **4**, 269–277.
- Jones C. D., and B. Macpherson, 1997b: Sensitivity of the limited area model to the assimilation of precipitation estimates derived from lightning data. *UKMO Forecasting Research Tech. Rep.* **212**, 11 pp.
- Jorgensen D. P., and M. A. LeMone, 1989: Vertically velocity characteristics of oceanic convection. *J. Atmos. Sci.*, **46**, 621–640.
- Junge, C. E., E. Robinson, and F. L. Ludwig, 1969: A study of aerosols in Pacific air masses. *J. Appl. Meteor.*, **8**, 340-347.

- Kain, J.S., and J.M. Fritsch, 1993: Convective parameterization for mesoscale models: The Kain- Fritsch scheme. The representation of cumulus convection in numerical models. *Meteor. Monogr.*, No. **24**, Amer. Meteor. Soc., 165-170.
- Karyampudi, V.M., G.S. Lai, and J. Manobianco, 1998: Impact of initial conditions, rainfall assimilation, and cumulus parameterization on simulations of hurricane Florence (1988). *Mon. Wea. Rev.*, **126**, 3077–3101.
- Keenan, T.D., M.J. Manton, G.J. Holland, and B.R. Morton, 1989: The Island Thunderstorm Experiment (ITEX)—a study of tropical thunderstorms in the Maritime Continent. *Bull. Amer. Meteor. Soc.*, **70**, 152–159.
- Keenan, T., S. Rutledge, R. Carbone, J. Wilson, T. Takahashi, P. May, N. Tapper, M. Platt, J. Hacker, S. Sekelsky, M. Moncrieff, K. Saito, G. Holland, A. Crook, and K. Gage, 2000: The Maritime Continent Thunderstorm Experiment (MCTEX): Overview and some results. *Bull. Amer. Meteorol. Soc.*, **81**, 2433–2455.
- Kelley, W.E., and D.R. Mock, 1982: A diagnostic study of upper tropospheric cold lows over the western North Pacific. *Mon. Wea. Rev.*, **110**, 471–480.
- Kelso, J.M., 1964: Radio ray propagation in the ionosphere, McGraw Hill, New York, 408 pp.
- Keogh, S., E. Hibbett, J. Nash and J. Eyre, 2006: The Met Office Arrival Time Difference (ATD) system for thunderstorm detection and lightning location. *Met Office, Numerical Weather Prediction : Forecasting Research Technical Report No. 488*, e-mail:nwp\_publications@metoffice.gov.uk

- Klett, J. D., and M. H. Davis, 1973: Theoretical collision efficiencies of cloud droplets at small Reynolds numbers. *J. Atmos. Sci.*, **30**, 107–117.
- Krider, E. P., R. C. Noggle, and M. A. Uman, 1976: A gated, wideband magnetic direction finder for lightning return strokes. *J. Appl. Meteor.*, **15**, 301–306.
- Kummerow, C., W. Barnes, T. Kozu, J. Shiue, and J. Simpson, 1998: The Tropical Rainfall Measuring Mission (TRMM) sensor package. *J. Atmos. Oceanic Technol.*, **15**, 809–817.
- Kummerow, C., Y. Hong, W. S. Olson, S. Yang, R. F. Adler, J. McCollum, R. Ferraro, G. Petty, D.-B. Shin, and T. T. Wilheit, 2001: The evolution of the Goddard Profiling Algorithm (GPROF) for rainfall estimation from passive microwave sensors. *J. Appl. Meteor.*, **40**, 1801–1820.
- Lane-Smith, DR, 1971: A warm thunderstorm. *Quart. J. Roy. Meteor. Soc.*, **97**, 577–578.
- Lang, T. J., L. J. Miller, M. Weisman, S. A. Rutledge, L. J. Barker III, V. N. Bringi, V. Chandrasekar, A. Detwiler, N. Doesken, J. Helsdon, C. Knight, P. Krehbiel, W. A. Lyons, D. Macgorman, E. Rasmussen, W. Rison, W. D. Rust, and R. J. Thomas, 2004: The Severe Thunderstorm Electrification and Precipitation Study. *Bull. Amer. Meteor. Soc.*, **85**, 1107–1125.
- LeMone, M. A., and E. J. Zipser, 1980: Cumulonimbus vertical velocity events in GATE. Part I: Diameter, intensity and mass flux. *J. Atmos. Sci.*, **37**, 2444–2457.
- Lin, C. L., and S. C Lee, 1975: Collision efficiency of water drops in the atmosphere. *J. Atmos. Sci.*, **32**, 1412–1418.

- Lucas, C., E. J. Zipser, and M. A. LeMone, 1994: Vertical velocity in oceanic convection off tropical Australia. *J. Atmos. Sci.*, **51**, 3183–3193.
- Lucas, C., and R. E. Orville, 1996: TOGA COARE: Oceanic lightning. *Mon. Wea. Rev.*, **124**, 2077–2082.
- Lynn, K. J. W., 1967: Anomalous sunrise effects observed on a long transequatorial VLF propagation path. *Radio Sci.*, **2**, 521–530.
- Manobianco, J., S. Koch, V. M. Karyampudi, and A. J. Negri, 1994: The impact of assimilating satellite-derived precipitation rates on numerical simulations of the ERICA IOP4 cyclone. *Mon. Wea. Rev.*, **122**, 341–365.
- Mansell, E. R., C. L. Ziegler, and D. R. MacGorman, 2007: A lightning data assimilation technique for mesoscale forecast models. *Mon. Wea. Rev.*, **135**, 1732–1748.
- Marshall, J. S., and W. M. Palmer, 1948: The distribution of raindrops with size. *J. Atmos. Sci.*, **5**, 165–166.
- Marshall, T. C. and W. D. Rust, 1991: Electric field soundings through thunderstorms. *J. Geophys. Res.*, **96**, 22,297–22,306.
- Marshall, T. C. and W. P. Winn, 1982: Measurements of charged precipitation in a New Mexico thunderstorm: Lower positive charge centers. *J. Geophys. Res.*, **87**, 7141–7157.
- Mason, B. L., and J. G. Dash, 2000: Charge and mass transfer in ice-ice collisions: Experimental observations of a mechanism in thunderstorm electrification, *J. Geophys. Res.*, **105**, 10,185–10,192.

- Matejka, T. J., 1980: Mesoscale organization of cloud processes in extratropical cyclones. Ph.D. thesis, University of Washington, 361 pp. [Available from University Microfilms, 300 Zeeb Road, Ann Arbor, MI 48106.].
- Mazur V., P.R. Krehbiel, X.M. Shao, 1995: Correlated high-speed video and radio interferometric observations of a cloud-to-ground lightning flash, *J. Geophys. Res.*, **100**, D12, 25,731-25,753.
- Mazur V., E. Williams, R. Boldi, L. Maier, and D. Proctor, 1997: Initial comparison of lightning mapping system with operational time-of-arrival and interferometric systems. *J. Geophys. Res.*, **102**, 3311–3325.
- McCaul, E. W. Jr. and M. L. Weisman, 2001: The sensitivity of simulated supercell structure and intensity to variations in the shapes of environmental buoyancy and shear profiles. *Mon. Wea. Rev.*, **129**, 664–687.
- MacGorman, D. R., and W.D. Rust, 1998: The electrical nature of storms. Oxford University Press, 422 pp.
- Mackerras, D., M. Darveniza, R. Orville, E. Williams, and S. Goodman, 1998: Global lightning: Total, cloud and ground flash estimates. *J. Geophys. Res.*, **103**, 19791–19809.
- McMurdie, L., and C. Mass, 2004: Major numerical forecast failures over the northeast Pacific. *Wea. Forecasting*, **19**, 338–356.
- McRae, W. M., and N. R. Thomson, 2000: VLF phase and amplitude: Daytime ionospheric parameters, *J. Atmos. Sol. Terr. Phys.*, **62**(7), 609–618.
- McRae, W. M., and N. R. Thomson, 2004: Solar flare induced ionospheric D-region

- enhancements from VLF phase and amplitude observations, *J. Atmos. Sol. Terr. Phys.*, **66**(1), 77 – 87.
- Moore, C.B., Vonnegut, B., Stein, B.A., and Survilas, H.J. 1960. Observations of electrification and lightning in warm clouds. *J. Geophys. Res.* **65**, 1907-10.
- Morrison, I., and S. Businger, 2001: Synoptic structure and evolution of a kona low. *Wea. Forecasting*, **16**, 81-98.
- Murphy, M. J., N.W.S. Demetriades, R.L. Holle, and K.L. Cummins, 2006: Overview of capabilities and performance of the U.S. National Lightning Detection Network. *Paper J2.5, Use of Lightning Data in Aviation Operations, 86th AMS Annual Meeting* (Atlanta, GA), Amer. Meteor. Soc.
- Nash, J. and Coauthors, 2005: Progress in introducing new technology sites for the Met Office long range lightning detection system. *Paper 2.9 WMO Technical Conference on Meteorological and Environmental Instruments and Methods of Observation (TECO-2005)*, Instruments and Observing Methods Report No. **82**, WMO/TD-No. 1265.
- Nesbitt, S. W., E. J. Zipser, and D. J. Cecil 2000: A census of precipitation features in the Tropics using TRMM: Radar, ice scattering, and lightning observations. *J. Climate*, **13**, 4087–4106.
- Nickolaenko, A.P., 1995: ELF/VLF propagation measurements in the Atlantic during 1989. *J. Atmos. Sol. Terr. Phys.*, **57**, 821-834.
- Ogawa, T. and M. Brook, 1964: The mechanism of the intracloud lightning discharge. *J. Geophys. Res.*, **69**, 5141-5150.

- Olson, W.S., C.D. Kummerow, S. Yang, G.W. Petty, W.K. Tao, T.L. Bell, S.A. Braun, Y. Wang, S.E. Lang, D.E. Johnson, and C. Chiu, 2006: Precipitation and latent heating distributions from satellite passive microwave radiometry. Part I: Improved method and uncertainties. *J. Appl. Meteor. Climatol.*, **45**, 702–720.
- Orville, R. E., E. J. Zipser, M. Brook, C. Weidman, G. Aulich, E. P. Krider, H. Christian, S. Goodman, R. Blakeslee, and K. Cummins, 1997: Lightning in the region of the TOGA COARE. *Bull. Amer. Meteor. Soc.*, **78**, 1055–1067.
- Orville, R.E., and G.R. Huffines, 2001: Cloud-to-ground lightning in the United States: NLDN results in the first decade, 1989–98. *Mon. Wea. Rev.*, **129**, 1179–1193.
- Otkin, J. A. and J. E. Martin, 2004: A synoptic climatology of the subtropical kona storm. *Mon. Wea. Rev.*, **132**, 1502-1517.
- Papadopoulos, A., T. Chronis and E. N. Anagnostou, 2005: Improving convective precipitation forecasting through assimilation of regional lightning measurements in a mesoscale model. *Mon. Wea. Rev.*, **133**, 1961-1977.
- Pappert R. A. and Hitney L. R., 1988: Empirical modelling of nighttime easterly and westerly VLF propagation in the earth-ionosphere waveguide. *Radio Sci.*, **23**, 599-611.
- Pappert, R. A., and F. P. Snyder, 1972: Some results of a mode-conversion program for VLF. *Radio Sci.*, **7**, 913– 923.
- Pessi, A., S. Businger, and T. Cherubini, 2006: Comparison of two methods for assimilation of lightning data into NWP models. *Preprints, 1st International Lightning Meteorology Conference, Tucson, Arizona, 26-27 April 2006.*

- Petersen, W. A., S. A. Rutledge, and R. E. Orville, 1996: Cloud-to-ground lightning observations from TOGA COARE: Selected results and lightning location algorithms. *Mon Wea. Rev.*, **124**, 602–620.
- Petersen, W. A., and S. A. Rutledge, 1998: On the relationship between cloud-to-ground lightning and convective rainfall. *J. Geophys. Res.*, **103**, 14025-14040.
- Petersen, W.A., S.A. Rutledge, R.C. Cifelli, B.S. Ferrier, and B.F. Smull, 1999: Shipborne dual-doppler operations during TOGA COARE: Integrated observations of storm kinematics and electrification. *Bull. Amer. Meteor. Soc.*, **80**, 81–97.
- Petersen, W. A., H. J. Christian and S. A. Rutledge, 2005: TRMM observations of the global relationship between ice water content and lightning, *Geophys. Res. Lett.*, **32**, No. 14, L14819 10.1029/2005GL023236.
- Phillips, V. T. J., A. M. Blyth, T. W. Choullarton, P. R. A. Brown, and J. Latham, 2001: The glaciation of a cumulus cloud over New Mexico. *Quart. J. Roy. Meteor. Soc.*, **127**, 1513–1534.
- Pinsky, M., A. Khain, and M. Shapiro, 1999: Collisions of small drops in a turbulent flow. Part I: Collision efficiency. Problem formulation and preliminary results. *J. Atmos. Sci.* **56**, 2585.
- Plank, V. G., 1969: The size distribution of cumulus clouds in representative Florida populations. *J. Appl. Meteor.*, **8**, 46-67.
- Pierce, E., 1970: Latitudinal variation of lightning parameters. *J. Appl. Meteor.*, **9**, 194 - 195.
- Porter, J. N., 1988: Marine aerosol: Their measurement and influence on cloud base

- properties. Master's thesis, Univ. of Hawaii, Department of Meteorology, Honolulu.
- Prentice, S., and D. Mackerras, 1977: The ratio of cloud to cloud-ground lightning flashes in thunderstorms. *J. Appl. Meteor.*, **16**, 545–549.
- Pruppacher, H. R., 2000: Microphysics of clouds and precipitation, Kluwer Academic Publishers, Norwell, Mass. pp. 792-852,
- Pruppacher, H. R., and J. D. Klett, 1978: Microphysics of clouds and precipitation. D. Reidel, 714 pp.
- Puri, K., and M. Miller, 1990: The use of satellite data in the specification of convective heating for diabatic initialization and moisture adjustment in numerical weather prediction models. *Mon. Wea. Rev.*, **118**, 67–93.
- Reynolds S. E., M. Brook, and M. F. Gourley, 1957: Thunderstorm charge separation. *J. Meteor.*, **14**, 426–436.
- Ries, G., 1967: Results concerning the sunrise effect of VLF signals propagated over long paths. *Radio Sci.*, **2**, 531– 538.
- Rodger, C. J., S. Werner , J. B. Brundell , E. H. Lay , N. R. Thomson , R. H. Holzworth, and R. L. Dowden, 2006: Detection efficiency of the VLF World-Wide Lightning Location Network (WWLLN): initial case study. *Ann. Geophys.*, **24**, 3197–3214.
- Rust, W. D., D. R. Macgorman, T. J. Schuur, E. C. Bruning, S. A. Weiss, J. Straka, W. Rison, T. Hamlin, P. R. Krehbiel, M. Biggerstaff, I. Apostololakopoulos, 2004: Overview of the 2003 and 2004 field program phases of the Thunderstorm

- Electrification and Lightning Experiment (TELEX). *American Geophysical Union, Fall Meeting 2004*, abstract #AE41A-08.
- Rutledge S. A., E. R. Williams, and T. D. Keenan, 1992: The Down Under Doppler and Electricity Experiment (DUNDEE): Overview and preliminary results. *Bull. Amer. Meteor. Soc.*, **73**, 3–16.
- Sadler, J., 1975: The upper tropospheric circulation over the global tropics. *Department of Meteorology, University of Hawaii, UHMET-75-05*, November 1975.
- Saunders, C., 1993: A review of thunderstorm electrification processes. *J. Appl. Meteor.*, **32**, 642–655.
- Saunders, C. P. R., 1994: Thunderstorm electrification laboratory experiments and charging mechanisms. *J. Geophys. Res.*, **99**, 10,773–10,780.
- Saunders, C. P. R., 1995: Thunderstorm electrification, in *Handbook of Atmospheric Electrodynamics, Volume 1*, pp. 61-92, CRC Press, Inc., Boca Raton.
- Saunders, C. P. R., W. D. Keith, and R. P. Mitzeva, 1991: The influence of liquid water on thunderstorm charging. *J. Geophys. Res.*, **96**, 11 007- 11 017.
- Schlamp, R. J., S. N. Grover, H. R. Pruppacher, and A. E. Hamielec, 1976: A numerical investigation of the effect of electric charges and vertical external electric fields on the collision efficiency of cloud drops. *J. Atmos. Sci.*, **33**, 1747–1755.
- Shao, X.M., P.R. Krehbiel, 1996: The temporal development of intracloud lightning, *J. Geophys. Res.*, **101**, D21, 26,641-26,668.
- Shao, X.M., M. Stanley, A. Regan, J. Harlin, M. Pongratz, and M. Stock, 2006: Total lightning observations with the new and improved Los Alamos Sferic Array

- (LASA). *J. Atmos. Oceanic Technol.*, **23**, 1273–1288.
- Sherwood, S. C., V. T. J. Phillips and J. S. Wettlaufer, 2006: Small ice crystals and the climatology of lightning. *Geophys. Res. Lett.*, **33**, No. 5, L05804  
10.1029/2005GL025242.
- Smith, D. A., X. M. Shao, D. N. Holden, C. T. Rhodes, M. Brook, P. R. Krehbiel, M. Stanley, W. Rison, and R. J. Thomas, 1999: A distinct class of isolated intracloud lightning discharges and their associated radio emissions, *J. Geophys. Res.*, **104**(D4), 4189–4212.
- Smith, D. A., K. B. Eack, J. Harlin, M. J. Heavner, A. R. Jacobson, R. S. Massey, X. M. Shao, and K. C. Wiens, 2002: The Los Alamos Sferic Array: A research tool for lightning investigations, *J. Geophys. Res.*, **107**(D13), 4183,  
doi:10.1029/2001JD000502.
- Soriano, L. R., F. Pablo, and E. G. Díez, 2001: Relationship between convective precipitation and cloud-to-ground lightning in the Iberian Peninsula. *Mon. Wea. Rev.*, **129**, 2998–3003.
- Squires, K., and S. Businger, 2008: The morphology of eyewall lightning outbreaks in two category five hurricanes. *Mon. Wea. Rev.* In press.
- Szoke, E.J., E.J. Zipser, and D.P. Jorgensen, 1986: A radar study of convective cells in mesoscale systems in GATE. Part I: Vertical profile statistics and comparison with hurricanes. *J. Atmos. Sci.*, **43**, 182–198.
- Szoke, E. J., J. M. Brown, J. A. McGinley, and D. Rodgers, 1994: Forecasting for a large field program: STORM-FEST. *Wea. Forecasting*, **9**, 593–605.

- Takahashi, T., 1976: Warm rain, giant nuclei and chemical balance: A numerical model. *J. Atmos. Sci.*, **33**, 269-286.
- Takahashi, T., 1978a: Riming electrification as a charge generation mechanism in thunderstorms. *J Atmos. Sci.*, **35**, 1536-1548.
- Takahashi, T., 1978b: Electrical properties of oceanic tropical clouds at Ponape, Micronesia. *Mon. Wea. Rev.*, **106**, 1598–1612.
- Takahashi, T., 1979: Warm cloud electricity in a shallow axisymmetric cloud model. *J Atmos. Sci.* , **36**, 2236-2258.
- Takahashi, T., 1984: Thunderstorm electrification—a numerical study. *J. Atmos. Sci.*, **41**, 2541–2558.
- Takahashi, T., 1990: Near absence of lightning in torrential rainfall producing Micronesian thunderstorms. *Geophys. Res. Lett.*, **17**, 2381–2384.
- Tapia, A., J.A. Smith, and M. Dixon, 1998: Estimation of convective rainfall from lightning observations. *J. Appl. Meteor.*, **37**, 1497–1509.
- Taylor, W. L., 1960: VLF attenuation for east-west and west-east daytime propagation using atmospherics. *J. Geophys. Res.*, **65**, 1933.
- Thomson, N. R., 1993: Experimental daytime VLF ionospheric parameters, *J. Atmos. Terr. Phys.*, **55**, 173 – 184.
- Thomson, N. R., M. A. Clilverd, and W. M. McRae, 2007: Nighttime ionospheric D region parameters from VLF phase and amplitude. *J. Geophys. Res.*, **112**, A07304, doi:10.1029/2007JA012271.

- Toracinta, E.R., K.I. Mohr, E.J. Zipser, and R.E. Orville, 1996: A comparison of WSR-88D reflectivities, SSM/I brightness temperatures, and lightning for mesoscale convective systems in Texas. Part I: Radar reflectivity and lightning. *J. Appl. Meteor.*, **35**, 902–918.
- Toracinta, E.R., D.J. Cecil, E.J. Zipser, and S.W. Nesbitt, 2002: Radar, passive microwave, and lightning characteristics of precipitating systems in the Tropics. *Mon. Wea. Rev.*, **130**, 802–824.
- Wait, J. R., 1962: Electromagnetic waves in stratified media. Pergamon, Tarrytown, N.Y.
- Wait, J.R., 1968: Theory of the terrestrial propagation of VLF electromagnetic waves. *Advances in electronics and electronic physics*, (L. Marton, Ed.), Academic Press.
- Wait, J.R., 1996: Electromagnetic waves in stratified media. Oxford University Press, Inc.
- Wait J. R. and Spies K. P., 1964: Characteristics of the earth-ionosphere waveguide for VLF radio waves, *NBS Tech. Note*, **300**.
- Walker, D., 1965: Phase steps and amplitude fading of VLF signals at dawn and dusk. *J. Res. Natl. Bur. Stand., Sect. D.*, **69**, 1435–1443.
- Wang, C. P., 1963: Lightning discharges in the tropics, 1. Whole discharges. *J. Geophys. Res.*, **68**(7), 1943–1949.
- Webster, P.J., and R. Lukas, 1992: TOGA COARE: The Coupled Ocean—Atmosphere Response Experiment. *Bull. Amer. Meteor. Soc.*, **73**, 1377–1416.

- Williams, E., K. Rothkin, D. Stevenson, and D. Boccippio, 2000: Global lightning variations caused by changes in thunderstorm flash rate and by changes in the number of thunderstorms. *J. Appl. Meteor.*, **39**, 2223–2230.
- Wilson, J. W., and D. L. Megenhardt, 1997: Thunderstorm initiation, organization, and lifetime associated with Florida boundary layer convergence lines. *Mon. Wea. Rev.*, **125**, 1507–1525.
- Yang, S., W.S. Olson, J.J. Wang, T.L. Bell, E.A. Smith, and C.D. Kummerow, 2006: Precipitation and latent heating distributions from satellite passive microwave radiometry. Part II: Evaluation of estimates using independent data. *J. Appl. Meteor. Climatol.*, **45**, 721–739.
- Zipser, E. J., 1970: The Line Island Experiment, its place in tropical meteorology and the rise of the fourth school of thought. *Bull. Amer. Meteor. Soc.*, **51**, 1136–1146.
- Zipser, E. J., 1994: Deep cumulonimbus cloud systems in the tropics with and without lightning. *Mon. Wea. Rev.*, **122**, 1837–1851.
- Zipser, E. and M. LeMone, 1980: Cumulonimbus vertical velocity events in GATE. Part II: Synthesis and model core structure. *J. Atmos. Sci.*, **37**, 2458–2469.
- Zipser, E.J., and K.R. Lutz, 1994: The vertical profile of radar reflectivity of convective cells: A strong indicator of storm intensity and lightning probability? *Mon. Wea. Rev.*, **122**, 1751–1759.